A MULTISCALE FRAMEWORK FOR STRUCTURE OF CONFINED WATER AND ELECTROLYTES

BY

SIKANDAR Y. MASHAYAK

DISSERTATION

Submitted in partial fulfillment of the requirements
for the degree of Doctor of Philosophy in Mechanical Engineering
with a concentration in Computational Science and Engineering
in the Graduate College of the
University of Illinois at Urbana-Champaign, 2017

Urbana, Illinois

Doctoral Committee:

Professor Narayana R. Aluru, Chair and Director of Research
Professor Kenneth S. Schweizer
Assistant Professor Andrew L. Ferguson
Professor Emeritus Eric Jakobsson

Abstract

Nanoconfined water and aqueous solutions play a prominent role in nature and technological applications. Understanding molecular origins of the properties of aqueous interfaces is critical to devising novel nanofluidic applications related to energy, water, and health. Near an interface, the inhomogeneous and anisotropic arrangement of water molecules gives rise to pronounced variations in the structural, thermodynamic, dynamic, and electrochemical properties of the nanofluidic systems. Classical continuum theories fail to accurately describe such atomic level variations in the properties of nanoconfined fluids. Moreover, accurate modeling of molecular-level details of water is still a long-standing challenge for liquid state theories.

In this work, we present an empirical potential based quasi-continuum theory (EQT) to accurately predict the molecular-level properties of interfacial water and aqueous electrolytes. In EQT, we employ rigorous statistical mechanics tools to incorporate interatomic interactions, long-range electrostatics, molecular correlations, and polarization effects at a continuum-level. Explicit consideration of atomic interactions of water molecules is both theoretically and numerically challenging. We develop a systematic coarse-graining approach to coarse-grain interactions of water molecules and electrolyte ions from a high-resolution atomistic scale to the continuum scale.

We show that EQT can predict the density profiles, i.e., molecular arrangement, of confined water as accurately as fully atomistic simulations. To demonstrate the ability of EQT to incorporate the water polarization, ion hydration, and electrostatic correlations effects, we simulate electric double layers and show that EQT can accurately predict the distribution of ions in a thin EDL and also reproduce the complex phenomenon of charge inversion. Furthermore, we show that EQT can also be combined with the classical density functional theory to model grand potential function for inhomogeneous fluids and accurately predict thermodynamic properties. Since EQT systematically and accurately links details of the atomic scales to the macroscopic continuum scales, it is inherently a multiscale approach.

To my family.

Acknowledgments

First, I would like to express my gratitude and appreciation to my advisor, Prof. Narayana R. Aluru. I am deeply grateful for his guidance, support, and patience. I would like to thank him for the variety of experience that I have gathered by being a part of his research group. I would also like to thank Prof. Eric Jakobsson, Prof. Kenneth S. Schweizer, and Prof. Andrew L. Ferguson for serving on my doctoral committee. I am also grateful to Dr. Christoph Junghans. I am happy to have gotten a chance to collaborate with him closely on implementing coarse-graining methods in the VOTCA tool. I am grateful to all former and present members of Prof. Aluru's research group with whom I have had a pleasure to work. The shared sense of camaraderie made it easier to show up for work every day and try harder. I would also like to acknowledge the National Science Foundation (NSF) and the Air Force Office of Scientific Research (AFOSR) for financial support. I also acknowledge the use of the Taub cluster provided by the Computational Science and Engineering Program at the University of Illinois.

Above all, I would like to thank my family especially my parents, Meher and Yusuf, and my wife, Uzma, for their love, encouragement, and patience throughout the long and rewarding journey of the graduate school.

Table of Contents

List of Tables

List of Figures

Chapter 1

Introduction

Aqueous interfaces are ubiquitous in nature in porous materials, around and within biological molecules, and have technological significance in micro/nanofluidic applications. For example, sorption processes at the mineral-aqueous solution interfaces play a major role in removal of trace element contaminants from natural waters [23]. Water molecules next to protein surfaces govern folding, three-dimensional structure, activity, and stability of proteins[112]. Biological nanopores, such as aquaporins, exploit interfacial interactions of confined water molecules to attain extremely high selectivity and permeability[138]. Furthermore, due to significant progress made in nano-fabrication technologies, it is now possible to design and engineer sophisticated micro/nanostructured interfacial systems for novel nanofluidic applications related to energy, water, and health, such as filtration [137, 50, 5, 64, 16], desalination [132, 57], energy storage devices [28, 134], DNA sequencing [38], lab-on-a-chip [31] and many other industrial applications.

Water at interfaces adds exceptional complexity and diversity to the interfacial systems [26, 43, 42, 136, 17, 118]. Water is well-known for its unique properties, such as the temperature of maximum density (TMD) and the diffusivity increase upon compression (DIC). Interfacial water in the nanoscale confinement can exhibit new phase behavior, such as the formation of vapor at room temperature and crystallization into new phases not found in the bulk ices [43]. The complexity and unusual characteristics of water are due to the small size and rich statistical mechanics of intermolecular interactions and microscopic structure of water molecules [42, 66]. Distinct polar charge distribution of the water molecule gives rise to highly directional intermolecular interactions, strong hydrogen bonding, polarization, and orientational ordering, which dominate structural and thermodynamic properties of water. Near an interface, additional conflicts between surface-water interactions, spatial constraints, and water's tendency to form hydrogen-bonded networks result in microscopic variations in the density, orientation, thermodynamic, and transport properties of water which are widely different from its bulk properties [26]. Furthermore, layer of structured water around ions and charge-dipole interactions play a dominant role in determining the distribution of ions and electrochemical properties of electric double layers (EDLs) near charged surfaces[7].

Understanding the molecular origins of the interfacial fluid properties is critical to devise mechanisms

to control interfacial phenomena and design novel fluidic functionalities. Variations in the surface-fluid molecular interactions, packing and orientational ordering, thermodynamic, and dynamical properties of fluid molecules across multiple length scales ranging from a few Angstroms to several nanometers govern the behavior of fluidic systems involving interfaces. For example, due to the long range nature of electrostatics, the local arrangement of ions in the thin EDL near the interface region has strong effects on the electrokinetics at nanometric, micrometric and even larger scales [19]. Therefore, it is important to study interfacial fluid phenomena at multiple length-scales.

Experimental investigation of the narrow intefacial region, despite significant progress in new instruments and tools over the past few decades, is still challenging [163, 164, 17]. Direct measurements of chemical details in the interfacial region is difficult because fluctuations hinder the ability to separate signal from the interface region over those of the adjacent bulk-like phases. Therefore, theory and computational tools are essential to obtain molecular level insights of interfaces.

Molecular simulation techniques, such as molecular dynamics (MD) and Monte Carlo (MC) simulations, can be used to study the microscopic properties of interfacial fluids [9, 40]. However, it is computationally expensive to perform atomistic simulations due to long equilibration times and extensive phase-space sampling required to compute average properties reliably, i.e., with low statistical noise. For example, MD simulations of electrolyte systems require thousands of water molecules per ion and long simulations to achieve reliable statistics. Therefore, the time- and length-scales accessible by molecular simulations are limited. On the other hand, the classical continuum methods, such as Navier-Stokes equations, are computationally efficient, but fail to accurately describe atomic-level structure and properties of confined fluids [114]. As a result, molecular simulations and classical continuum methods are not applicable for applications that involve multiple time and length scales ranging from the atomic to continuum scales [10]. To address these issues, we need a multiscale method which is not only as accurate as molecular simulations, but also as fast as classical continuum methods.

There exist liquid state theories, such as integral equation theory (IET) [58, 52] and classical density functional theory (cDFT) [34, 158, 1], which can describe atomic-level structure and thermodynamic properties of confined fluids at much lower computational cost than molecular simulations. These theories have been successfully applied to model atom-like fluids, such as hard-sphere models [124] and simple Lennard-Jones (LJ) fluids [158, 157, 139], in bulk and confined environments. However, accurate modeling of molecular fluids, most notably water, is still a long standing challenge for liquid state theories.

In this thesis, we develop a systematic multiscale approach to study properties of interfacial water and aqueous electrolytes using an empirical potential-based quasi-continuum theory (EQT). EQT [117, 6] is a

multiscale theory, that seamlessly integrates interatomic potentials describing various atomic interactions into the continuum framework, to accurately predict the equilibrium density and potential profiles of confined fluids. On the one hand, EQT captures the atomic details, and hence, it is more rigorous than the classical continuum methods. On the other hand, it is based on a continuum framework, therefore it is computationally faster than molecular simulations. In [117, 6], EQT was established for the simple Lennard-Jones (LJ) fluids, such as argon and methane, which are modeled as single site molecules with LJ pair potentials. It was shown that EQT can predict the structural properties of the confined LJ fluids as accurately as MD simulations.

In this work, we extend the EQT framework to more complex confined fluid systems, such as LJ mixtures, water, and electric double layers (EDLs). We also extend EQT to predict not only the structural properties but also the thermodynamic properties, such as local pressure tensor, surface tension, and solvation force of confined fluids. Main contributions of this work are

- We develop a systematic coarse-graining approach to coarse-grain pair potentials for complex molecules, such as water, from a high-resolution discrete particle based representation to the continnum-based average density field representation.
- We develop a point dipole based electrostatic potential framework to include water polarization, dielectric variation, hydration effects, and ion-ion electrostatic correlations on the arrangements of ions in EDLs.
- We incorporate integral integration theory, such Percus-Yevick (PY) equation and hypernetted chain theory (HNC), and fundamental measure theory (FMT) in the EQT framework to account for the fluid-fluid pair correlation effects, which were ignored in [117, 6].
- We employ the EQT formulation into the grand potential functional of the classical density functional theory (cDFT) to compute the thermodynamic properties of confined fluids.

The thesis is organized as follows. In Chapter 2, we describe the EQT framework to predict density and potential profiles of a confined fluid. We explain the challenges of determining fluid-fluid potentials in a continuum framework and present three approaches to incorporate fluid-fluid pair correlations effects. We demonstrate ability of EQT to accurately predict density of a confined fluid by simulating Lennard-Jones (LJ) fluids confined inside slit-like channels. In Chapter 3, we combine EQT with cDFT to predict thermodynamic properties of confined fluids and show that the EQT-cDFT framework can accurately predict thermodynamic properties of confined LJ systems. In Chapter 4, we develop a multiscale model to study properties of water confined inside slit-like channels by two multiscale simulation approaches: the coarse-grained molecular

dynamics (CG-MD) and EQT. In Chapter 5, we present EQT for EDL, which incorporates the polarization and hydration effects of water explicitly. We demonstrate the EQT framework for EDL by simulating NaCl aqueous electrolyte confined inside slit-like capacitor channels at various ion concentrations and surface charge densities. In Chapter 6, we study the importance of electrostatic correlations to accurately predict charge inversion phenomenon in EDL and present a framework to incorporate electrostatic correlations in EQT for EDLs. In Chapter 7, we present a direct and computationally efficient approach to determine coarse-grained potentials for from integral equation theory. Finally, the concluding remarks of this thesis work are presented in Chapter 8.

Chapter 2

Empirical potential-based quasi-continuum theory (EQT)

2.1 EQT framework

Consider a fluid confined in a slit channel formed by two parallel walls that are infinite in the x and y directions (see Fig. 2.1). At equilibrium, the distribution of the fluid molecules is given by the 1-D Nernst-Planck (NP) equation,

$$\frac{d}{dz}\left(\frac{d\rho}{dz}+\frac{\rho}{k_{\mathrm{B}}T}\frac{dU}{dz}\right)=0 \tag{2.1}$$

with boundary conditions

$$\rho(0)=0 \tag{2.2a}$$

$$\rho(L)=0 \tag{2.2b}$$

$$\frac{1}{L}\int_0^L \rho(z)\,dz=\rho_{\mathrm{avg}} \tag{2.2c}$$

where, ρ and U are the density and total potential of the fluid, respectively, T is the fluid temperature, k_{B} is the Boltzmann constant, L is the channel width, ρ_{avg} is the average density of the fluid inside the channel, and z-axis is normal to the wall. We note that the solution of Eqs. 2.1 and 2.2 is equivalent to the solution of the Boltzmann distribution equation,

$$\rho(z)=\rho_{\mathrm{ref}}\exp\left(-\frac{U(z)-U_{\mathrm{ref}}}{k_{\mathrm{B}}T}\right), \tag{2.3}$$

where ρ_{ref} and U_{ref} are the reference density and potential of the fluid, respectively. The confined fluid is assumed to be in thermodynamic equilibrium with a reference bulk fluid system. Therefore, the reference density and potential required in Eq. 5.3 can be determined from the reference bulk system.

To predict the density profile of the confined fluid from Eq. (2.1), we need a framework to compute the total potential, U. For a confined fluid system, the total potential is due to wall-fluid and fluid-fluid interactions, and it can be computed as a sum of the wall-fluid potential, U^{wf}, and the fluid-fluid potential,

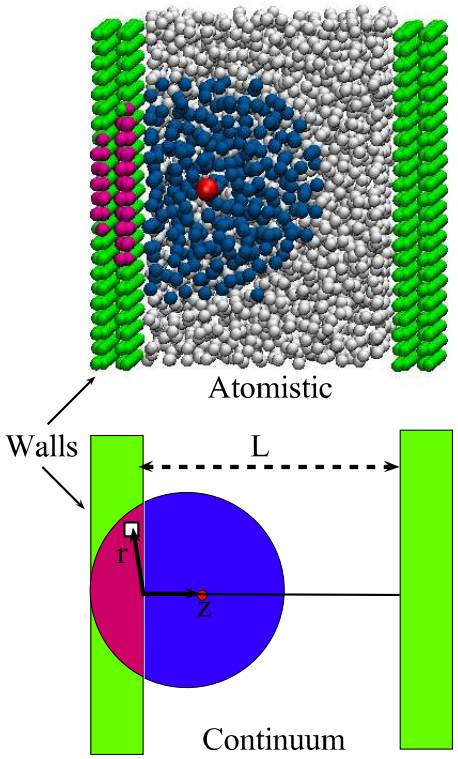

Figure 2.1: Atomistic (top) and continuum (bottom) representation of confined fluid. Selected fluid atoms (blue) and wall atoms (red) contribute to the total potential at location z.

U^{ff}, i.e.,

$$U(z) = U^{\mathrm{wf}}(z) + U^{ff}(z). \tag{2.4}$$

The principal idea in EQT is to compute U^{wf} and U^{ff} by a continuum approximation. In the continuum approximation, wall and fluid particles are represented by their local densities. Procedures to determine U^{wf} and U^{ff} using the continuum approximation are described in Sections 2.1.1 and 2.1.2.

2.1.1 Wall-fluid potential

In the continuum approximation, the wall structure is modeled as a continuous medium with a particle density, $\rho_{\mathrm{wall}}(\boldsymbol{r})$. Then, the wall-fluid potential is determined as

$$U^{\mathrm{wf}}(\boldsymbol{r}) = \int \rho_{\mathrm{wall}}(\boldsymbol{r}')u^{\mathrm{wf}}(r)d\boldsymbol{r}', \tag{2.5}$$

where $u^{\mathrm{wf}}(r)$ is the pair potential between the wall and fluid atoms, $\boldsymbol{r}$ and $\boldsymbol{r}'$ are the position vectors, and $r = |\boldsymbol{r} - \boldsymbol{r}'|$. Note that in Eq. 2.5, $\boldsymbol{r} = x\boldsymbol{i} + y\boldsymbol{j} + z\boldsymbol{k}$ is a general position vector. In the case of a 1-D slit

channel, the system is periodic in x and y dimensions and therefore, we consider only the z-variations of the properties, i.e., $U^{\text{wf}}(\boldsymbol{r}) = U^{\text{wf}}(x, y, z) = U^{\text{wf}}(z) \,\forall\, x, y$.

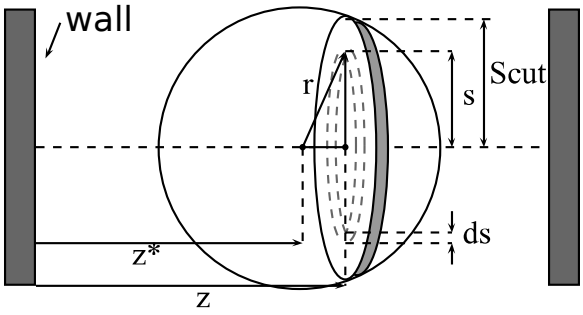

Figure 2.2: Schematic of integration procedure for EQT potential calculations.

The integration in Eq. 2.5 can be simplified using the cylindrical symmetry of the slit channel. For a given location z, the neighboring volume V can be divided into circular disks with thickness dz' (see Fig. 2.2), and the contribution to the potential at z due to the particles in a circular disk at location z', $dU(z')$, can be computed as

$$dU(z') = \left(\int_0^{S_{\text{cut}}} u(s) 2\pi s ds \right) \rho(z') dz', \tag{2.6}$$

where, $s = \sqrt{r^2 - (z - z')^2}$ and S_{cut} corresponds to the cut-off distance, R_{cut}, for the pair potential, $u(r)$. Substituting $r = \sqrt{s^2 + (z - z')^2}$,

$$dU(z') = \left(\int_{|z-z'|}^{r_{\text{cut}}} u(r) 2\pi r dr \right) \rho(z') dz'. \tag{2.7}$$

Hence, for a slit channel geometry, Eq. 2.5 simplifies to

$$U^{\text{wf}}(z) = 2\pi \int_{\Gamma_{\text{wall}}} \rho_{\text{wall}}(z') \left(\int_{|z-z'|}^{R_{\text{cut}}^{\text{wf}}} u^{\text{wf}}(r) r dr \right) dz' \tag{2.8}$$

where, $R_{\text{cut}}^{\text{wf}}$ is the cut-off distance for the wall-fluid pair potential and Γ_{wall} is the region defined by the location and the dimensions of the channel walls.

2.1.2 Fluid-fluid potential

The fluid-fluid potential is more challenging to compute than the wall-fluid potential. Fluid-fluid interactions give rise to the finite size, i.e., excluded volume effects, dispersion attraction, and particle-particle correlations in the fluid[52]. Incorporating all the effects of the fluid-fluid interactions is a major challenge for a continuum-based framework. For fluid molecules interacting via pair additive potentials, U^{ff} can be

computed as

$$U^{\mathrm{ff}}(\boldsymbol{r}) = \int \rho(\boldsymbol{r}')g^{(2)}(\boldsymbol{r},\boldsymbol{r}')u^{\mathrm{ff}}(r)d\boldsymbol{r}', \tag{2.9}$$

where $g^{(2)}(\boldsymbol{r},\boldsymbol{r}')$ is the two-body correlation (also known as the radial distribution function (RDF)) [52] and $u^{\mathrm{ff}}(r)$ is the pair potential between fluid atoms. The exact expression for $g^{(2)}(\boldsymbol{r},\boldsymbol{r}')$ for inhomogeneous real fluids is unknown. In the following subsections, we present three different approaches to approximate fluid-fluid correlations and determine $U^{\mathrm{ff}}(\boldsymbol{r})$.

Soft-core potential approach

In the EQT framework proposed by Raghunathan et al [117], a mean field approximation (MFA) is used to determine $U^{\mathrm{ff}}(\boldsymbol{r})$. In MFA, the fluid-fluid pair correlations are ignored and $g^{(2)}(\boldsymbol{r},\boldsymbol{r}')$ is assumed to be 1. Therefore, in MFA, $U^{\mathrm{ff}}(\boldsymbol{r})$ is given by

$$U^{\mathrm{ff}}(\boldsymbol{r}) = \int \rho(\boldsymbol{r}')u^{\mathrm{ff}}(r)d\boldsymbol{r}'. \tag{2.10}$$

Similar to the wall-fluid potential (Eq. 2.8), Eq. 2.10 can be simplified using the cylindrical symmetry of the slit channel as

$$U^{\mathrm{ff}}(z) = 2\pi \int \rho(z') \left(\int_{|z-z'|}^{R^{\mathrm{ff}}_{\mathrm{cut}}} u^{\mathrm{ff}}(r) r dr \right) dz', \tag{2.11}$$

where, $R^{\mathrm{ff}}_{\mathrm{cut}}$ is the cut-off distance for the fluid-fluid pair potential.

In addition to the errors arising from MFA, Eq. 2.10 poses numerical challenges due to inclusion of self interactions and hard repulsion cores of the pair potentials, i.e., $u^{\mathrm{ff}}(r) \to \infty$ as $r \to 0$. Hence, to account for the neglected pair correlations in the MFA and to avoid self interactions, Raghunathan et al.[117] replace the hard repulsion core of $u^{\mathrm{ff}}(r)$ by an effective soft core repulsion model, which can be optimized to account for the neglected pair correlations in the MFA. References [117, 6] discuss formulations of core-softened u^{ff}(r) for simple Lennard-Jones fluids, and single-site core-softened potentials for the graphite-CO_2 system are discussed in [129].

In this work, we propose two approaches to address the limitations of the mean-field approximation in EQT and incorporate fluid-fluid correlation effects in the fluid-fluid potential formulation. In the first approach, we approximate $g^{(2)}(\boldsymbol{r},\boldsymbol{r}')$ by a reference bulk hard-sphere fluid RDF and add a correlation correction potential. In the second approach, we use a hard sphere functional based on the fundamental measure theory (FMT) to account for the excluded volume and correlation effects due to purely repulsive component of the fluid-fluid pair potential.

Correlation correction approach

In this approach, the fluid-fluid pair correlation is approximated by a hard-sphere radial distribution function (RDF), $g^{\text{hs}}(r)$. Similar approach to approximate the fluid-fluid correlations has been used by Tang and Wu [139]. However, the hard sphere RDF approximation may not accurately reproduce the properties of a real fluid. Therefore, to account for the effects of real fluid pair correlations in the hard sphere approximation, we add a correlation correction potential (CCP), $u^{\text{ff}}_{\text{ccp}}(r)$, and reformulate Eq. 2.10 as

$$U^{\text{ff}}(\mathbf{r}) = \int \rho(\mathbf{r}') \left(u^{\text{ff}}(r) g^{\text{hs}}(r) + u^{\text{ff}}_{\text{ccp}}(r) \right) d\mathbf{r}'. \tag{2.12}$$

In Eq. 2.12, for $u^{\text{ff}}(r)$ we use an atomistic model-based fluid-fluid pair potential, and for $g^{\text{hs}}(r)$, we use the Percus-Yevick (PY) equation for a hard sphere fluid [144, 155, 135]

Hard sphere functional approach

A hard sphere fluid is an important reference system to model the short-range steep repulsion part of the fluid-fluid inter-particle interactions. Due to the short-range repulsion each fluid molecule has a volume which is not accessible to other molecules. This effect is known as the excluded volume effect. The short-range repulsion plays a dominant role in determining the structure of fluids especially at high densities [154].

Rosenfeld's fundamental measure theory (FMT) [121] provides a framework to model the excess (over the ideal gas) free energy of inhomogeneous fluids due to the short-range steep repulsive part of inter-particle interactions. It accounts for both the excluded volume effects and pair correlations in an inhomogeneous fluid due to the hard repulsive part of pair interactions. Therefore, both the numerical difficulties in MFA and drawbacks of bulk RDF approximation can be addressed by FMT.

In the FMT-based approach, we split U^{ff} into a purely repulsive and dispersion components as

$$U^{\text{ff}}(\boldsymbol{r}) = U^{\text{ff}}_{\text{hs}}(\boldsymbol{r}) + \int_{R^{\text{ff}}_{\text{min}}}^{R^{\text{ff}}_{\text{cut}}} \rho(\boldsymbol{r}') u^{\text{ff}}(r) d\boldsymbol{r}', \tag{2.13}$$

where $R^{\text{ff}}_{\text{min}}$ and $R^{\text{ff}}_{\text{cut}}$ are the inner and outer cut-offs for the dispersion part of the pair potential, respectively. In Eq. 5.14, $U^{\text{ff}}_{\text{hs}}(\boldsymbol{r})$ is the purely repulsive component of the fluid-fluid interactions, which mainly accounts for the excluded volume effects. We use the hard sphere fluid approximation based on the White-Bear version of FMT mark II [124] to determine $U^{\text{ff}}_{\text{hs}}(r)$ as

$$U^{\text{ff}}_{\text{hs}}(\boldsymbol{r}) = k_{\text{B}} T \sum_{\alpha} \int d\boldsymbol{r}' \frac{\partial \Phi \left(\{n_\alpha\} \right)}{\partial n_\alpha} \frac{\delta n_\alpha \left(\boldsymbol{r}' \right)}{\delta \rho_i \left(\boldsymbol{r} \right)}, \tag{2.14}$$

where Φ is the reduced free energy density and $\{n_\alpha\}$ are the set of weighted densities. The details about Φ and $\{n_\alpha\}$ are given in Appendix A. The second term in Eq. 2.13 accounts for the fluid-fluid vdW attractive interactions using a mean field approximation.

2.2 Results and discussion

To demonstrate the EQT approach, we simulate two different confined LJ fluid systems, namely, methane-graphene and argon-graphene slit-channel systems. In both the systems, the LJ fluid is confined between two flat graphene walls in equilibrium with the bulk reservoir. The thermodynamic state of the confined fluid is defined by the bulk reservoir temperature, T, and density, ρ_b. We consider supercritical states of the methane and argon fluids given in Table 2.1.

Table 2.1: Thermodynamic states of methane and argon.

	T (K)	ρ_b (nm^{-3})
Methane	296	18
Argon	300	24

To validate the accuracy of different fluid-fluid potential computation approaches in EQT, we compare the EQT results with the equilibrium MD simulations for various channel widths from 2σ to 20σ, where σ is the length-scale parameter for the LJ interaction between fluid molecules (see Table 2.2). To perform the reference MD simulations, we use the similar procedure and the interaction parameters given in Ref. [6]. The MD simulations are performed in the NVT (canonical) ensemble by GROMACS [113]. Methane, argon, and graphene carbon atoms are modeled as LJ type spherical particles. The LJ interaction parameters used in MD simulations for various pairs of methane, argon, and graphene carbon particles are given in Table 2.2. The two graphene layers are placed along the XY plane, and the lateral dimensions of the layers are 3.83400×3.68927 nm^2. The separation distance between the two graphene layers, i.e., the channel width, is varied from 2σ to 20σ. The average densities of fluid molecules, i.e., ρ_avg = no. of molecules/volume of the channel, in various size channels are given in Table 2.3. Spherical cutoff of 1.38 nm is used for the Lennard-Jones interactions. Wall atoms are kept fixed at their original positions. Periodic boundary conditions are specified in the x, y, and z directions. The simulation box is padded with a vacuum layer of 60σ width in the z dimension to avoid the interactions between periodic images in the z dimension. Temperature is maintained using the Nosé-Hoover thermostat [108] with 0.5 ps time constant. All systems are equilibrated for 2 ns and production runs of 8 ns are performed with 1 fs time step.

In the EQT simulations of methane-graphene and argon-graphene slit-channel systems, we model $u^\mathrm{wf}(r)$

Table 2.2: LJ interaction parameters for methane (CH4), argon (Ar), and graphene carbon (C) atom pairs.

	C_{12} (kJ/mol)	C_6 (kJ/mol)	σ (nm)
CH4-CH4	0.46341E-04	0.15102E-01	0.3812
CH4-C	0.10353E-04	0.47088E-02	0.3606
Ar-Ar	0.96929E-05	0.62194E-02	0.3405
Ar-C	0.46428E-05	0.29922E-02	0.3402

Table 2.3: Average fluid densities (nm^{-3}) in MD simulations of various size channels.

System	20σ	15σ	10σ	9σ	8σ	7σ	6σ	5σ	4σ	3σ	2σ
Methane-graphene	17.18	16.92	16.37	16.20	15.98	15.68	15.24	14.59	13.58	11.94	9.09
Argon-graphene	22.76	22.30	21.50	21.24	20.88	20.45	19.84	18.99	17.76	15.79	12.05

and $u^{\text{ff}}(r)$ as LJ potentials:

$$u^{\text{wf}}(r) = \frac{C_{12}^{\text{wf}}}{r^{12}} - \frac{C_6^{\text{wf}}}{r^6}, \tag{2.15a}$$

$$u^{\text{ff}}(r) = \frac{C_{12}^{\text{ff}}}{r^{12}} - \frac{C_6^{\text{ff}}}{r^6}, \tag{2.15b}$$

where C_{12}^{wf}, C_6^{wf}, C_{12}^{ff}, and C_6^{ff} are the usual LJ parameters for the wall-fluid and fluid-fluid interactions. For the methane-graphene, argon-graphene, methane-methane, and argon-argon LJ interactions, we use the same LJ parameters as in the MD simulations that are given in Table 2.2. The cut-offs for the wall-fluid and fluid-fluid pair interactions are set to 1.4 nm.

2.2.1 Correlation correction approach

In the correlation correction approach-based EQT, we model $u_{\text{ccp}}^{\text{ff}}(r)$ using uniform cubic B-splines (Eq. B.8). For the cubic B-splines-based $u_{\text{ccp}}^{\text{ff}}(r)$, we use $\Delta r = 0.04$ nm and $n = 36$ and optimize the spline knot values, $\{c_0, c_1, c_2, ..., c_{n+1}\}$, using a systematic approach based on the potential of mean force (PMF) matching, which we describe in Section 4.4. PMF-matching approach optimizes structurally consistent potential parameters. Here, to optimize the spline knot values of $u_{\text{ccp}}^{\text{ff}}(r)$ for methane and argon, we use the corresponding 20σ channel atomistic trajectories from the MD simulation as a reference. Fig. 2.3 shows the optimized $u_{\text{ccp}}^{\text{ff}}(r)$ for the methane-methane and argon-argon interactions.

Fig. 2.5 shows that, for both methane-graphene and argon-graphene systems, the equilibrium density profiles from the EQT with CCP agree well with the MD simulations for various channel widths. We observe that the methane and argon density profiles are similar and oscillatory, because the confined LJ fluid molecules arrange in the layers near the walls due to the competition between the wall-fluid and fluid-fluid interactions. When $L = 3\sigma$, fluid molecules arrange in two layers located around 0.95σ distance from each wall. A layer of particles is added mid-way between the walls with each σ increase in the channel width,

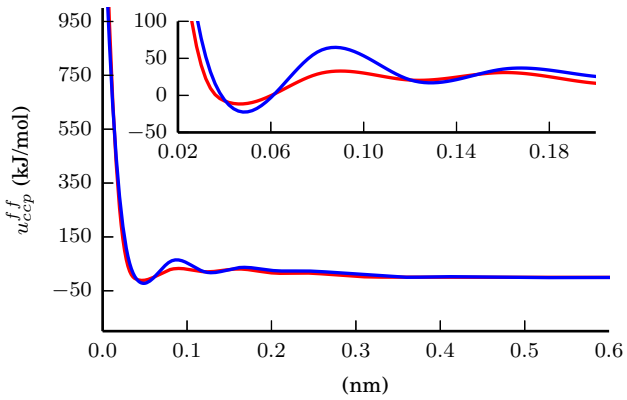

Figure 2.3: Fluid-fluid correlation correction potentials: methane-methane (blue) and argon-argon (red).

and the density of the added layer decreases with increase in the distance from the walls. The maximum number of layers occur when $L = 18\sigma$. Further increase in L only adds flat bulk-like region in the middle of a channel.

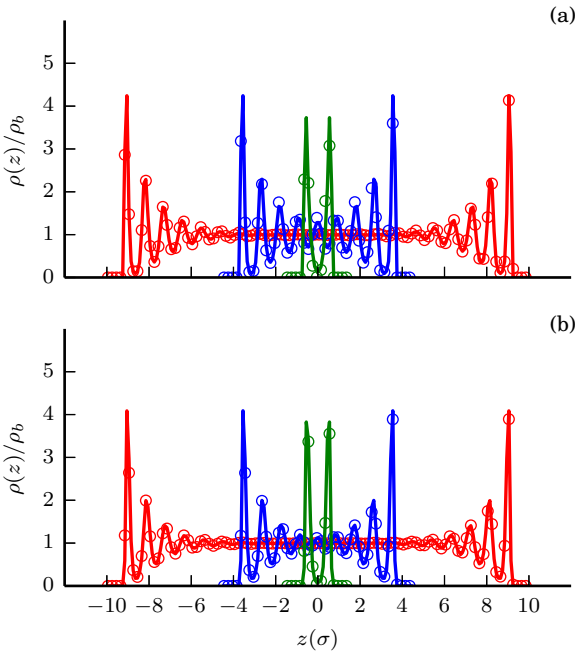

Figure 2.4: Comparison of density profiles of methane (a) and argon (b) from EQT with CCP (lines) and MD (circles) simulations at different channel widths: 20σ (red), 9σ (blue), and 3σ (green).

2.2.2 FMT approach

In the FMT-based EQT simulations, to compute U^{ff} from Eqs. 2.13 and 2.14, we need to specify effective hard-sphere diameter, d_{hs}, for a fluid molecule and the inner cut-off, $R^{\text{ff}}_{\text{min}}$, and outer cut-off $R^{\text{ff}}_{\text{cut}}$ for the dispersion part of the fluid-fluid pair potential. There are different approaches to set $R^{\text{ff}}_{\text{min}}$ for the LJ type pair potentials [154]. Here, we set $R^{\text{ff}}_{\text{min}} = \sigma^{\text{ff}}$ for the fluid-fluid LJ pair potentials, where σ^{ff} is the usual LJ parameter given in Table 2.2. We treat d_{hs} as a free parameter and tune it such that the density profiles from EQT compare well with the reference MD simulations. We find that the effective hard-sphere diameter of 0.375 and 0.32 nm work well for methane and argon, respectively. Fig. 2.5 shows that, for both methane-graphene and argon-graphene systems, the equilibrium density profiles from the FMT-based EQT approach agree well with the MD simulations for various channel widths.

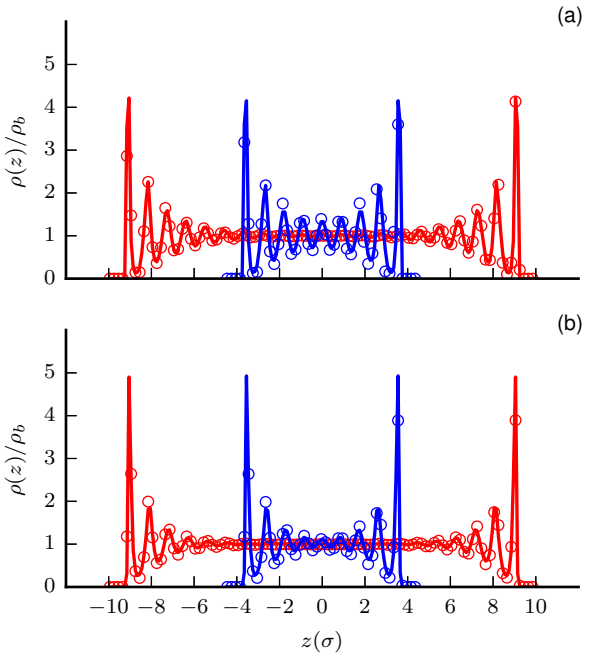

Figure 2.5: Comparison of density profiles of methane (a) and argon (b) from EQT with FMT (lines) and MD (circles) simulations at different channel widths: 20σ (red) and 9σ (blue).

2.3 Summary

In this chapter, we presented details of the empirical potential based quasi-continuum theory (EQT). In EQT, a steady-state Nernst-Planck equation is solved to predict the density, and a continuum approximation is used to compute the potential due to wall-fluid and fluid-fluid atomic interactions. Determining the fluid-

fluid potential of an inhomogeneous fluid is the most challenging part of a continuum-based approach. We presented three models to compute the fluid-fluid potential in EQT: (i) a soft-core potential approach, (ii) correlation correction approach, and (iii) fundamental measure theory (FMT) approach. In the soft-core potential approach, we ignore the fluid-fluid correlations and replace the hard repulsive core of the fluid-fluid pair potential by a soft-core potential. In the correlation correction approach, we approximate the fluid-fluid correlations by the hard-sphere radial distribution function (RDF) and add a correlation correction potential. In the FMT-based approach, we use the White-Bear mark II (WBII) version of FMT to include the finite size and correlation effects of fluid. We demonstrated EQT by simulating two different confined LJ fluid systems, namely, methane-graphene and argon-graphene slit-channel systems. We showed that the EQT predictions of the methane and argon density profiles agree well with the reference MD simulations.

Chapter 3

EQT-cDFT framework for thermodynamic properties

Here, we focus on an application of the EQT framework to determine the equilibrium thermodynamic properties of a confined fluid. For a fluid confined to a slit-like channel, the fundamental thermodynamic relation is [1]

$$\mathrm{d}\Omega = -S\mathrm{d}T - P\mathrm{d}V - N\mathrm{d}\mu + 2\gamma\mathrm{d}A - f_{\mathrm{S}}A\mathrm{d}L, \tag{3.1}$$

where Ω is the grand potential, S is the entropy, T is the temperature, P is the pressure, V is the volume, N is the number of the fluid particles, μ is the chemical potential, γ is the wall-fluid surface tension, A is the surface area of the wall, L is the channel width, and f_{S} is the solvation force. Given the thermodynamic state of a confined fluid defined by T, V, and μ, we can determine the thermodynamic properties of the fluid by evaluating the gradients of Ω. For example, from Eq. 3.1, the wall-fluid surface tension can be computed as $\gamma = \frac{1}{2}\left(\frac{\partial\Omega}{\partial A}\right)_{V,T,L,\mu}$. Therefore, to determine the thermodynamic properties of a confined fluid, we need an expression for Ω. Classical density functional theory (cDFT) [1, 35, 158] provides a framework to determine Ω in terms of the equilibrium density and interaction energy obtained from EQT.

Here, first, we use EQT to model an expression for Ω in terms of the equilibrium density and potentials. Then, we can use the EQT-cDFT-based grand potential functional to compute various thermodynamic properties of confined fluids.

3.1 cDFT

cDFT is a continuum-based technique that describes the properties of inhomogeneous fluids from a microscopic level [1, 35, 158]. It is based on the theorem that, for a fluid in an external field, the Helmholtz free energy, F, is a unique functional of the average molecular density profile, $\rho(\mathbf{r})$, independent of the external potential, $V_{\mathrm{ext}}(\mathbf{r})$ [1, 35, 158]. Therefore, in cDFT, the grand potential is defined as a functional of $\rho(\mathbf{r})$:

$$\Omega\left[\rho(\mathbf{r})\right] = F\left[\rho(\mathbf{r})\right] + \int \left(V_{\mathrm{ext}}(\mathbf{r}) - \mu\right)\rho(\mathbf{r})d\mathbf{r}. \tag{3.2}$$

To determine Ω from Eq. 3.2, we require an expression for $F\left[\rho(\mathbf{r})\right]$. The Helmholtz energy has two parts: (i) the ideal part, $F^{\mathrm{id}}\left[\rho(\mathbf{r})\right]$, and (ii) the excess part, $F^{\mathrm{ex}}\left[\rho(\mathbf{r})\right]$, i.e.,

$$F\left[\rho(\mathbf{r})\right] = F^{\mathrm{id}}\left[\rho(\mathbf{r})\right] + F^{\mathrm{ex}}\left[\rho(\mathbf{r})\right]. \tag{3.3}$$

The ideal part of the Helmholtz energy accounts for the ideal gas free energy,

$$F^{\mathrm{id}}\left[\rho(\mathbf{r})\right] = k_{\mathrm{B}}T \int \rho(\mathbf{r}) \left(\ln\left(\rho(\mathbf{r})\Lambda^3\right) - 1\right) d\mathbf{r}, \tag{3.4}$$

where k_{B} is the Boltzmann constant, $\Lambda = \left(\frac{2\pi\hbar^2}{mk_{\mathrm{B}}T}\right)^{\frac{1}{2}}$ is the thermal wavelength, $\hbar$ is the reduced Planck's constant, and m is the mass of an atom. The excess part of the intrinsic Helmholtz energy accounts for the non-bonded interactions between molecules. Modeling of $F^{\mathrm{ex}}\left[\rho(\mathbf{r})\right]$ is the most challenging part of the cDFT. The exact expression for $F^{\mathrm{ex}}\left[\rho(\mathbf{r})\right]$ is in general unknown [158]. There exists approximate functionals for $F^{\mathrm{ex}}\left[\rho(\mathbf{r})\right]$, such as fundamental-measure theory (FMT) functionals for hard sphere fluids [121, 122, 120, 143, 142, 123, 162] and functionals based on the statistical associating fluid theory (SAFT) [45, 44, 65]. In this work, we use EQT to formulate $F^{\mathrm{ex}}\left[\rho(\mathbf{r})\right]$ as explained in Section 3.2.

3.2 EQT-cDFT

In the EQT-cDFT approach, the fluid-fluid EQT potential model (Eq. 2.12) is used to construct the excess part of the intrinsic Helmholtz energy functional as

$$F^{\mathrm{EQT,ex}}\left[\rho(\mathbf{r})\right] = \frac{1}{2}\int \rho(\mathbf{r}')U^{\mathrm{ff}}(\mathbf{r}')d\mathbf{r}' \tag{3.5}$$

For a confined fluid system, the external potential is due to the wall-fluid interactions, i.e., $V_{\mathrm{ext}}(\mathbf{r}) = U^{\mathrm{wf}}(\mathbf{r})$. Therefore, from Eqs. 3.2, 3.3, 3.4, 2.12, 3.5, and 2.5, we get the EQT-cDFT-based grand potential functional, $\Omega^{\mathrm{EQT}}\left[\rho(\mathbf{r})\right]$, as

$$\begin{aligned}
\Omega^{\mathrm{EQT}}\left[\rho(\mathbf{r})\right] \;=\; & k_{\mathrm{B}}T \int \rho(\mathbf{r}) \left(\ln\left(\rho(\mathbf{r})\Lambda^3\right) - 1\right) d\mathbf{r} \\
& + \frac{1}{2}\int d\mathbf{r}\rho(\mathbf{r}) \int \rho(\mathbf{r}') \left(u^{\mathrm{ff}}(r)g^{\mathrm{hs}}(r) + u^{\mathrm{ff}}_{\mathrm{ccp}}(r)\right) d\mathbf{r}' \\
& + \int \left(U^{\mathrm{wf}}(\mathbf{r}) - \mu\right) \rho(\mathbf{r}) d\mathbf{r}.
\end{aligned} \tag{3.6}$$

We note that the chemical potential, μ, in Eq. 3.6 is same as the bulk fluid chemical potential, μ_{b}, at temperature T and density ρ_{b}. The bulk chemical potential can be defined as

$$\mu_{\mathrm{b}} = \left(\frac{\partial F_{\mathrm{b}}}{\partial \rho_{\mathrm{b}}}\right)_T, \tag{3.7}$$

where F_{b} is the Helmholtz energy per unit volume of the bulk fluid. Applying Eqs. 3.3, 3.4, and 3.5 for a bulk fluid, F_{b} can be computed as

$$F_{\mathrm{b}} = k_{\mathrm{B}}T\rho_{\mathrm{b}}\left(\ln\left(\rho_{\mathrm{b}}\Lambda^3\right) - 1\right) + \frac{1}{2}\rho_{\mathrm{b}}U_{\mathrm{b}}, \tag{3.8}$$

where U_{b} is the potential energy per molecule in the bulk fluid, given by

$$U_{\mathrm{b}} = 4\pi\rho_{\mathrm{b}}\int_0^{R_{\mathrm{cut}}^{\mathrm{ff}}} r^2\left(u^{\mathrm{ff}}(r)g^{\mathrm{hs}}(r) + u_{\mathrm{ccp}}^{\mathrm{ff}}(r)\right)dr. \tag{3.9}$$

Hence, in the EQT-cDFT approach, the chemical potential of a confined fluid can be computed as

$$\mu = k_{\mathrm{B}}T\log\left(\rho_{\mathrm{b}}\Lambda^3\right) + U_{\mathrm{b}}. \tag{3.10}$$

At equilibrium, Ω is minimum. Therefore, the equilibrium $\rho(\mathbf{r})$ can be obtained by minimizing $\Omega\left[\rho(\mathbf{r})\right]$. From Eq. 3.6, by minimizing the EQT-cDFT-based grand potential, $\Omega^{\mathrm{EQT}}\left[\rho(\mathbf{r})\right]$, w.r.t. $\rho(\mathbf{r})$, we obtain the equilibrium density profile of a confined fluid as

$$\rho(\mathbf{r}) = \rho_{\mathrm{b}}\exp\left(-\frac{1}{k_{\mathrm{B}}T}\left(U^{\mathrm{ff}}(\mathbf{r}) + U^{\mathrm{wf}}(\mathbf{r}) - U_{\mathrm{b}}\right)\right). \tag{3.11}$$

Therefore, in the EQT-cDFT approach, one can obtain the equilibrium density and potential profiles of a confined fluid by self-consistently solving Eqs. 2.5, 2.12, and 3.11. One of the advantages of the EQT-cDFT approach (Eq. 3.11) over the Nernst-Planck approach (Eq. 2.1), is that a solution of the EQT-cDFT approach does not require ρ_{avg} as an input; instead, ρ_{avg} can be computed as an output of the EQT-cDFT simulation from the equilibrium density profile.

3.3 Thermodynamic properties

We consider a fluid confined in a slit-like channel, which consists of two infinitely long plane parallel walls placed in the xy plane at $z = 0$ and $z = L$. Therefore, the system is periodic in the x and y directions,

and we focus only on the z-variation of the properties. From the equilibrium values of $\rho(z)$ and $\Omega^{\mathrm{EQT}}[\rho(z)]$, one can determine various thermodynamic properties of a confined fluid [1]. In this work, we compute the properties like total adsorption, local pressure tensor, surface tension, and solvation force as described below.

The total adsorption is the difference between the average number of fluid molecules in the confined region with and without the channel walls. The total adsorption per unit surface area, Γ, can be computed as an integral over the confined region:

$$\Gamma(L) = \frac{1}{2}\int_0^L (\rho(z) - \rho_{\mathrm{b}})\, dz, \tag{3.12}$$

where ρ_{b} is the bulk density of the fluid at a given T and μ, and the factor of $\frac{1}{2}$ is multiplied to account for the two channel walls.

The surface tension, γ, according to the thermodynamic definition, is the isothermal work required to increase the interface by unit area, i.e., $\gamma = \frac{1}{2}\left(\frac{\partial\Omega}{\partial A}\right)_{T,\mu,L}$ for a slit-channel system. Alternatively, γ can also be determined, according to the mechanical definition, in terms of the stress transmitted across a strip of unit width normal to the interface. In this work, we use a mechanical definition of the surface tension given by [75]

$$\gamma(L) = \frac{1}{2}\int_0^L (P_{\mathrm{n}}(z) - P_l(z))\, dz, \tag{3.13}$$

where $P_{\mathrm{n}}(z)$ and $P_l(z)$ are the normal and lateral components of the local pressure tensor. In a bulk fluid, pressure is homogeneous and isotropic, however, in a confined fluid, pressure varies with the position and is anisotropic due to the wall-fluid force field and local variations in the fluid density [33, 56, 14]. For a slit-channel system, $P_l(z)$ can be computed as a negative of the local grand potential density, $\Omega(z)$ [61, 146]. Therefore, from Eq. 3.6,

$$\begin{aligned} P_l(z) \;=\; & -k_{\mathrm{B}}T\rho(z)\left(\ln\left(\rho(z)\Lambda^3\right) - 1\right) \\ & -\frac{1}{2}\rho(z)U^{\mathrm{ff}}(z) \\ & -\left(V_{\mathrm{ext}}(z) - \mu\right)\rho(z). \end{aligned} \tag{3.14}$$

Also, for a slit-channel system in the steady-state, $P_{\mathrm{n}}(z)$ must be uniform across the channel width to satisfy a mechanical equilibrium condition. Therefore, for a given channel of width L, an average normal pressure

value, $P_{\mathrm{n}}(L)$, can be computed using the thermodynamic definition as

$$P_{\mathrm{n}}(L) = -\frac{1}{A}\frac{\partial \Omega^{\mathrm{EQT}}(L)}{\partial L} \tag{3.15}$$

where $\Omega^{\mathrm{EQT}}(L)$ is the total grand potential of the channel of width L, which can be computed from Eq. 3.6. To compute $\partial\Omega^{\mathrm{EQT}}(L)/\partial L$ in Eq. 3.15, we use the central difference scheme as

$$P_{\mathrm{n}}(L) = -\frac{1}{A}\frac{\Omega^{\mathrm{EQT}}(L+\epsilon) - \Omega^{\mathrm{EQT}}(L-\epsilon)}{2\epsilon} \tag{3.16}$$

where ϵ is the infinitesimal change in the channel width. Eqs. 3.15 and 3.16 are analogous to the volume perturbation expressions proposed by de Miguel and Jackson [100] in the context of vapour-liquid interfaces as an extension of the formalism introduced by Eppenga and Frenkel [32] and Harismiadis et al. [55].

The solvation force, f_{S}, is the difference between the pressure exerted by a confined fluid on the channel walls and the bulk fluid pressure, P_{b} [1, 11]. For a slit-like system in mechanical equilibrium, the pressure exerted by a confined fluid on the channel walls is equal to the average normal pressure, $P_{\mathrm{n}}(L)$. Therefore, the solvation force can be computed as

$$f_{\mathrm{S}}(L) = P_{\mathrm{n}}(L) - P_{\mathrm{b}}. \tag{3.17}$$

3.4 Results

To demonstrate the EQT-cDFT approach, we compute the thermodynamic properties of the methane-graphene and argon-graphene slit-channel systems. The accuracy of the EQT-cDFT results is compared with the reference MD simulations. We use the correlation correction approach to compute the fluid-fluid potential in EQT. The optimized correlation correction potentials for the methane-graphene and argon-graphene systems are described in Section 2.2.1. See Section 2.2 for the details of the methane-graphene and argon-graphene slit-channel and reference MD simulations. To compute the local pressure tensors from MD, we use the method of Schofield and Henderson [131] in combination with the Gaussian smoothing kernel similar to ref. [56]. The local pressure determination method is not available in the default GROMACS 4.6.1 version. Therefore, for this work, we modified the GROMACS source code and implemented the method for determining the local pressure tensor in a slit-like geometry. Our implementation of the local pressure tensor method in GROMACS is publicly available on GitHub [4]. Recently, Vanegas et al. [147] have also implemented a local pressure calculation method in a custom verion of GROMACS, which is based on the

Hardy–Murdoch procedure. The surface tension and solvation force values from MD are determined by substituting the MD local pressure values in Eqs. 3.13 and 3.17, respectively. To estimate the errors in the properties from MD, we perform 5 different MD simulations with different initial conditions and obtain 5 sets of mean values of the properties. The estimate of error in the properties from MD are found to be less than 1.0%.

Fig. 3.1 shows the variation of ρ_{avg} and Γ with L. We observe that, for the channels 2σ to 20σ, $\Gamma < 0$ and $\rho_{\text{avg}} < \rho_{\text{b}}$. Due to the strong repulsion from the wall atoms, fluid molecules cannot access the volume very close to the walls. Moreover, the layering of particles not only forms the regions of high ($> \rho_{\text{b}}$) densities, but also the regions of low ($< \rho_{\text{b}}$) densities inside a channel. The net effect of the excluded volume and layering is that the total number of fluid molecules inside the channel of a volume V is smaller than the number of molecules in the bulk of the same volume. We also observe that, for the smaller channels with no bulk-like region, Γ oscillates with L. The oscillations in Γ follow the formations of adsorbed layers with increasing L. The minimum in Γ occur when adsorbed particles form an additional layer to arrange in a closely packed structure and reduce the average density.

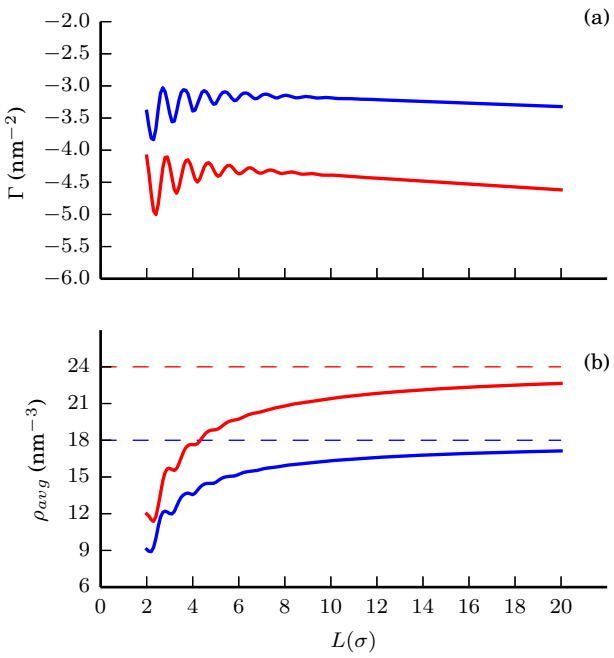

Figure 3.1: EQT-cDFT predictions for total adsorption (a) and average density (b) of methane (blue solid lines) and argon (red solid lines) molecules inside graphene slit channels of various widths. In subfigure b dotted lines correspond to the bulk densities of methane (blue) and argon (red).

Next, we compute the local pressure tensor, surface tension, and solvation force. Fig. 3.2 shows the

lateral pressure profiles in the methane-graphene and argon-graphene systems. It can be observed that the lateral pressure predictions from the EQT-cDFT compare well with the MD for various channel widths. We observe that, in a channel, $P_l(z)$ oscillates similar to $\rho(z)$. The lateral pressure values are much higher near the walls than the bulk pressure. The maximum value of $P_l(z)$ occurs near the first density peak, i.e., 0.95σ from the walls, and it is ≈ 5 times greater than the bulk pressure. Such high pressures in a confined fluid near the channel walls provide explanations for the confined fluid nanophases[85, 86], such as high pressure solid phases [77, 63] and chemical reactions [145]. Away from the walls, the oscillations in $P_l(z)$ decay towards the bulk value.

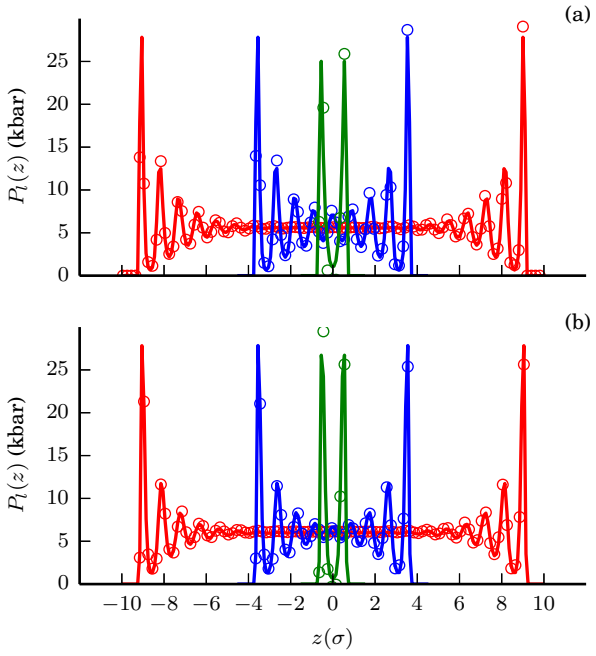

Figure 3.2: Comparison of lateral pressure profiles of methane (a) and argon (b) from EQT-cDFT (lines) and MD (circles) simulations for various channel widths: 20σ (red), 9σ (blue), and 3σ (green).

Fig. 3.3 shows the variation of the normal pressure, surface tension, and solvation force as a function of L for both methane-graphene and argon-graphene systems. We observe that the predictions for $P_{\rm n}(L)$, $\gamma(L)$, and $f_{\rm S}(L)$ from the EQT-cDFT simulations compare well with the MD simulations. Fig. 3.3 shows that the normal pressure oscillates with L for channels less than 9σ and it approaches the bulk pressure value for $L > 9\sigma$. The oscillations in the normal pressure are well-known and they arise because of the oscillations in the average density values (see Fig. 3.1) [11, 77, 85, 33, 86]. Similar to the normal pressure, the surface tension and solvation force oscillate for the smaller channels and the amplitudes of oscillations decay rapidly with increasing L.

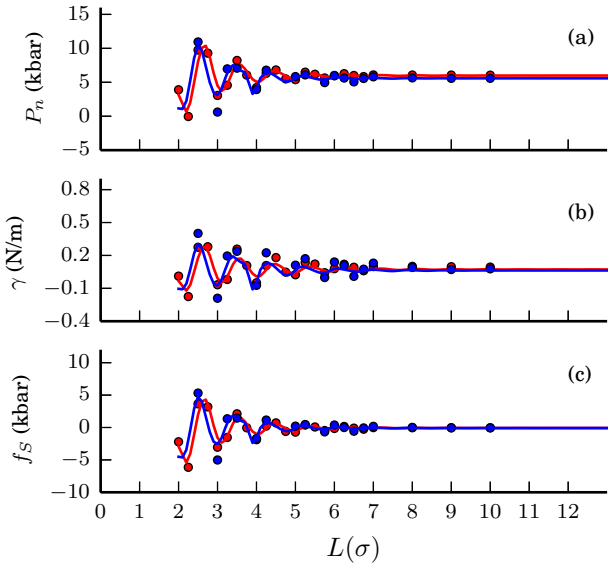

Figure 3.3: Variation of normal pressure (a), surface tension (b), and solvation force (c) of methane (blue) and argon (red) with channel width. Lines are EQT-cDFT results and circles are MD results.

3.5 Summary

In this chapter, we presented an EQT-cDFT approach, in which the density and potentials from EQT are used to model the grand potential functional of a confined fluid. Then the expressions for various thermodynamic properties are derived. We demonstrated the EQT-cDFT approach by simulating methane and argon confined in slit-like graphene channels of various widths. The EQT-cDFT predictions for the thermodynamic properties, like adsorption, local pressure tensor, surface tension, and solvation force, compare well with MD simulations.

Chapter 4

Multiscale model for confined water

We develop a multiscale model to study properties of water confined inside slit-like channels by two multiscale simulation approaches: the coarse-grained molecular dynamics (CG-MD) and the empirical potential-based quasi-continuum theory (EQT). For multiscale model development, we systematically coarse-grain degrees of freedom of confined water from the detailed all-atom level to the cheaper particle-based CG level, and to the continuum-based level. There exists many different AA level models for water with varied degrees of complexity and accuracy [72, 150]. Here, we use the extended simple point charge (SPC/E) [15] model for the AA level confined water simulations. Though particle-based CG systems are simulated using similar molecular simulation techniques as in AA simulations, they allow faster computations due to reduced degrees of freedom and simpler interaction potentials as compared to AA models. For continuum-based simulation, we use EQT.

4.1 Confined water systems

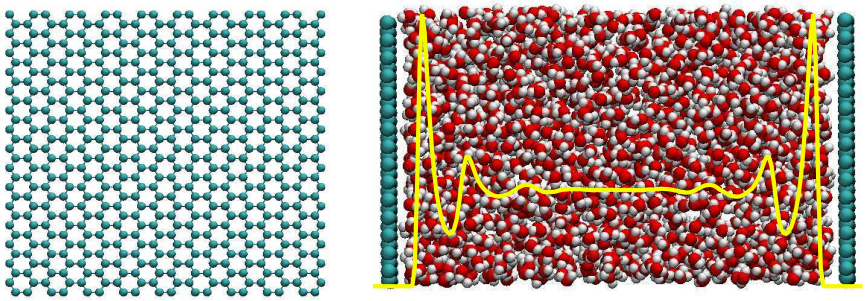

Figure 4.1: Schematic representation of confined water system.

We consider confined water systems in which water molecules are confined between two flat parallel graphene layers as shown in Fig. 4.1. The two graphene layers are placed along the XY plane, and the lateral dimensions of the layers are 3.83400×3.68927 nm^2. The z coordinate is perpendicular to the graphene layers and the separation distance between the two graphene layers is varied from 2σ to 20σ, where σ ($= 0.317$ nm)

is the length-scale parameter for the Lennard-Jones interaction between oxygen atoms of water molecules. For all channel widths, the confined water is assumed to be in equilibrium with a bulk reservoir, and the thermodynamic state of the confined water is defined by the corresponding bulk reservoir temperature and density. We consider various thermodynamic states, from ambient (298 K) to supercritical conditions (673 K) with a range of densities between 0.66 and 1.0 g/cm^3 similar to the one considered in ref. [95].

The reference all-atom molecular dynamic (AA-MD) simulations are performed in the NVT (canonical) ensemble by GROMACS [62]. In MD simulations, the total number of molecules, N, of the confined fluid, which is in equilibrium with the bulk fluid at a given density and temperature, must be specified *a priori*. N can be obtained if we know the average density of the confined fluid defined as, $\rho_{\text{avg}} = N/V_{\text{channel}}$, where V_{channel} is the volume of the channel. It is, therefore, required to determine ρ_{avg} of confined water for various separations of the channel walls. In this work, to determine the average density of confined water in equilibrium with the bulk water at a given thermodynamic state, we adopt the linear superposition approximation (LSA), as described in[30]. It was shown in [30], that ρ_{avg} of confined water at various separations obtained using LSA is thermodynamically consistent except at very small separations. Hence, we use LSA to determine ρ_{avg} for channels of widths larger than 4σ, and for smaller channels, we performed equilibration simulations with the channel attached to the bulk water reservoir at the saturated liquid density for the corresponding temperature and saturation pressure which are obtained from [130].

In AA-MD, water is modeled using the extended simple point charge (SPC/E) [15] model. The interaction parameters are given in Table 4.1. Spherical cutoff of 1.5 nm is used for the Lennard-Jones interactions, and electrostatic interactions are computed by the particle mesh Ewald (PME) [29] method with an extra vacuum of 19 nm above the graphene layer along with the appropriate correction for the slab geometry. Wall atoms are kept fixed at their original positions. Periodic boundary conditions are specified in the x, y, and z directions. Temperature is maintained using the Nosé-Hoover thermostat [108] with 0.2 ps time constant. All systems are equilibrated for 5 ns and production runs of 45 ns are performed with 1 fs time step.

Table 4.1: Interaction parameters in all-atom MD simulations of water confined in graphene slit channels

	σ (nm)	ϵ (kJ/mol)	q (e)
O	0.317	0.6503	-0.8476
H	0.0	0.0	0.4238
C	0.3390	0.2334	0.0
C-O	0.3280	0.3896	-

4.2 Systematic coarse-graining of confined water

In multiscale simulations, it is important that the individual models on different levels of resolution are systematically linked such that these models are thermodynamically and/or structurally consistent. This scale-bridging can be achieved by appropriately devising the effective interaction potentials at different levels of resolution. The process of determining effective interactions at coarser-level from more detailed high resolution level is referred to as the systematic coarse-graining[110, 111, 103, 149, 107].

In the multiscale model for confined water, we represent one water molecule with one coarse-grained bead at the center of mass (COM) and retain all the atomistic details of the graphene layers. In this representation of the confined water system, we need to specify the effective interaction potentials between water-water CG beads and between graphene-water CG beads. We first optimize coarse-grained interactions for the CG-MD scale from the reference AA-MD results and then obtain the effective interactions for the EQT-based continuum scale from the CG-MD scale as depicted in Fig. 4.2.

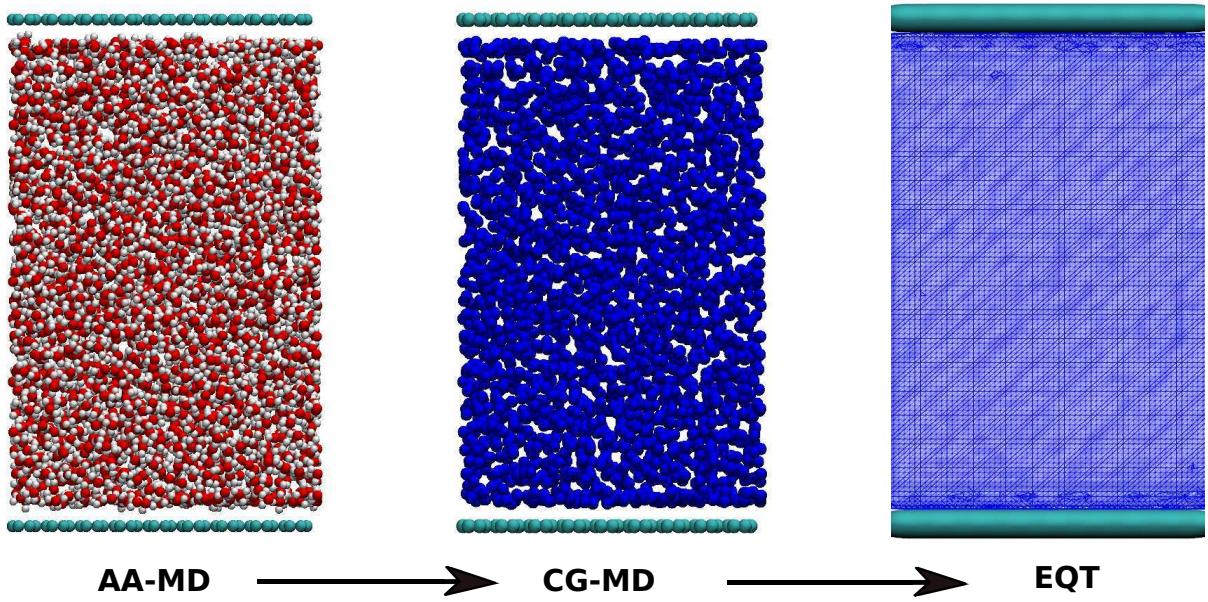

Figure 4.2: Schematic representation of systematic coarse-graining of confined water system from AA-MD to CG-MD to EQT.

4.3 CG-MD model for confined water

To optimize CG potentials for CG-MD scale from a reference high resolution AA-MD system, there exist several systematic coarse-graining techniques of varying complexities and accuracies. These range from structure-based methods, such as Boltzmann inversion, iterative Boltzmann inversion (IBI) [119], inverse

monte carlo (IMC) [90], and relative entropy [133], to force-based methods like force matching (FM) [67, 125]. Structure-based methods target (multi-body) distribution functions and use the relation between the distribution functions and the potential of mean force (PMF) [119, 125] to derive effective CG interactions. In contrast, the FM method tries to reproduce forces on CG sites [125]. Detailed descriptions about the various aspects and methods for determining CG potentials can be found in ref. [103, 110, 25, 126, 125].

In general, coarse-grained potentials cannot reproduce simultaneously all the thermodynamic and structural properties of the reference system [87, 69, 151]. Here, the property of interest for coarse-graining is the equilibrium center of mass (COM) density profile of confined water obtained by the reference AA-MD simulations. Furthermore, CG potentials suffer from transferability issues, i.e., they are thermodynamic state dependent and may not be accurate for states other than the reference state for which they are optimized [87, 69]. Therefore, first, we focus on obtaining CG potentials for confined water at a standard thermodynamic state of 298 K temperature and 1.0 g/cm^3 density. Then, in Section 4.5, we study the thermodynamic state dependence of CG potentials for confined water.

Due to the inherent inhomogeneity of the confined water system and water's special characteristic of forming directional hydrogen-bonds, it is a formidable problem to parameterize a single-site isotropic CG potential model for confined water. CG potentials have been developed to reproduce structural properties of bulk water, such as radial distribution function (RDF).[151, 24, 67] Structural properties of confined water can, however, be different from bulk properties of water. For example, density, RDF, dipole angle distribution, tetrahedral structure, and other properties of water near the surface are different from bulk water, and depend upon surface characteristics.[27, 74, 92] Hence, CG potentials for bulk water may not capture structure of confined water accurately. However, not much attention has been given to the development of CG potentials for confined water. To our knowledge, there is no systematic method for parameterizing CG potentials to reproduce the inhomogeneous density profiles of confined fluids.

In this work, to optimize CG potentials for the confined water system, we use the relative entropy minimization method[133]. Relative entropy is a metric which quantifies the extent of the configurational phase-space overlap between two molecular ensembles as [156, 133]

$$S_{\mathrm{rel}} = \sum_i p_{\mathrm{AA}}(i) \ln \left(\frac{p_{\mathrm{AA}}(i)}{p_{\mathrm{CG}}\left(M(i)\right)} \right) + \langle S_{\mathrm{map}} \rangle_{\mathrm{AA}}, \tag{4.1}$$

where i is a particular configuration of the atom sites in the AA-MD ensemble, M is the mapping operation to generate a corresponding configuration I of the CG sites, i.e., $I = M(i)$, p_{AA} and p_{CG} are the configurational probabilities based on the AA-MD and CG-MD potentials, respectively, and $\langle S_{\mathrm{map}} \rangle_{\mathrm{AA}}$ is the mapping entropy

due to the average degeneracy of the AA configurations mapping to the same CG configuration, given by

$$S_{\text{map}}(I) = \ln \sum_i \delta_{I,M(i)}, \tag{4.2}$$

where δ is the Kronecker delta function. S_{rel} can be used as a measure of the discrepancies between various properties of the CG system's and the target all-atom (AA) ensemble. It has been shown by Shell S. [133] that one can minimize the relative entropy metric between the model CG system and the target AA system to optimize CG potential parameters such that the CG ensemble would mimic the target AA ensemble. We implemented the relative entropy minimization method in an open-source coarse-graining software called Versatile Object-Oriented Toolkit for Coarse-graining Applications (VOTCA) [126, 98]. In addition to the relative entropy minimization method, VOTCA supports various coarse-graining methods such as IBI, IMC, FM, and Simplex. See Appendix B for the details of the relative entropy minimization method and its implementation in VOTCA.

We note that in the coarse-grained representation of the confined water system, we only coarse-grain water molecules and keep all the atomistic details of the channel wall. This representation is similar to the hybrid simulations approach used in[127], in which part of the system is represented at atomic resolution and the remaining part at coarse-grained level. In the reference SPC/E water-based all-atom model, carbon atoms of the graphene layers are modeled as simple LJ-type atoms, and hence, the interaction between a carbon atom and a water molecule is already a single-site isotropic potential.

First, we test the bulk based water-water CG potential in confinement. For the interaction between carbon atoms and CG water beads, we use the LJ potential with the same parameters as the LJ interactions between carbon and oxygen in the reference all-atom system. The water-water CG potential is obtained by relative entropy-based coarse-graining of bulk water at 298 K temperature and 1.0 g/cm^3. The details of bulk water coarse-graining are provided in Appendix B. Fig. 4.3 shows the water-water CG potential along with the LJ interaction between a carbon atom and water CG bead. Fig. 4.4 shows the comparison of the CG-MD and AA-MD results for the COM density profiles of water in the 10σ channel. We observe that CG-MD model based on bulk water-water CG potential and LJ potential between carbon and water fails to predict the interfacial layering of water accurately. This is not surprising because the structure of interfacial water is quite different from that of bulk water[92]. Therefore, a bulk based water-water CG potential along with the original carbon-water LJ pair interaction is not sufficient to accurately capture interfacial structure of the confined water. We discussed this issue in detail in [96]. To address this issue, in ref. [96], we used the coarse-grained correction potential between a wall atom and a water CG bead in addition to the original

LJ potential. Here, instead of separately modeling these two types of CG potentials between a wall atom and a water CG bead, we consider a single effective carbon-water CG potential, and optimize it such that it accounts for the surface effects on the water structure.

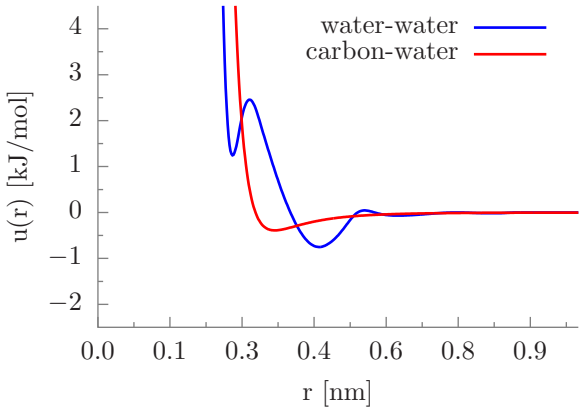

Figure 4.3: Water-water CG potential from bulk water coarse-graining and carbon-water interaction modeled using the carbon-oxygen LJ potential from the reference AA-MD system.

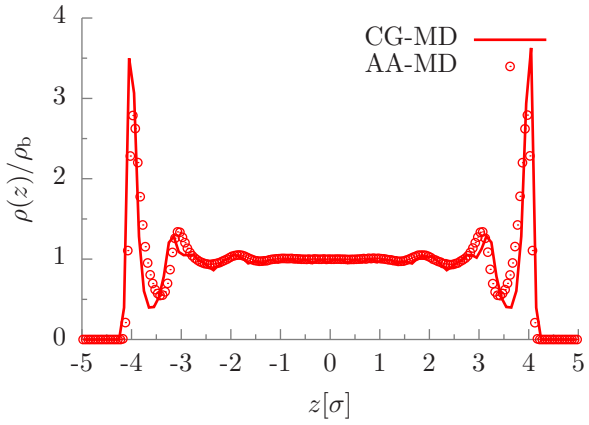

Figure 4.4: Comparison of COM density profile of water from AA-MD and CG-MD with water-water CG potential from bulk water and LJ potential for the carbon-water interactions. The confined water system is 10σ channel at $T = 298$ and $\rho_b = 1.0$ g/cm^3 thermodynamic state.

Next, we optimize water-water and carbon-water CG potentials from a reference 10σ channel AA-MD system. To model the water-water CG-MD potential, $u_{CG}^{ww}(r)$, and the carbon-water CG-MD potential, $u_{CG}^{cw}(r)$, we use a functional form based on uniform cubic B-splines (SP). In a pair potential function, $u_{SP}(r)$, based on uniform cubic B-splines the separation interval from 0 to the cut-off distance, R_{cut}, is discretized into $n-1$ segments, $\{r_0, r_1, r_2, ..., r_{n-1}\}$, of equal size $\Delta r = R_{cut}/(n-1)$ such that $r_i = i \times \Delta r$, where $i \in (0...n-1)$. Then, given $n+2$ real values $\{c_0, c_1, c_2, ..., c_{n+1}\}$ called the spline knots, the value of

a pair potential at a separation distance r is determined by

$$u_{\mathrm{SP}}(r) = \begin{bmatrix} 1 & t & t^2 & t^3 \end{bmatrix} \frac{1}{6} \begin{bmatrix} 1 & 4 & 1 & 0 \\ -3 & 0 & 3 & 0 \\ 3 & -6 & 3 & 0 \\ -1 & 3 & -3 & 1 \end{bmatrix} \begin{bmatrix} c_j \\ c_{j+1} \\ c_{j+2} \\ c_{j+3} \end{bmatrix} \tag{4.3}$$

where the index j is determined such that $r_j \leq r < r_{j+1}$, and t is given by

$$t = \frac{r - r_j}{\Delta r} \tag{4.4}$$

The SP potential form, $u_{\mathrm{SP}}(r)$, is not only suitable for analytical treatment but it also exhibits remarkable flexibility and can represent various complex functional characteristics of pair potentials for sufficiently large number of knots. In this work, for both $u_{\mathrm{CG}}^{\mathrm{ww}}(r)$ and $u_{\mathrm{CG}}^{\mathrm{cw}}(r)$, we set $R_{\mathrm{cut}} = 1.0$ nm with a grid spacing of $\Delta r = 0.02$ nm, i.e., $n = 51$. Thus, we need to optimize a total of 53 knot values for each CG-MD potential, i.e., the knot values $\{c_{0,\mathrm{CG}}^{\mathrm{ww}}, c_{1,\mathrm{CG}}^{\mathrm{ww}}, c_{2,\mathrm{CG}}^{\mathrm{ww}}, ..., c_{52,\mathrm{CG}}^{\mathrm{ww}}\}$ for the water-water CG-MD potential and the knot values $\{c_{0,\mathrm{CG}}^{\mathrm{cw}}, c_{1,\mathrm{CG}}^{\mathrm{cw}}, c_{2,\mathrm{CG}}^{\mathrm{cw}}, ..., c_{52,\mathrm{CG}}^{\mathrm{cw}}\}$ for the carbon-water CG-MD potential.

We determine the optimum spline knots for $u_{\mathrm{CG}}^{\mathrm{ww}}(r)$ and $u_{\mathrm{CG}}^{\mathrm{cw}}(r)$ by relative entropy minimization using the trajectory of the reference 10σ channel AA-MD simulations. Fig. 4.5 shows the carbon-water and water-water CG-MD potentials obtained by the relative entropy minimization. We evaluate these CG-MD potentials for their ability to predict the COM density profile of the confined water by performing the CG-MD simulations. Fig. 4.6 shows the CG-MD results for the COM density profile of water in the reference 10σ channel. It is evident that the CG-MD potentials predict the COM density profile of the confined water accurately as compared to the reference AA-MD results, and it is found that the root-mean-squared deviation (RMSD) between the CG-MD and AA-MD results is less than 0.055.

4.4 EQT model for confined water

As described in Chapter 2, to determine the density profile of confined water from EQT, we need effective carbon-water and water-water pair potentials. It was shown that, to determine the wall-fluid potential from Eq. 2.5, one can use the particle-based effective single-site isotropic pair potential between a wall particle and a fluid particle. Thus, to compute the wall-fluid potential, U^{wf}, for the confined water, we use the

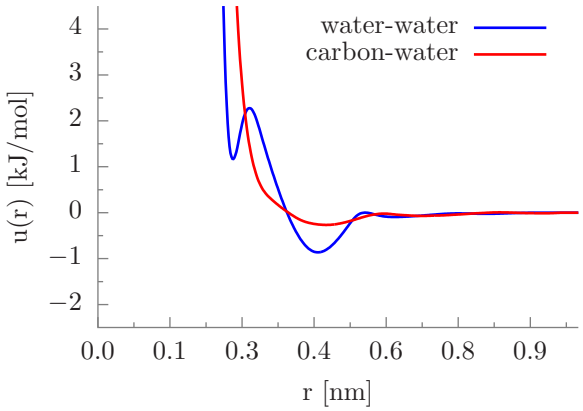

Figure 4.5: Water-water and carbon-water CG potentials for the CG-MD scale for $T = 298$ and $\rho_b = 1.0$ g/cm^3 thermodynamic state.

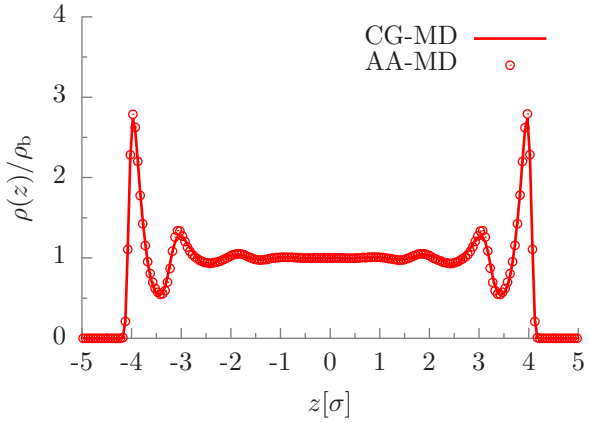

Figure 4.6: Comparison of COM density profile of water from CG-MD and AA-MD simulations inside 10σ channel at $T = 298$ and $\rho_b = 1.0$ g/cm^3 thermodynamic state.

carbon-water CG pair potential, $u^{cw}_{CG}(r)$, optimized for the CG-MD scale as

$$U^{wf}(\boldsymbol{r}) = \int \rho_{wall}(\boldsymbol{r}')u^{cw}_{CG}(r)d\boldsymbol{r}', \tag{4.5}$$

where, $\rho_{wall} = 38.18$ atoms/nm^3 for the graphene wall.

Here, we use the soft-core potential approach to compute the fluid-fluid potential due to water-water interactions as

$$U^{ff}(\boldsymbol{r}) = \int \rho(\boldsymbol{r}')u^{ww}_{EQT}(r)d\boldsymbol{r}' \tag{4.6}$$

where $u^{ww}_{EQT}(r)$ is the water-water effective quasi-continuum pair potential. One should model $u^{ww}_{EQT}(r)$, such that it is finite for $r \to 0$, and it should take into account the effects of the neglected pair correlations

in the mean-field approximation (MFA) of Eq. 4.6 [96]. Therefore, we model the water-water effective quasi-continuum pair potential, $u^{\mathrm{ww}}_{\mathrm{EQT}}(r)$, as

$$u^{\mathrm{ww}}_{\mathrm{EQT}}(r) = \begin{cases} 0, & r \leq R_{\mathrm{crit}} \\ a_0 + a_1(r - R_{\mathrm{min}}) + a_2(r - R_{\mathrm{min}})^2, & R_{\mathrm{crit}} < r \leq R_{\mathrm{min}} \\ u_{\mathrm{SP}}(r), & R_{\mathrm{min}} < r \leq R_{\mathrm{cut}} \end{cases} \tag{4.7}$$

where R_{crit} and R_{min} are the control parameters, which define the zero potential region and the soft-core of $u^{\mathrm{ww}}_{\mathrm{EQT}}(r)$, respectively. The soft-core region is modeled using the quadratic polynomial with the coefficients a_0, a_1, and a_2. Similar approach of modeling the soft-core of the fluid-fluid quasi-continuum pair potentials to ensure the finite potential values for small r is followed previously in [117, 6, 129, 96]. In the region from R_{min} to the cut-off distance R_{cut}, $u^{\mathrm{ww}}_{\mathrm{EQT}}(r)$ is modeled using the uniform cubic B-splines form, $u_{\mathrm{SP}}(r)$, given by Eq. 4.3. In this work, we optimize a_1, a_2, and the cubic B-spline knot values of $u^{\mathrm{ww}}_{\mathrm{EQT}}(r)$ in Eq. 4.7, i.e., $\boldsymbol{\lambda} = \{a_1, a_2, c^{\mathrm{ww}}_{0,\mathrm{EQT}}, c^{\mathrm{ww}}_{1,\mathrm{EQT}}, c^{\mathrm{ww}}_{2,\mathrm{EQT}}, ...\}$. We fix $R_{\mathrm{crit}} = 0.05$ nm, $R_{\mathrm{min}} = 0.26$ nm, $R_{\mathrm{cut}} = 1.04$ nm, and use grid spacing of 0.08 nm for the cubic B-spline part of $u^{\mathrm{ww}}_{\mathrm{EQT}}(r)$. a_0 is determined by imposing the C^0 continuity condition at R_{min}.

Here, we develop a systematic technique to optimize the parameters $\boldsymbol{\lambda}$ of $u^{\mathrm{ww}}_{\mathrm{EQT}}(r)$ such that the target equilibrium COM density profile, $\rho^{\mathrm{tgt}}(z)$, of the confined water can be reproduced by EQT. Similar to the IBI method, in which, to reproduce the target RDF, the CG potential is optimized such that the Boltzmann relation between the two-body PMF and the RDF is satisfied, for reproducing $\rho^{\mathrm{tgt}}(z)$ the parameters of $u^{\mathrm{ww}}_{\mathrm{EQT}}(r)$ must satisfy the Boltzmann relation given by

$$\rho(z) = \rho_{\mathrm{ref}} \exp\left(-\frac{\bar{U}(z)}{k_{\mathrm{B}}T}\right), \tag{4.8}$$

where $\bar{U}(z) = (U(z) - U_{\mathrm{ref}})$. For the slit-like graphene-water system, we use the midpoint of the channel as the reference point. Therefore, to quantify the accuracy of $u^{\mathrm{ww}}_{\mathrm{EQT}}(r)$ parameters, we define the metric:

$$\epsilon_{\mathrm{B}} = \frac{1}{2L}\int_0^L \left(\rho^{\mathrm{tgt}}_{\mathrm{ref}} \exp\left(-\frac{\bar{U}(z)}{k_{\mathrm{B}}T}\right) - \rho^{\mathrm{tgt}}(z)\right)^2 dz \tag{4.9}$$

where $\rho^{\mathrm{tgt}}_{\mathrm{ref}}$ is the target density at the reference point and $U(z)$ is determined by using the target density profile, $\rho^{\mathrm{tgt}}(z)$. The quantity ϵ_{B} in Eq. 4.9 gives the average squared error in the Boltzmann relation due to the given parameters of $u^{\mathrm{ww}}_{\mathrm{EQT}}(r)$. Hence, the objective is to determine the parameters of $u^{\mathrm{ww}}_{\mathrm{EQT}}(r)$ such that the quantity ϵ_{B} is minimized. Since, minimizing ϵ_{B} is equivalent to reproducing the target total PMF

profile, it is in essence a PMF-matching technique.

Similar to the relative entropy minimization as described in Appendix B, for the minimization of ϵ_{B}, we use the coupled Newton-Raphson scheme such that the parameters of $u_{\mathrm{EQT}}^{\mathrm{ww}}(r)$, $\boldsymbol{\lambda}$, are refined iteratively as

$$\boldsymbol{\lambda}^{k+1} = \boldsymbol{\lambda}^{k} - \chi {\mathbf{H}_{\epsilon_{\mathrm{B}}}}^{-1} \cdot \nabla_{\lambda}\epsilon_{\mathrm{B}} \tag{4.10}$$

where k is the iteration index, $\chi \in (0...1)$ is the relaxation parameter that can be adjusted to ensure convergence, $\nabla_{\lambda}\epsilon_{\mathrm{B}}$ is the vector of the first derivatives of ϵ_{B} with respect to $\boldsymbol{\lambda}$, and $\mathbf{H}_{\epsilon_{\mathrm{B}}}$ is the Hessian matrix of ϵ_{B}. $\nabla_{\lambda}\epsilon_{\mathrm{B}}$ can be computed from Eq. 4.9 as

$$\nabla_{\lambda}\epsilon_{\mathrm{B}} = -\frac{1}{L}\int_{0}^{L} \frac{1}{RT}\rho_{\mathrm{ref}}^{\mathrm{tgt}} \exp\left(-\frac{\bar{U}(z)}{k_{\mathrm{B}}T}\right)\left(\rho_{\mathrm{ref}}^{\mathrm{tgt}} \exp\left(-\frac{\bar{U}(z)}{k_{\mathrm{B}}T}\right) - \rho^{\mathrm{tgt}}(z)\right)\frac{\partial \bar{U}(z)}{\partial \lambda} dz \tag{4.11}$$

and $\mathbf{H}_{\epsilon_{\mathrm{B}}}$ is given by

$$\begin{aligned}
\mathbf{H}_{ij,\epsilon_{\mathrm{B}}} \quad = \quad & \frac{1}{L}\int_{0}^{L} \left(\frac{1}{k_{\mathrm{B}}T}\right)^{2} \rho_{\mathrm{ref}}^{\mathrm{tgt}} \exp\left(-\frac{\bar{U}(z)}{k_{\mathrm{B}}T}\right)\left(\rho_{\mathrm{ref}}^{\mathrm{tgt}} \exp\left(-\frac{\bar{U}(z)}{k_{\mathrm{B}}T}\right) - \rho^{\mathrm{tgt}}(z)\right)\frac{\partial \bar{U}(z)}{\partial \lambda_i}\frac{\partial \bar{U}(z)}{\partial \lambda_j} dz \\
& + \frac{1}{L}\int_{0}^{L} \left(\frac{1}{k_{\mathrm{B}}T}\rho_{\mathrm{ref}}^{\mathrm{tgt}} \exp\left(-\frac{\bar{U}(z)}{k_{\mathrm{B}}T}\right)\right)^{2} \frac{\partial \bar{U}(z)}{\partial \lambda_i}\frac{\partial \bar{U}(z)}{\partial \lambda_j} dz \\
& - \frac{1}{L}\int_{0}^{L} \frac{1}{k_{\mathrm{B}}T}\rho_{\mathrm{ref}}^{\mathrm{tgt}} \exp\left(-\frac{\bar{U}(z)}{k_{\mathrm{B}}T}\right)\left(\rho_{\mathrm{ref}}^{\mathrm{tgt}} \exp\left(-\frac{\bar{U}(z)}{k_{\mathrm{B}}T}\right) - \rho^{\mathrm{tgt}}(z)\right)\frac{\partial^{2} \bar{U}(z)}{\partial \lambda_i \partial \lambda_j} dz
\end{aligned} \tag{4.12}$$

Since $\boldsymbol{\lambda}$ in Eq. 4.10 contains only the parameters of the water-water pair potential, $u_{\mathrm{EQT}}^{\mathrm{ww}}(r)$, only the water-water potential profile contributes to the first and second derivatives of $\bar{U}(z)$ in Eqs. 4.11 and 4.12, and they can be computed as

$$\frac{\partial \bar{U}(z)}{\partial \lambda_i} = \frac{\partial U^{\mathrm{ff}}(z)}{\partial \lambda_i} - \frac{\partial U^{\mathrm{ff}}(z_{\mathrm{ref}})}{\partial \lambda_i} \tag{4.13a}$$

$$\frac{\partial^{2} \bar{U}(z)}{\partial \lambda_i \lambda_j} = \frac{\partial^{2} U^{\mathrm{ff}}(z)}{\partial \lambda_i \lambda_j} - \frac{\partial^{2} U^{\mathrm{ff}}(z_{\mathrm{ref}})}{\partial \lambda_i \lambda_j} \tag{4.13b}$$

where $\frac{\partial U^{\mathrm{ff}}}{\partial \lambda_i}$ and $\frac{\partial^{2} U^{\mathrm{ff}}}{\partial \lambda_i \lambda_j}$ are given by

$$\frac{\partial U^{\mathrm{ff}}(r)}{\partial \lambda_i} = \int \rho(r') \frac{\partial u_{\mathrm{EQT}}^{\mathrm{ww}}(|r-r'|)}{\partial \lambda_i} dr' \tag{4.14a}$$

$$\frac{\partial^{2} U^{\mathrm{ff}}(r)}{\partial \lambda_i \lambda_j} = \int \rho(r') \frac{\partial^{2} u_{\mathrm{EQT}}^{\mathrm{ww}}(|r-r'|)}{\partial \lambda_i \lambda_j} dr' \tag{4.14b}$$

The first derivatives of $u^{\mathrm{ww}}_{\mathrm{EQT}}(r)$ w.r.t. a_1 and a_2 can be computed from Eq. 4.7 as

$$\frac{\partial u^{\mathrm{ww}}_{\mathrm{EQT}}(r)}{\partial a_1} = r - R_{\mathrm{min}} \tag{4.15a}$$

$$\frac{\partial u^{\mathrm{ww}}_{\mathrm{EQT}}(r)}{\partial a_2} = (r - R_{\mathrm{min}})^2 \tag{4.15b}$$

and the first derivatives w.r.t. the knot values of the B-spline part of $u^{\mathrm{ww}}_{\mathrm{EQT}}(r)$ can be computed by Eq. 4.3. The second derivatives of $u^{\mathrm{ww}}_{\mathrm{EQT}}(r)$ w.r.t. $\boldsymbol{\lambda}$ are zero. For the graphene-water slit-like system, we follow the same procedure described in Chapter 2 to determine $U(z)$, $U^{\mathrm{wf}}(z)$, $U^{\mathrm{ff}}(z)$, and the derivatives of $U(z)$.

Fig. 4.7 shows the optimum water-water soft-core pair potential obtained by the PMF-matching method. Similar to the relative entropy coarse-graining for the CG-MD scale, for the PMF-matching, we use the 10σ channel AA-MD system as the target system. We note that the optimum values of a_1,a_2, and the cubic B-spline knot values for $u^{\mathrm{ww}}_{\mathrm{EQT}}(r)$ depend significantly on the choice of R_{crit} and R_{min} values. Herein, we set $R_{\mathrm{crit}} = 0.05$ nm and $R_{\mathrm{min}} = 0.26$ nm such that the optimized $u^{\mathrm{ww}}_{\mathrm{EQT}}(r)$ follows as closely as possible the characteristics of the CG-MD water-water potential in the region from R_{min} to R_{cut}. It can be observed that, for each thermodynamic state, though the water-water EQT potential has the same core-softened double-well-type characteristics as in the CG-MD case, it's length-scales are slightly shifted and energy-scales are more attractive as compared to the CG-MD water-water potential. This behaviour can be contributed to the MFA of Eq. 4.6 [148]. The MFA neglects the water-water pair correlations which should enhance the attractive interactions. Hence, the effective water-water EQT potentials are more attractive to account for the effects of the pair correlation. Furthermore, from Fig. 4.8, we observe that the soft-core CG potential is similar to the water-water direct correlation, $c(r)$, [52], which is computed from the water-water radial distribution function in the bulk. This suggests that the soft-core potential form does not only address the numerical issues due to a steep-repulsion component of the fluid-fluid pair potential in the continuum approximation but also accurately captures the fluid-fluid correlations in the confined system.

Next, we evaluate the soft-core CG potential for its ability to predict the COM density profile of the confined water by performing the EQT simulations. From Fig. 4.9, it is evident that the CG potentials based EQT predicts the COM density profile of the confined water accurately as compared to the reference AA-MD results, and it is found that the RMSD between the EQT and AA-MD results is less than 0.044.

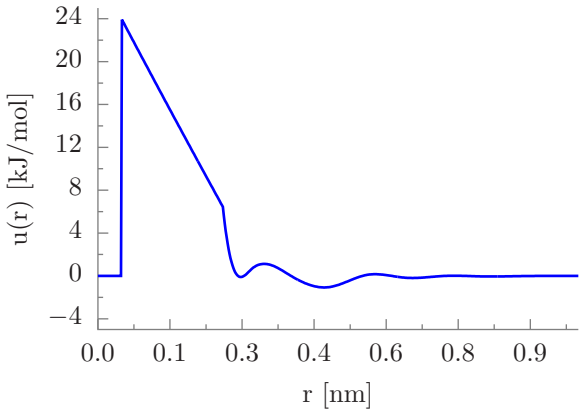

Figure 4.7: Water-water soft-core CG potential for the EQT-based continuum scale for $T = 298$ and $\rho_b = 1.0$ g/cm^3 thermodynamic state.

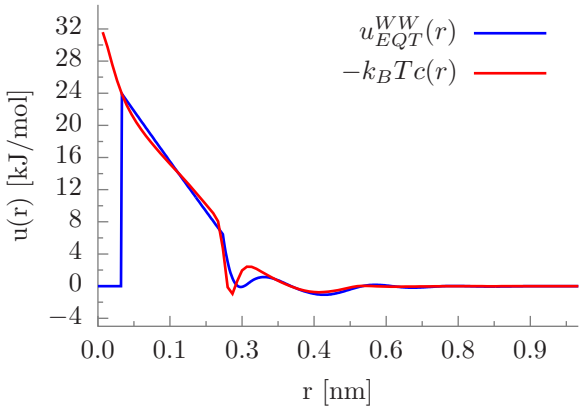

Figure 4.8: Comparison of the water-water soft-core CG potential and the bulk water-water direct correlation function for $T = 298$ and $\rho_b = 1.0$ g/cm^3 thermodynamic state.

4.5 Transferability

First we test the transferability of the CG potentials optimized for the 10σ channel to different channel widths at the same thermodynamic state of $T = 298$ and $\rho_b = 1.0$ g/cm^3. Fig. 4.10 shows that the density profiles from CG-MD and EQT compare well with the reference AA-MD results for different channel widths. Therefore, the CG potentials are transferable across different channel widths at the same thermodynamic state.

Next, we study the thermodynamic state dependence of the CG potentials for confined water. Since the average contributions of the coarse-grained atomic degrees of freedom depend on the thermodynamic state of the reference system, CG potentials suffer from transferability issues, i.e., CG potential constructed from a reference system at a given thermodynamic state may not directly be used for modeling the underlying

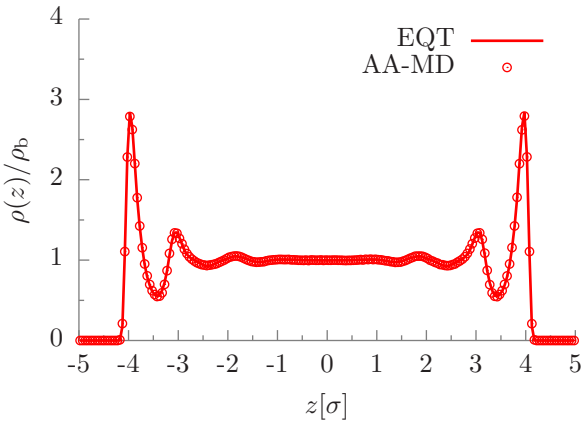

Figure 4.9: Comparison of COM density profile of water from EQT using the soft-core water-water CG potential and AA-MD simulations inside 10σ channel at $T = 298$ and $\rho_b = 1.0$ g/cm^3 thermodynamic state.

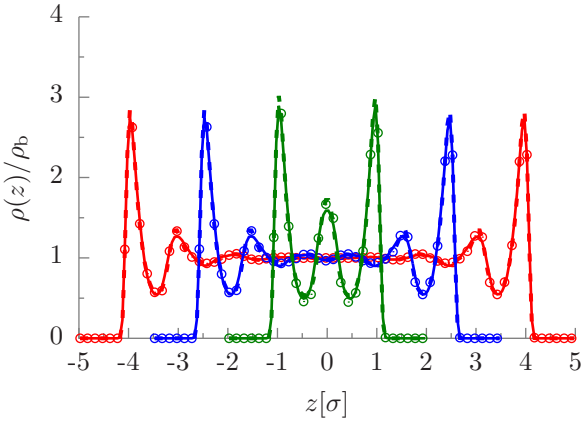

Figure 4.10: Comparison of COM density profiles of water from AA-MD, CG-MD, and EQT simulations for different channel widths at $T = 298$ and $\rho_b = 1.0$ g/cm^3 thermodynamic state:10σ (red), 7σ (blue), and 4σ (green). Circles are AA-MD results, solid lines are CG-MD results, and dashed lines are EQT results.

sytem at a different state point [87, 69]. Therefore, we generate different set of CG-MD and EQT soft-core potentials for each thermodynamic state of the confined water, given in Table 4.2. For both, the relative entropy minimization and the PMF-matching based coarse-graining, we use the 10σ channel AA-MD system as the target system.

Fig. 4.11 shows the carbon-water and water-water CG-MD potentials and water-water soft-core EQT CG potentials for different thermodynamic states. Fig. 4.12 shows that the CG-MD and EQT results for the COM density profiles of water compare well with the reference AA-MD results in multiple channel widths at different thermodynamic states.

From Fig. 4.11, further observations can be made about the state dependent characteristics of the water-water and carbon-water CG potentials. It can be seen that both the CG-MD pair potentials depend sub-

Table 4.2: Thermodynamic states of confined water.

State	T [K]	ρ [gm/cm^3]
I	298	1.0
II	328	0.985
III	400	0.935
IV	523	0.8
V	673	0.66

stantially on the thermodynamic state. However, water-water CG-MD potential exhibits a characteristic core-softened double-well-type form at all the states considered. This observation is consistent with the studies of single-site isotropic potentials for water [67, 160, 69, 161, 24]. There are two important energy and length-scales to core-softened double-well-type potential form. We find that, for the water-water CG-MD potential, the energy-scale of the first well varies significantly with the thermodynamic state: it continuously falls from positive values at lower temperatures to negative values at higher temperatures. The second-well is always attractive and does not vary significantly with the thermodynamic state. Also, we note that the difference between the second inflection point and the second energy well decreases with increasing temperature. Wang et al. [151] suggest that this difference governs the tetrahedral packing of water molecules: the larger the difference, the stronger the tetrahedral packing. This implies that for the graphene-water system as temperature increases the tetrahedral packing of water molecules becomes weaker, which is physically consistent with the observations by Martí and Guàrdia [95] that as temperature increases the number of hydrogen bonds per water molecule decreases. In contrast to the significant state dependence of the energy-scales, both the length-scales, i.e., locations of the first and second well, vary very little with the state, and the ratio of the two length-scales is in the range 0.61-0.67, which is in agreement with the observation made by Yan et al. [160], that in order to have water-like characteristics this ratio should be ≈ 0.6. Similar observations are made by Chaimovich and Shell [24] about the thermodynamic state dependence of the energy and length-scales of the coarse-grained bulk water potential.

Although, the CG potentials are significantly state-dependent, one can transfer a CG potential optimized for a particular thermodynamic state to a different state by an appropriate state-dependent scaling relation [37]. Such scaling relations, if exist, can be useful to derive CG potentials for wider thermodynamic states from the CG potentials of a few representative states which are optimized explicitly by a coarse-graining technique. Farah et al. [37] used a 2-point linear interpolation formula given by

$$u(r,T) = C_{\mathrm{L}} \times u(r,T_{\mathrm{L}}) + C_{\mathrm{U}} \times u(r,T_{\mathrm{U}}) \tag{4.16}$$

to determine the temperature dependent CG potentials for liquid n-hexane in a region of homogeneous

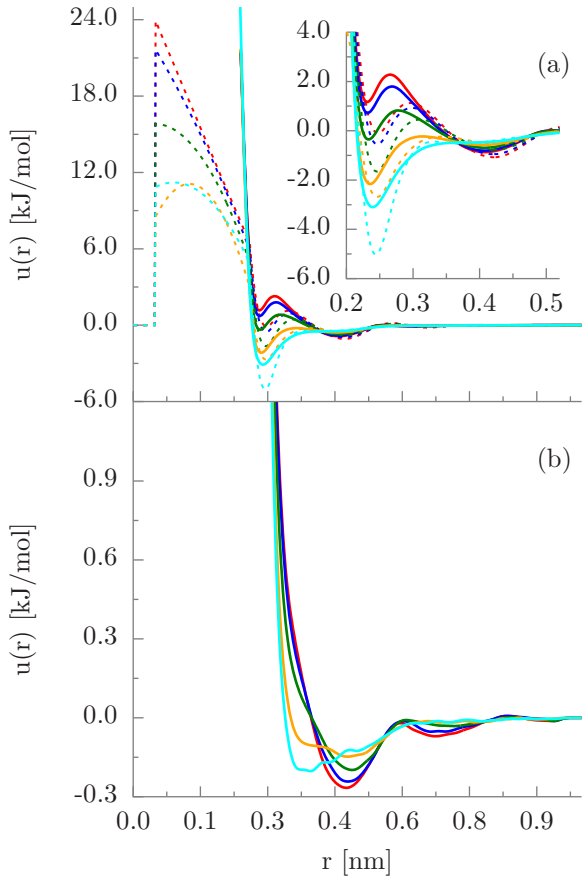

Figure 4.11: Coarse-grained effective potentials for CG-MD and EQT simulations at different thermodynamic states. The top subfigure shows water-water potentials where solid lines are CG-MD potentials and dashed lines are EQT potentials. The bottom subfigure shows carbon-water potentials. In both the subfigures, red lines are for T = 298 K, blue for T = 328 K, green for T = 400 K, orange for T = 523 K, and cyan for T = 673 K.

phases. In Eq. 4.16, the CG potential at temperature T, $u(r,T)$, is determined from the two known CG potentials $u(r,T_{\mathrm{L}})$ and $u(r,T_{\mathrm{U}})$ at temperatures T_{L} and T_{U}, where $T_{\mathrm{L}} \leq T \leq T_{\mathrm{U}}$, and C_{L} and C_{U} are the mixing coefficients given by

$$C_{\mathrm{L}} = \frac{T_{\mathrm{U}} - T}{T_{\mathrm{U}} - T_{\mathrm{L}}} \tag{4.17a}$$

$$C_{\mathrm{U}} = \frac{T - T_{\mathrm{L}}}{T_{\mathrm{U}} - T_{\mathrm{L}}} \tag{4.17b}$$

Herein, we test the applicability of 2-point linear interpolation formula for the confined water by evaluating the accuracy of the CG potentials derived for the saturated liquid water states: $T = 310$ K, $\rho = 0.9933$ gm/cm^3 and $T = 473$ K, $\rho = 0.863$ gm/cm^3. For $T = 310$ K we use $T_{\mathrm{L}} = 298$ K and $T_{\mathrm{U}} = 328$ K, and for $T = 473$ K we use $T_{\mathrm{L}} = 400$ K and $T_{\mathrm{U}} = 523$ K. The CG-MD and EQT potentials obtained by this procedure are shown in Fig. 4.13. From Fig. 4.14, it is evident that the density profiles of water predicted

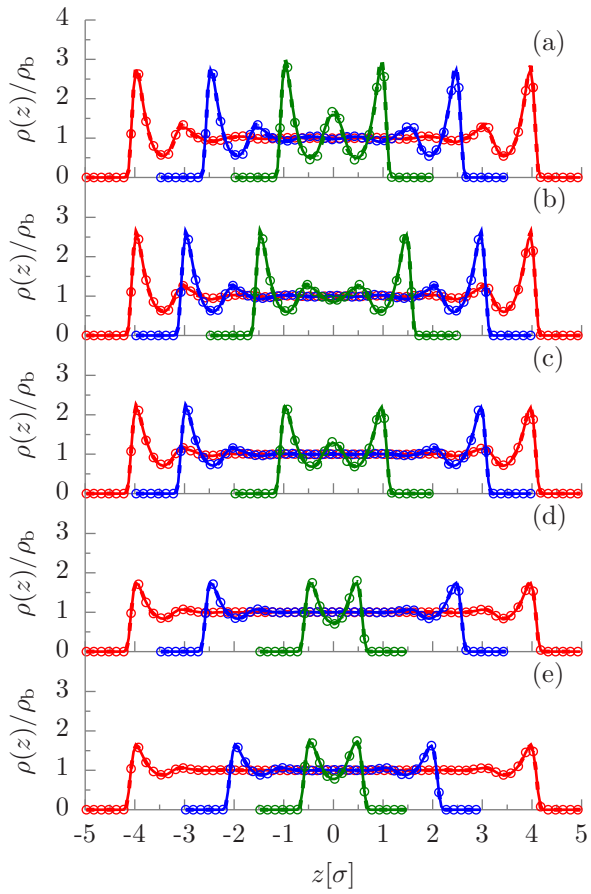

Figure 4.12: Comparison of COM density profiles of water from AA-MD, CG-MD, and EQT simulations at different thermodynamic states and channel widths: (a) T = 298 K, 10σ (red), 7σ (blue), and 4σ (green); (b) T = 328 K, 10σ (red), 8σ (blue), and 5σ (green); (c) T = 400 K, 10σ (red), 8σ (blue), and 4σ (green); (d) T = 523 K, 10σ (red), 7σ (blue), and 3σ (green); and (e) T = 673 K, 10σ (red), 6σ (blue), and 3σ (green). In all subfigures, circles are AA-MD results, solid lines are CG-MD results, and dashed lines are EQT results.

by the scaled CG-MD and EQT potentials are in reasonably good agreement with the reference AA-MD results. Therefore, it is clear that the 2-point linear interpolation can be used to derive state dependent CG potentials for the confined water in the region of the saturated liquid phases. We note that there is a scope to further investigate, in detail, the transferability of the CG potentials for the cofined water in the region of much wider thermodynamic states using the relative entropy minimization and the PMF-matching techniques.

4.6 Summary

In this chapter, we developed coarse-grained potentials to predict the structure of confined water by two multiscale simulation approaches: the coarse-grained molecular dynamics (CG-MD) and the empirical potential-

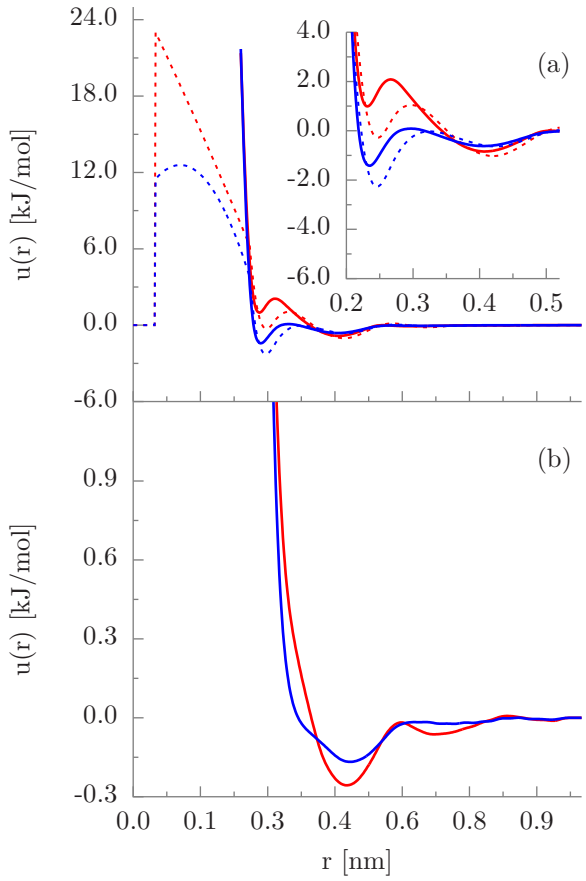

Figure 4.13: Interpolated CG potentials for the confined water. The top subfigure shows water-water potentials where solid lines are CG-MD potentials and dashed lines are EQT potentials. The bottom subfigure shows carbon-water potentials. In both the subfigures, red lines are for T = 310 K, and blue for T = 473 K.

based quasi-continuum theory (EQT). The structurally-consistent coarse-grained potentials for the CG-MD and EQT are determined from the reference all-atom SPC/E water model. For optimization of the CG-MD potentials, the relative entropy-based coarse-graining method is used, and for determination of the EQT potentials, we developed a potential of mean force matching scheme. We found that the density profiles from CG-MD and EQT compare well with the reference AA-MD results for different channel widths. Hence, the CG potentials are transferable across different channel widths at the same thermodynamic state. Furthermore, we studied thermodynamic transferability of the CG potentials and found that the CG potentials depend on the thermodynamic state of confined water.

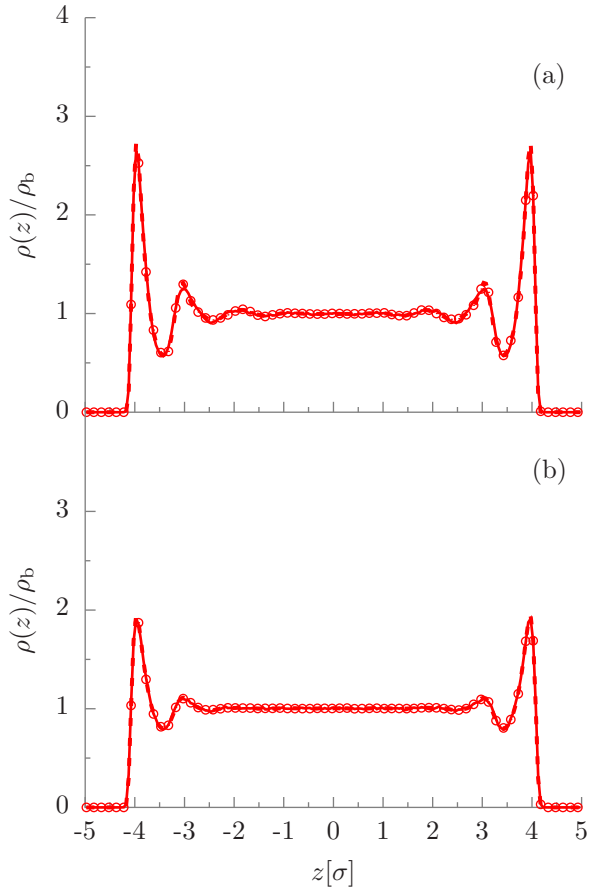

Figure 4.14: Comparison of COM density profiles of water from AA-MD, CG-MD, and EQT simulations using interpolated CG potentials for 10σ channel: (a) T = 310 K and (b) T = 473 K. In both the subfigures, circles are AA-MD results, solid lines are CG-MD results, and dashed lines are EQT results.

Chapter 5

Langevin-Poisson-EQT: A dipolar solvent based quasi-continuum approach for electric double layers

In this chapter, we extend the EQT framework to simulate electric double layers (EDLs).When an electrolyte fluid, which is usually an aqueous solution of ions, interacts with a charged surface, the surface electric field attracts counter ions to form a layer of counter ions near the surface, which is called the "electric double layer" (EDL) [7]. Water is a highly polar solvent. As a result, electrostatic interactions of interfacial water molecules play a dominant role in determining the distribution of ions in electric double layers (EDLs). Near a surface, an inhomogeneous and anisotropic arrangement of water molecules gives rise to pronounced variations in the electrostatic and hydration energies of ions. Therefore, a detailed description of the structural and dielectric properties of water is important to study EDLs.

Most theoretical models ignore the molecular effects of water and treat water as a background continuum with a uniform dielectric permittivity. The Gouy-Chapman (GC) theory based on the Poisson-Boltzmann (PB) equation is the most basic and popular theory to study EDL [3]. It models ions as point charges and incorporates only the electrostatic interactions among them; furthermore, it treats water implicitly as a background medium with a uniform dielectric permittivity. However, it ignores many important molecular aspects of the fluid, such as finite size of the ions, statistical correlations, the van der Waals' (vdW) interactions, molecular nature of water and variations in the dielectric permittivity. Therefore, accuracy of the Gouy-Chapman theory is limited.

To address the limitations of the GC theory, various advanced theories have been developed, such as the modified PB theory [22], integral equation theory [76], and classical density functional theory (cDFT) [36, 158, 83, 41, 82, 128]. These theories, in addition to the electrostatic interactions, mainly account for the finite size effects of ions and van der Waals' interactions among them. However, they usually ignore molecular details of water and variations in the dielectric permittivity. For example, in the most common cDFT approach, which is also known as a primitive model (PM), ions are modeled as charged hard spheres, water is treated as a background continuum with a uniform dielectric permittivity, and then the ion density profiles and EDL properties are obtained by minimizing a free energy functional [68]. In the PM, if all the ions are assumed to have the same hard sphere diameter then it is called a restricted PM (RPM) [140].

The implicit solvent-based methods ignore important molecular details of water and, hence, they fail to predict several key experimental [79] and atomistic simulation results [114, 115]. Near a surface, water molecules are packed in distinct density layers and they exhibit anisotropy in their orientations [94, 26]. Such inhomogeneous and anisotropic arrangement of the interfacial water molecules gives rise to pronounced oscillations in the polarization, dielectric permittivity, electric field, and hydration interactions near the surface [20, 21]. Consquently, the interfacial water has a dominant effect on the electrostatic and hydration energies of ions, which in turn affect the spatial arrangements of ions and electrostatic potential and capacitance of EDL. Therefore, the representation of water as a homogeneous dielectric medium is inaccurate. To accurately predict the properties of EDL, it is necessary to consider molecular details of water explicitly.

There are some approaches which try to incorporate molecular details of water explicitly. The simplest approach is to model water molecules as hard spheres with uniform dielectric permittivity. Hard sphere water model has been used in various cDFT-based studies of EDL, which are also known as three component model (3CM) or molecular solvent model (MSM) [81, 46]. Lee et al. [83] have further incorporated the Lennard-Jones (LJ) interactions among ions, water, and wall particles in the 3CM cDFT. However, the hard sphere model is a very crude approximation for a water molecule and it ignores water-water electrostatic interactions and variations in the orientation and dielectric permittivity of water. To include water orientation and polarization effects, dipolar solvent-based approaches have beeen proposed, such as the Langevin dipole model, [48, 47, 153], dipolar hard sphere model based on mean spherical approxmation (MSA) [18], and dimer solvent-based cDFT [60]. Accuracy of these dipolar solvent-based approaches is limited. For example, dipolar hard sphere MSA is a linear response theory and is limited to small surface charge densities [59]. Moreover, a detailed comparison of the dipolar solvent-based theories with higher fidelity MD simulations has not been performed.

In this chapter, we present an empirical potential-based quasi-continuum theory (EQT) for EDL, which can accurately incorporate the molecular effects of water on the arrangement of ions in EDL. We extend the EQT framework to include the effects of water dipole orientation, polarization, and dielectric permittivity variation near a charged surface. To explicitly incorporate water polarization effects, we systematically develop a point dipole based coarse-grained model of water. We also develop coarse-grained ion-water potentials to accurately capture ion hydration effects. We show that EQT with point dipole water model and ion-water coarse-grained potentials can accurately predict the density profiles of water and ions near a charged surface.

The remainder of the chapter is organized as follows. In Sec. 5.1, we describe the EQT framework for EDL. In Sec. 5.2, we provide the details of systematic coarse-graining to develop a point dipole water model

and ion-water coarse-grained potentials. In Sec. 5.3, we describe the numerical details of EQT and the reference MD simulations. In Sec. 5.4.1, we provide the analysis of the point dipole approach to predict the electrostatic potential profile in EDL. In Sec. 5.4.2, we demonstrate the EQT approach by simulating NaCl aqueous electrolyte confined inside slit-like capacitor channels at various ion concentrations and surface charge densities.

5.1 EQT for EDL

Consider a mixture of cations (+), anions (-), and water (w) molecules confined in a charged slit channel. At equilibrium, the distribution of the fluid molecules is given by the 1-D Nernst-Planck (NP) equation,

$$\frac{d}{dz}\left(\frac{d\rho_i}{dz}+\frac{\rho_i}{k_{\mathrm{B}}T}\frac{dU_i}{dz}\right)=0 \tag{5.1}$$

with boundary conditions

$$\rho_i(0)=0 \tag{5.2a}$$

$$\rho_i(L)=0 \tag{5.2b}$$

$$\frac{1}{L}\int_0^L \rho_i(z)\,dz=\rho_{i,\mathrm{avg}} \tag{5.2c}$$

where, ρ_i and U_i are the density and total potential of the molecule i (= +, -, w), respectively, T is the fluid temperature, k_{B} is the Boltzmann constant, L is the channel width, $\rho_{i,\mathrm{avg}}$ is the average density of the molecule i inside the channel, and z-axis is normal to the wall. The solution of Eqs. 5.1 and 5.2 is equivalent to the solution of the Boltzmann distribution equation,

$$\rho_i(z)=\rho_{i,\mathrm{ref}}\exp\left(-\frac{U_i(z)-U_{i,\mathrm{ref}}}{k_{\mathrm{B}}T}\right), \tag{5.3}$$

where $\rho_{i,\mathrm{ref}}$ and $U_{i,\mathrm{ref}}$ are the reference density and potential of the molecule i, respectively. For the electrolyte system, the total potential energy can be split into the electrostatics, $U_{i,\mathrm{elec}}$, and van der Waals (vdW), $U_{i,\mathrm{vdw}}$, contributions as

$$U_i(z)=U_{i,\mathrm{elec}}(z)+U_{i,\mathrm{vdw}}(z). \tag{5.4}$$

Procedures to determine $U_{i,\mathrm{elec}}$ and $U_{i,\mathrm{vdw}}$ are described in Subsections 5.1.1 and 5.1.2.

5.1.1 Electrostatic potential

To include the effects of water orientation polarization and dielectric permittivity variation on the electrostatic potential, we model water molecules as point-like Langevin dipoles (LD) as described by Gongadze et al. [48]. The electrostatic potentials for the ions and water molecules are determined as

$$U_{+/-,\mathrm{elec}}(z) = q_{+/-}\phi(z), \tag{5.5a}$$

$$U_{\mathrm{w,elec}}(z) = \mu \left\langle \cos\theta(z) \right\rangle \phi^{'}(z), \tag{5.5b}$$

where q_+ and q_- are the charges on the cation and anion, respectively, ϕ is the mean electrostatic potential, $\phi^{'}(z) = \frac{d\phi(z)}{dz}$, μ is the dipole moment of the water molecule, θ is the angle between the water dipole vector and the z-axis, and $\langle \cos\theta(z) \rangle$ is the average cosine of the dipole orientation. $\langle \cos\theta(z) \rangle$ can be computed as (see Ref. [48])

$$\langle \cos\theta(z) \rangle = -\mathcal{L}\left(\beta\mu\phi^{'}(z)\right), \tag{5.6}$$

where, $\mathcal{L}(x) = \left(\coth x - \frac{1}{x}\right)$ is the Langevin function and $\beta = \frac{1}{k_{\mathrm{B}}T}$.

From the average dipole orientation profile, we can determine the orientation polarization, $P(z)$, and the dielectric permittivity variation, $\varepsilon_{\mathrm{r}}(z)$, as

$$P(z) = \rho_{\mathrm{w}}(z)\mu \left\langle \cos\theta(z) \right\rangle \tag{5.7}$$

and

$$\varepsilon_{\mathrm{r}}(z) = 1 - \frac{P(z)}{\varepsilon_0 \phi^{'}(z)}, \tag{5.8}$$

where ε_0 is the vacuum dielectric constant. In the limit of $\phi^{'}(z) \to 0$, Eq. 5.8 reduces to the bulk dielectric permittivity,

$$\lim_{\phi^{'}(z)\to 0} \varepsilon_{\mathrm{r}}(z) = \varepsilon_{\mathrm{r,b}} = 1 + \frac{\rho_{\mathrm{w,b}}\mu^2\beta}{3\varepsilon_0}, \tag{5.9}$$

where $\varepsilon_{\mathrm{r,b}}$ is the bulk dielectric permittivity and $\rho_{\mathrm{w,b}}$ is the bulk density of water. We note that the definition of the permittivity given by Eq. 5.8 (the Clausius-Mosotty formula) is valid for the bulk homogeneous and weakly inhomogeneous systems [153]. For strong inhomogeneous systems, a local average density based phenomenological expression for $\varepsilon_{\mathrm{r}}(z)$ is proposed which smoothes out the strong oscillations in the dielectric permittivity profile predicted by Eq. 5.8 [153, 109]. However, MD simulation studies have shown that, near a wall, the dielectric permittivity of water exhibits strong oscillations similar to the density of water [20, 13].

Therefore, in this work, we use Eq. 5.8 which depends on the local density value of water and results in the dielectric permittivity oscillations similar to the oscillations in the density of water (see Sec. 5.4.1 and Fig. 5.6).

To compute $\phi(z)$, we use the 1-D Poisson equation with spatially varying dielectric permittivity as

$$\frac{d}{dz}\left(\varepsilon_{\mathrm{r}}(z)\frac{d\phi}{dz}\right) = -\frac{q_{+}\rho_{+}(z) + q_{-}\rho_{-}(z)}{\varepsilon_0}, \tag{5.10}$$

with boundary conditions

$$\left.\frac{d\phi}{dz}\right|_{z=0} = -\frac{\sigma_{\text{wall-L}}}{\varepsilon_0} \tag{5.11a}$$

$$\left.\frac{d\phi}{dz}\right|_{z=L} = \frac{\sigma_{\text{wall-U}}}{\varepsilon_0} \tag{5.11b}$$

$$\phi\left(z = L/2\right) = 0 \tag{5.11c}$$

In Eqs. 5.10 and 5.11, $\sigma_{\text{wall-L}}$ and $\sigma_{\text{wall-U}}$ are the surface charge densities of the lower ($z = 0$) and upper ($z = L$) walls, respectively. To obtain a non-trivial solution of the Poisson equation with the constant surface charge boundary conditions (Eq. 5.11a and 5.11b), we impose a zero potential condition at the mid-point of the channel via Eq. 5.11c. Therefore, $\phi(z)$ is the relative electrostatic potential with respect to the mid-point of the channel. The condition of $\phi\left(L/2\right) = 0$ is generally exact for sufficiently large channels with significant bulk-like region in the center. However, for smaller channels in which EDLs of opposite walls may overlap, Eq. 5.11c may not be exact. In such cases, to determine a unique solution of Eq. 5.10, it is simpler to use constant surface potential boundary conditions instead of constant surface charge boundary conditions.

5.1.2 vdW potential

We compute the total vdW potential as a sum of the wall-fluid, $U^{\text{wf}}_{i,\text{vdw}}$ and fluid-fluid, $U^{\text{ff}}_{i,\text{vdw}}$, vdW potentials as

$$U_{i,\text{vdw}}(z) = U^{\text{wf}}_{i,\text{vdw}}(z) + U^{\text{ff}}_{i,\text{vdw}}(z). \tag{5.12}$$

In the continuum approximation, we represent the wall as a continuous medium with a uniform particle density, ρ_{wall}. Then, the wall-fluid vdW potential is determined as

$$U^{\text{wf}}_{i,\text{vdw}}(\boldsymbol{r}) = \rho_{\text{wall}} \int u^{\text{wf}}_{i}(r) d\boldsymbol{r}', \tag{5.13}$$

where $u_i^{\mathrm{wf}}(r)$ is the effective vdW pair potential between the wall atoms and molecule i, $\boldsymbol{r}$ and $\boldsymbol{r}'$ are the position vectors, and $r = |\boldsymbol{r} - \boldsymbol{r}'|$. A procedure to compute $U_{i,\mathrm{vdw}}^{\mathrm{wf}}(\boldsymbol{r})$ for a slit-channel system is described in [96]. Note that in Eq. 5.13, $\boldsymbol{r} = x\boldsymbol{i} + y\boldsymbol{j} + z\boldsymbol{k}$ is a general position vector. In the case of a 1-D slit channel, the system is periodic in x and y dimensions and therefore, we consider only the z-variations of the properties, i.e., $U_{i,\mathrm{vdw}}^{\mathrm{wf}}(\boldsymbol{r}) = U_{i,\mathrm{vdw}}^{\mathrm{wf}}(x,y,z) = U_{i,\mathrm{vdw}}^{\mathrm{wf}}(z) \,\forall\, x, y$.

The fluid-fluid vdW potentials are more challenging to compute than the wall-fluid potentials. They give rise to the finite size, i.e., excluded volume effects, dispersion attraction, and particle-particle correlations in the fluid. The exact theoretical framework, which accounts for all the fluid-fluid interaction effects, is unknown. In this work, we split the fluid-fluid vdW potential into purely repulsive and dispersion components as

$$U_{i,\mathrm{vdw}}^{\mathrm{ff}}(\boldsymbol{r}) = U_{i,\mathrm{hs}}^{\mathrm{ff}}(\boldsymbol{r}) + \sum_{j=1}^{3} \int_{R_{ij,\min}^{\mathrm{ff}}}^{R_{ij,\mathrm{cut}}^{\mathrm{ff}}} \rho_j(\boldsymbol{r}') u_{ij}^{\mathrm{ff}}(r) d\boldsymbol{r}', \tag{5.14}$$

where $u_{ij}^{\mathrm{ff}}(r)$ is the effective vdW pair potential between fluid molecules i and j, and $R_{ij,\min}^{\mathrm{ff}}$ and $R_{ij,\mathrm{cut}}^{\mathrm{ff}}$ are the inner and outer cut-offs for the dispersion part of the pair potential, respectively. In Eq. 5.14, $U_{i,\mathrm{hs}}^{\mathrm{ff}}(\boldsymbol{r})$ is the purely repulsive component of the fluid-fluid interactions, which mainly accounts for the excluded volume effects. We use the hard sphere fluid approximation based on the White-Bear version of FMT mark II [124] to determine $U_{i,\mathrm{hs}}^{\mathrm{ff}}(r)$ as

$$U_{i,\mathrm{hs}}^{\mathrm{ff}}(\boldsymbol{r}) = k_{\mathrm{B}}T \sum_{\alpha} \int d\boldsymbol{r}' \frac{\partial \Phi\left(\{n_\alpha\}\right)}{\partial n_\alpha} \frac{\delta n_\alpha\left(\boldsymbol{r}'\right)}{\delta \rho_i\left(\boldsymbol{r}\right)}, \tag{5.15}$$

where Φ is the reduced free energy density and $\{n_\alpha\}$ are the set of weighted densities. The details about Φ and $\{n_\alpha\}$ are given in Appendix A. The second term in Eq. 5.14 accounts for the fluid-fluid vdW attractive interactions using a mean field approximation.

To compute $U_{i,\mathrm{vdw}}^{\mathrm{wf}}$ and $U_{i,\mathrm{vdw}}^{\mathrm{ff}}$, we need to specify $u_i^{\mathrm{wf}}(r)$ and $u_{ij}^{\mathrm{ff}}(r)$. In Eqs. 5.13 and 5.14, $u_i^{\mathrm{wf}}(r)$ and $u_{ij}^{\mathrm{ff}}(r)$ are assumed to be spherically symmetric isotropic pair potentials. Classical atomistic force fields, which are used in MD simulations, provide vdW pair potentials for wall-fluid and fluid-fluid interactions. In the atomistic force fields, vdW interactions of ions are commonly modeled with the pair additive LJ potentials. For monoatomic ions, the ion-ion and ion-wall LJ potentials are spherically symmetric and hence, they are straighforward to use in Eqs. 5.13 and 5.14. However, in MD, the water molecule is generally modeled with multiple sites to represent hydrogen and oxygen atoms and partial charge distribution, e.g. three sites SPC/E model [15], four sites TIP4P model [71], and five sites TIP5P model [91]. Due to multiple sites per water molecule, the water-water and ion-water interactions in an atomistic force field are anisotropic, i.e., they depend not only on the separation distance between molecules but also on the relative orientation.

Therefore, it is more complex to use fully atomistic force field of water in a continuum framework. Hence, we need a simple yet accurate potential model for water which can incorporate the effects of water polarization and ion-water interactions. As explained in Sec. 5.1.1, in EQT, we use a point dipole model for water to include polarization effects of water. However, as per our knowledge, there is no point dipole-based force field for water which can accurately predict the structural and dielectric properties of water. Therefore, we first develop a point dipole-based water force field and single site spherically symmetric ion-water coarse-grained potentials as described in the following section, Sec. 5.2.

5.2 Coarse-grained (CG) potentials

We follow a systematic coarse-graining approach to develop a point dipole based CG model of water and obtain ion-water CG interactions. Systematic coarse-graining is a bottom-up approach to devise CG models by systematically linking a low resolution CG system to a reference high resolution all atom (AA) system [110, 149, 107]. In this work, we first obtain the CG potentials in the particle based CG MD framework and use the same CG interactions in EQT to compute the water-water and ion-water vdW potentials.

5.2.1 Point dipole CG water model

To mimick point dipoles in CG MD, we use an extended dipole topology as shown in Fig. 5.1, in which two opposite charges, $\pm q$, are symmetrically placed at distance $d/2$ from the center of the molecule. Ballenegger and Hansen [12] have shown that for $d/\sigma_{\text{mol}} \leq 0.25$, the extended dipole and point dipole models are similar, where σ_{mol} is the effective diameter of the molecule. For the dipole water model, we fix $d = 0.058\,\text{nm}$, which is same as the length of the SPC/E water dipole and it also satisfies $d/\sigma_{\text{mol}} = 0.183 \leq 0.25$ (with $\sigma_{\text{mol}} = \sigma_{\text{SPCE}} = 0.317\,\text{nm}$). Therefore, the dipole water model has a permanent dipole moment of $\mu = qd$. Total interaction energy between two extended dipoles is a sum of the four electrostatic interactions between the point charges and the vdW interactions,

$$U_{ij,\text{dd}} = u_{\text{dd,cg}}\left(r_{ij}\right) + \sum_{l=1}^{2}\sum_{m=1}^{2} \frac{q_{il}q_{jm}}{4\pi\varepsilon_0\left|\boldsymbol{r}_{il} - \boldsymbol{r}_{jm}\right|}, \tag{5.16}$$

where, $U_{ij,\text{dd}}$ is the total interaction energy between two dipoles i and j, $u_{\text{dd,cg}}\left(r_{ij}\right)$ is the coarse-grained vdW pair potential, r_{ij} is the center-to-center distance between i and j dipoles, q_{il} and q_{jm} are the point charges of dipole molecules i and j, respectively, $q_{i1} = q_{j1} = -q$ and $q_{i2} = q_{j2} = +q$, and $\boldsymbol{r}_{il}$ and $\boldsymbol{r}_{jm}$ are the positions of q_{il} and q_{jm}, respectively. Therefore, the vdW interaction between two dipoles depends only on the distance between the centers of the dipoles and hence, it is spherically symmetric.

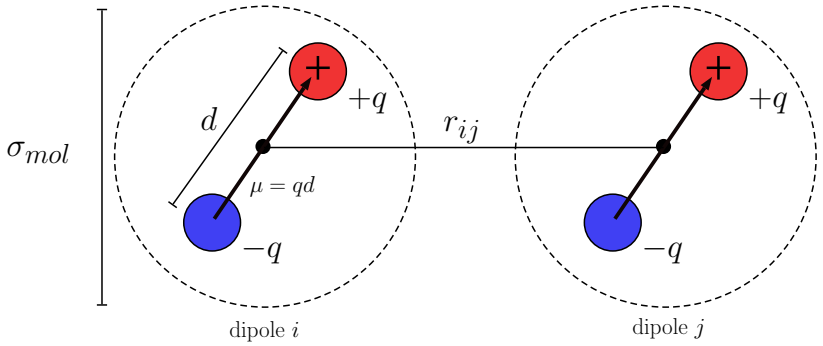

Figure 5.1: Topology of the extended dipole water molecule.

For accurate prediction of EDL properties, we need a dipole model which can accurately capture the structural and dielectric properties of water. We use systematic coarse-graining to determine q and $u_{\mathrm{dd,cg}}(r)$ for the point dipole model such that it reproduces the radial distribution function (RDF) and dielectric permittivity of the bulk water. We use SPC/E as a reference AA model and the RDF of bulk water at 298 K and 1.0 g/cm^3 thermodynamic state as the target RDF and 78.5 as the target permittivity.

There are various structure-based systematic coarse-graining techniques, such as iterative Boltzmann inversion (IBI) [119], inverse Monte-Carlo (IMC) [90], and relative entropy minimization [133, 25], which can optimize $u_{\mathrm{dd,cg}}(r)$ to reproduce a target RDF. We use the relative entropy minimization method to optimize $u_{\mathrm{dd,cg}}(r)$. We model $u_{\mathrm{dd,cg}}(r)$ with a cubic B-splines functional form (see Ref. [98] for the details of the B-splines potential). In [25], it is shown that when CG pair potentials are modeled using finely tabulated functional forms, such as B-splines, the relative entropy minimization based CG potentials reproduce RDFs. Relative entropy based CG water models have been shown to accurately predict the RDF of the bulk water [24, 98] and the density profiles of the confined water [97]. However, the relative entropy minimization does not guarantee reproducibility of the dielectric permittivity. We note that the dielectric permittivity mainly depends on the magnitude of the dipole moment, $\mu = qd$. Since, as mentioned above, we fix $d = 0.058\,\mathrm{nm}$, q is the only free parameter to adjust μ. We use a trial-n-error approach to optimize q such that the target permittivity is reproduced. In this approach, we first set a test value for $q = q^{\mathrm{t}}$ and perform the relative entropy minimization to obtain the vdW pair potential, $u_{\mathrm{dd,cg}}(r) = u^{\mathrm{t}}_{\mathrm{dd,cg}}(r)$ corresponding to q^{t}. Then we perform a CG MD simuation with q^{t} and $u^{\mathrm{t}}_{\mathrm{dd,cg}}(r)$ and compute the RDF and dielectric permittivity. We perform different sets of relative entropy-based coarse-graining calculations with different point charge values. We note that for each point charge value the relative entropy method is able to determine the pair potential which reproduces the target RDF.

Fig. 5.2 shows different pair potentials for different point charge values and comparison of RDFs. We observe that all of them are able to reproduce the target RDF. Dielectric permittivity values obtained for

the different combinations of the point charge and pair potential are given in Table 5.1. We choose the CG potential obtained with $q = 0.73$ e, which reproduces both the target RDF and dielectric permittivity.

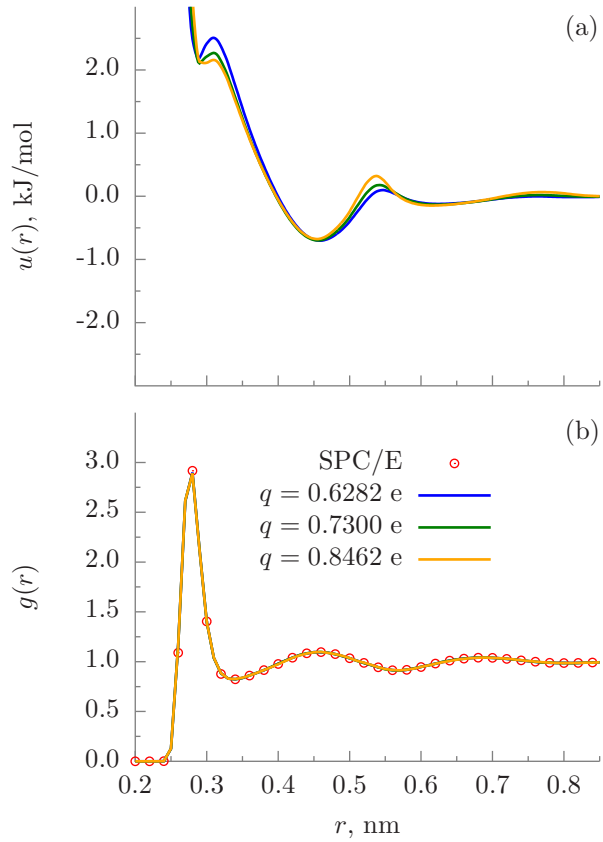

Figure 5.2: (a) Dipole-dipole CG potentials obtained by the relative entropy minimization for different point charge values. (b) Comparison of COM RDFs from SPC/E based AA MD and point dipole based CG MD.

Table 5.1: Dielectric permittivities of point dipole water for different point charge values.

q (e)	μ (D)	ε_{r}
0.8476	2.35	292.78
0.7300	2.034	77.01
0.6282	1.75	49.75

5.2.2 Ion-water CG potentials

An ion-water interaction has two parts: (i) the long-range ion-water electrostatic interaction and (ii) the short-range ion-water vdW interaction. The ion-water electrostatic interaction causes screening of the ion-ion electrostatic interactions. The effects of the ion-water electrostatic interactions can be accounted via the dielectric premittivity of water, which scales down (i.e., screens) the ion-ion electrostatic interactions.

Therefore, here, we only determine the ion-water short-range vdW interactions by the systematic coarse-graining approach.

For systematic coarse-graining of the ion-water vdW interactions, we use a single Na^+-Cl^- pair dissolved in a bulk water system. In the reference atomistic simulations, water is modeled with SPC/E force field, ion-ion, and ion-water interactions are modeled with the force field of Joung and Cheatham [73] (see Sec. 5.3.2). To determine the ion-water CG interactions, we represent water as a single bead and for water-water interactions, we use the relative entropy based CG interactions obtained in Ref. [98]. The ion-ion vdW interactions are the same as the LJ interactions in the atomistic force-field. The charges on the ions are also kept the same as in the atomistic force field. The ion-ion electrostatics are computed by the particle mesh Ewald (PME) [29] method with the relative permittivity of 78.5. The ion-water CG potentials are modeled with B-splines and optimized by the relative entropy minimization.

Fig. 5.3 shows the Na^+-water and Cl^--water CG potentials and the comparison of the ion-water RDFs from the AA MD and CG MD simulations. We observe that the ion-water CG potentials accurately predict the ion-water RDFs. Though the ion-water CG potentials are obtained from the single ion pair system, i.e., dilute ion concentration, we find that the ion-water CG potentials are transferable upto 1 M ion concentration, i.e., they can reproduce ion-water RDFs of the bulk NaCl system upto 1 M concentration.

In this work, the relative entropy-based coarse-graining for the point dipole CG water and ion-water CG interactions are performed using the versatile object-oriented toolkit for coarse-graining applications (VOTCA) [126, 98]. We follow the procedure as described in Ref. [98] for the relative entropy minimization. The reference AA MD and CG MD simulations are performed in GROMACS [113]. The long-range electrostatic interactions are computed with the PME. A cut-off of 0.9 nm is used for the vdW pair potential and the short-range component of the electrostatic interactions.

5.3 Simulation details

To demonstrate EQT for EDL, we simulate NaCl aqueous electrolyte confined inside slit-like capacitor channels. The electrolyte fluid is confined between two parallel, uniformly, and oppositely charged graphene walls separated by 3.804 nm ($=12\sigma_{\mathrm{OW}}$, where $\sigma_{\mathrm{ow}}(=0.317$ nm) is the length scale of the LJ interactions between water oxygen atoms). $12\sigma_{\mathrm{ow}}$ is a large enough width to avoid overlap of two opposite EDLs and allow sufficiently wide bulk-like region at the center of the channel. The confined electrolyte is assumed to be in thermodynamic equilibrium with a reference bulk electrolyte system. We consider a range of $0.25-1$ M bulk ion concentrations in water at 1.0 g/cm^3 density and 298 K temperature, and surface charge densities

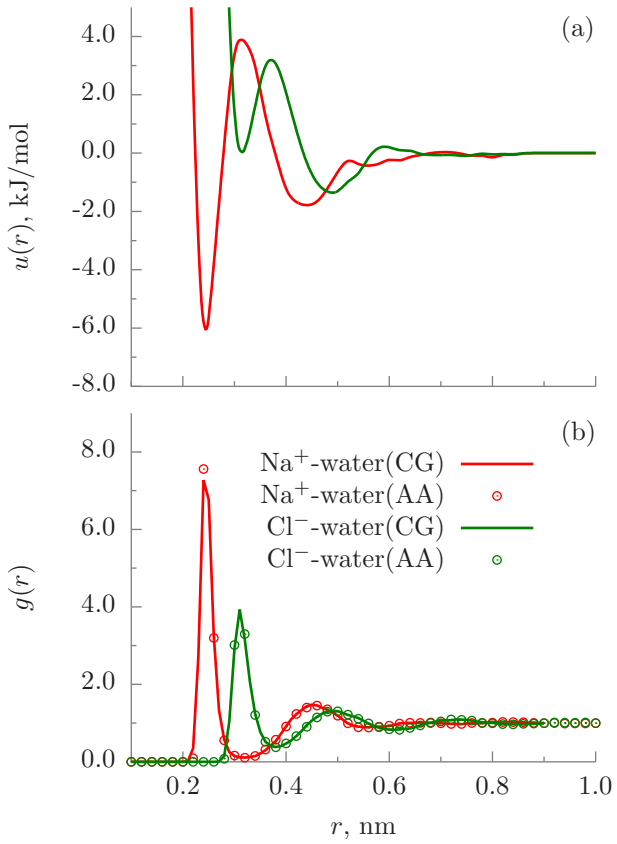

Figure 5.3: (a) Ion-water CG potentials obtained by relative entropy minimization. (b) Comparison of ion-water RDFs from AA MD and CG MD.

of $0.12 - 0.18$ C/m^2. Table 5.2 summarizes four different systems considered in this work. To check the accuracy of EQT, we compare the EQT results with MD simulations.

Table 5.2: Summary of the systems simulated.

System no.	Lower/upper wall charge density (C/m^2)	NaCl concentration (M)	Molecules in MD simulations water/Na^+/Cl^-
I	-0.12/0.12	0.25	1624/14/14
II	-0.15/0.15	0.50	1637/22/22
III	-0.15/0.15	0.75	1633/28/28
IV	-0.18/0.18	1.00	1640/37/37

5.3.1 EQT simulations

In EQT, we solve Eqs. (5.3)-(5.14) self-consistently to determine density and potential profiles of ions and water. The reference densities and potentials required in Eq. 5.3 are determined from the reference bulk system. The reference bulk potentials, $U_{i,\text{ref}}$, are computed by substituting the bulk densities in Eq. 5.14. To compute the attractive part of the vdW potential from Eq. 5.14, we use the CG pair potentials, i.e.,

$$u_{ij}^{\text{ff}}(r) = u_{ij,\text{cg}}^{\text{ff}}(r), \tag{5.17}$$

where, $u_{ij,\text{cg}}^{\text{ff}}$ is the CG interaction between the molecules i and j. As explained in Sec. 5.1.2, for the ion-ion pairs, $u_{ij,\text{cg}}^{\text{ff}}$ are the same LJ potentials as in the reference MD simulations (see Sec. 5.3.2) and for the water-water and ion-water pairs, we use the CG pair potentials obtained in Sec. 5.2. For all the pair potentials, we set $R_{ij,\text{cut}}^{\text{ff}} = 0.9$ nm. There are different approaches to set $R_{ij,\text{min}}^{\text{ff}}$ for the LJ type pair potentials [154]. Here, we set $R_{ij,\text{min}}^{\text{ff}} = \sigma_{ij}^{\text{ff}}$ for the ion-ion LJ pair potentials, where σ_{ij}^{ff} is the usual LJ parameter. For the water-water and ion-water CG potentials, we set $R_{ij,\text{min}}^{\text{ff}}$ to be the location of the first minima of the corresponding CG pair potential. Therefore, $R_{\text{ww,min}}^{\text{ff}} = 0.28\,\text{nm}$, $R_{\text{+w,min}}^{\text{ff}} = 0.244\,\text{nm}$, and $R_{\text{-w,min}}^{\text{ff}} = 0.314\,\text{nm}$. To compute the wall-fluid potential energies from Eq. 5.13, we use $\rho_{\text{wall}} = 38.18\,\text{atoms/nm}^3$ for the graphene walls. For the wall-water potential energy, we use the same LJ pair potential as that of C-O pair in the reference MD simulations. For the wall-ion potentials, as explained in Sec. 5.4.2, we modify the reference MD C-ion LJ pair potentials to account for the errors in the Langevin dipole model near the walls. To determine the mean electrostatic potential, $\phi(z)$, we solve Eqs. 5.10 and 5.11 with $q_+ = +1.0\,\text{e}$ and $q_- = -1.0\,\text{e}$ and $\mu = 2.88\,\text{D}$. For the capacitor channel, the walls are equally and oppositely charged such that $\sigma_{\text{wall-L}} = -\sigma_{\text{wall}}$ and $\sigma_{\text{wall-U}} = \sigma_{\text{wall}}$, where σ_{wall} is the given surface charge density. To determine the hard-sphere energy component from FMT (Eq. 5.15), we use $d_{\text{hs,w}} = 0.28\,\text{nm}$, $d_{\text{hs,+}} = 0.14\,\text{nm}$, and $d_{\text{hs,-}} = 0.23\,\text{nm}$. The

values for μ and $d_{\mathrm{hs},i}$ are set such that the density profiles from EQT compare well with the reference MD simulations. The summary of the interaction parameters used in EQT simulations is given in Table 5.3.

Table 5.3: Interaction parameters in EQT simulations.

	q (e)	μ (D)	d_{hs} (nm)
Water	0.0	2.88	0.28
Na^+	+1.0	0.0	0.14
Cl^-	-1.0	0.0	0.23
	$u_{\mathrm{cg}}^{\mathrm{ff}}(r)$	$R_{\mathrm{min}}^{\mathrm{ff}}$ (nm)	
Water – Water	$u_{\mathrm{dd,cg}}(r)$[1]	0.28	
Na^+ – Na^+	$u_{\mathrm{Na\text{-}Na,md}}(r)$[2]	0.21595	
Cl^- – Cl^-	$u_{\mathrm{Cl\text{-}Cl,md}}(r)$2	0.48304	
Na^+ – Cl^-	$u_{\mathrm{Na\text{-}Cl,md}}(r)$2	0.349495	
Na^+ – Water	$u_{\mathrm{Na\text{-}Water,cg}}(r)$[3]	0.244	
Cl^- – Water	$u_{\mathrm{Cl\text{-}Water,cg}}(r)$3	0.314	
C – Water	$u_{\mathrm{C\text{-}O,md}}(r)$2	0.0	
C – Na^+	LJ ($\sigma = 0.4596$ nm, $\epsilon = 0.2328$ kJ/mol)	0.0	
C – Cl^-	LJ ($\sigma = 0.3814$ nm, $\epsilon = 0.1781$ kJ/mol)	0.0	

Once all the parameters are set, we use Picard iteration technique to self-cosistently solve Eqs. (5.3)-(5.14). We note that the convergence of the Picard iterations depends on the initial guesses for the fluid density profiles. We use uniform bulk fluid densities as an initial guess. However, for high surface charge densities, the Picard iterations may diverge depending on the initial guess. Similar convergence issues for high ion concentrations and surface charge densities have been observed by others [60, 153]. To solve the convergence issue, we implement a surface charge stepping procedure as following. We start with a zero surface charge boundary condition and uniform bulk densities as an initial guess and obtain the converged fluid densities, $\rho_i^0(z)$, corresponding to the zero surface charge. Next, we increment the surface charge by a discrete value $\Delta\sigma_{\mathrm{wall}}$ and use $\rho_i^0(z)$ as an initial guess to again obtain the converged densities, $\rho_i^{\Delta\sigma_{\mathrm{wall}}}(z)$. We repeat this procedure of increasing the surface charge by $\Delta\sigma_{\mathrm{wall}}$ and using $\rho_i^{(n-1)\Delta\sigma_{\mathrm{wall}}}(z)$ as an initial guess to obtain the density profiles for the surface charge of $n\Delta\sigma_{\mathrm{wall}}$ until we reach the target surface charge value, σ_{wall}.

We note that the EQT simulations are orders of magnitude faster than the MD simulations. For example, on a single Intel Core i7-3520M 4M Cache 3.60 GHz processor, an EQT simulation of system III requires around 4 min, whereas a 10 ns long MD simulation of the same system requires around 60 h.

[1] Same as the dipole-dipole CG potential obtained in Sec. 5.2.1
[2] Same as the LJ potentials in MD (Table 5.4)
[3] Same as the ion-water CG potentials obtained in Sec. 5.2.2

Table 5.4: LJ interaction parameters in MD simulations.

	σ (nm)[4]	ϵ (kJ/mol)4
H	0.0	0.0
O	0.317	0.6503
Na^+	0.21595	1.47545
Cl^-	0.48304	0.05349
C	0.339	0.2334

5.3.2 MD simulations

The reference MD simulations are performed in the NVT (canonical) ensemble by GROMACS. Two graphene walls are placed along the xy plane, and the lateral dimensions of the walls are $3.834 \times 3.68927\,\text{nm}^2$. The wall atoms are kept fixed. A uniform partial charge is assigned to the wall atoms. The value of the partial charge on the wall atoms is determined from a given surface charge density. For example, -0.02 e and $+0.02$ e charges are assigned to the lower ($z = 0$) and upper ($z = L$) wall atoms, respectively, to achieve the surface charge density of 0.12 C/m^2. Periodic boundary conditions are used in the x, y, and z directions. Water is modeled using SPC/E force field and ions are modeled using the force field of Joung and Cheatham [73]. The LJ interaction parameters of various fluid particles are given in Table 5.4. The LJ parameters between two dissimilar particles are determined by the Lorentz-Berthlot (LB) combination rule. We note that Wu and Aluru [159] have developed a more accurate graphitic carbon-water force field. This carbon-water force field depends on the water orientation and hence, it is anisotropic. As explained in Sec. 5.1.2, for simplicity, we use isotropic vdW pair potentials in EQT, and therefore, in MD also, we model C-water interactions by the LJ type isotropic pair potential parameters given in Table 5.4. Spherical cutoff of 0.9 nm is used for the LJ interactions, and electrostatic interactions are computed by PME [29]. The simulation box is padded with a vacuum layer of $50\sigma_{\text{ow}}$ in the z dimension along with a correction for the slab geometry to exclude the interactions between the periodic images in z. Temperature is maintained using the Nosé-Hoover thermostat [108] with 0.5 ps time constant. Equations of motion are integrated with the leap-frog algorithm with a time step of 1 fs. For a given bulk ion concentration and surface charge density, the number of ions and water molecules are determined by a trial-n-error approach such that the bulk fluid densities are achieved in the center of the channel. The number of molecules determined for different systems are given in Table 5.2. For each ion concentration and surface charge density, equilibrium properties are obtained by averaging the values from 5 different MD simulations of 10 ns each with different initial conditions.

[4]Parameters for the two dissimilar particles are determined by the Lorentz-Berthlot (LB) combination rule.

5.4 Results and discussion

5.4.1 Analysis of LD approach

First, we analyze the ability of the LD model to predict electrostatic potential variations in EDL. For this analysis, we provide the ion and water center of mass (COM) density profiles from the MD simulations of system II as an input to the LD Eqs. (5.6)-(5.11) and solve the equations self-consistently. To study the dependence of LD results on the dipole moment, we vary μ from 1.2-4.8 D. For comparison, we also compute $\phi(z)$ with a uniform dielectric permittivity of $\epsilon_r = 78.5$. We compare $\phi(z)$ from the LD and uniform permittivity approaches with MD. To compute $\phi(z)$ from MD, we solve Eq. 5.10 with $\epsilon_r = 1$ and the charge densities of ions and partial charges of water molecules, i.e., $\sum_i q_i\rho_i(z) = q_{Na^+}\rho_{Na^+}(z) + q_{Cl^-}\rho_{Cl^-}(z) + q_H\rho_H(z) + q_O\rho_O(z)$. Fig. 5.4 shows the total charge density and densities of Na^+, Cl^-, O, H, and water COM from MD.

Fig. 5.5 shows the comparison of the electrostatic potentials from MD, LD, and uniform permittivity approaches. We observe that $\phi(z)$ from MD shows pronounced oscillations near the channel walls and it varies linearly in the central region of the channel. In the lower half of the channel, i.e., closer to the negatively charged wall, $\phi(z)$ is mostly negative except at 0.2 nm away from the lower wall, where there is a positive peak in $\phi(z)$. The positive peak in the electrostatic potential near the negatively charged wall can be attributed to the net positive charge density due to accumulation of positively charged hydrogen atoms at 0.2 nm away from the lower wall (see Fig. 5.4). Similarly, in the upper half of the channel, $\phi(z)$ is mostly positive except at 0.3 nm away from the upper wall, where there is a negative valley due to the net negative charge density from the accumulation of negatively charged Cl^- and oxygen atoms.

The electrostatic potential profiles from the LD approach show weaker oscillations compared to MD. Moreover, the strength of the electrostatic potential from the LD model decreases as the dipole moment value is increased. This behavior can be understood by examining the dielectric permittivity profiles from the LD model for different μ values as shown in Fig. 5.6. We observe that, for all μ values, the variations in ε_r are similar to the variations in the water COM density profile. However, a larger dipole moment value results in a higher permittivity profile which results in a stronger screening of the surface electric field and hence, a smaller potential profile. The errors in the LD model are due to the simplifications adopted in Eqs. (5.6)-(5.10). The LD model is a mean-field approach and hence, it ignores dipole-dipole direct interactions and dipole-dipole correlations [48]. In addition, the LD model neglects higher electric moments of the water molecule, such as a quadrupole moment, which also contribute to the dielectric permittivity variation of confined water [20, 21].

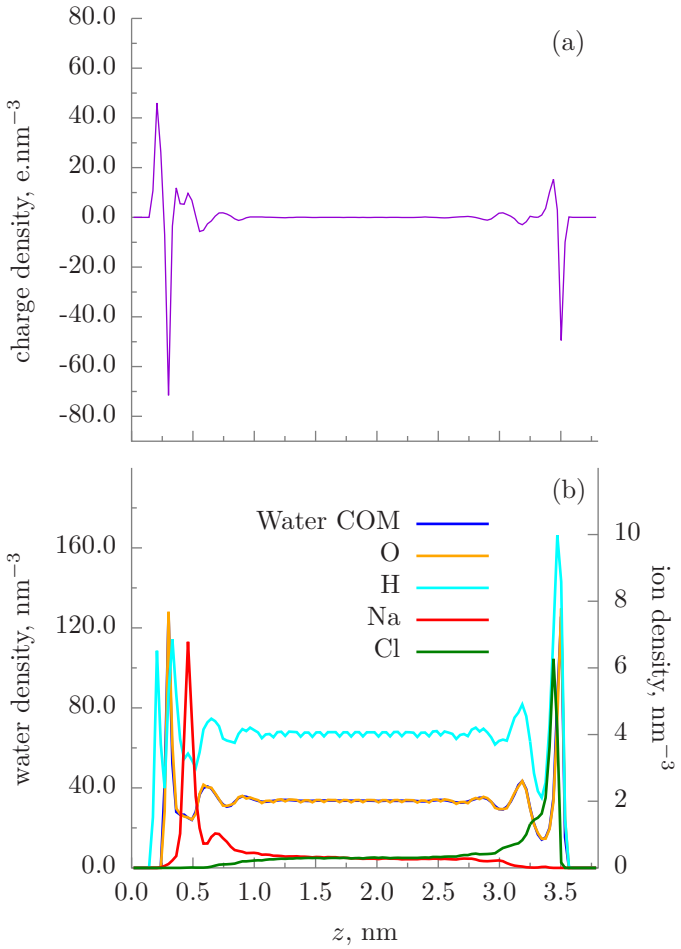

Figure 5.4: Charge and species density profiles from the MD simulations of system II: (a) Total charge density, i.e., ions plus water partial charges. (b) O, H, and water COM densities on the left y-axis and Na^+ and Cl^- ion densities on the right y-axis.

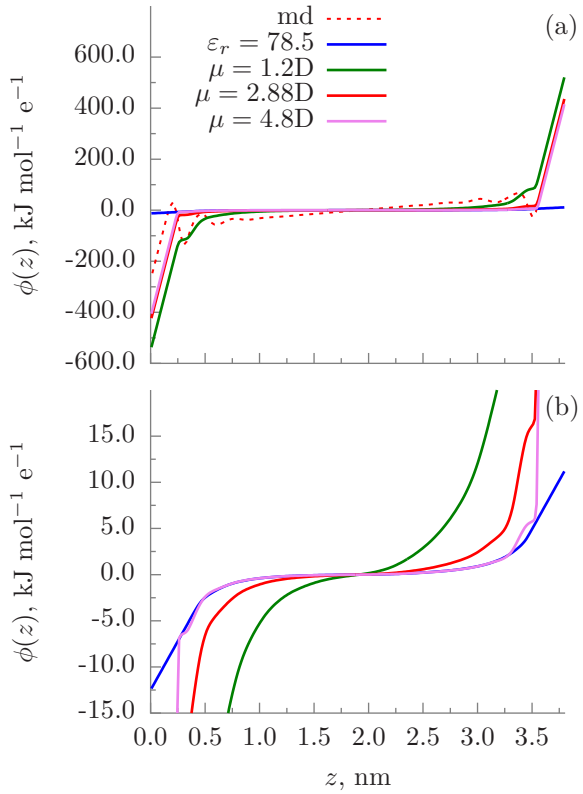

Figure 5.5: Electrostatic potentials for system II from MD, LD with different dipole moment values, and uniform permittivity approximation with $\varepsilon_r = 78.5$. (a) Full range plots for comparison with MD. (b) Zoomed in plot for comparing LD and uniform permittivity approaches.

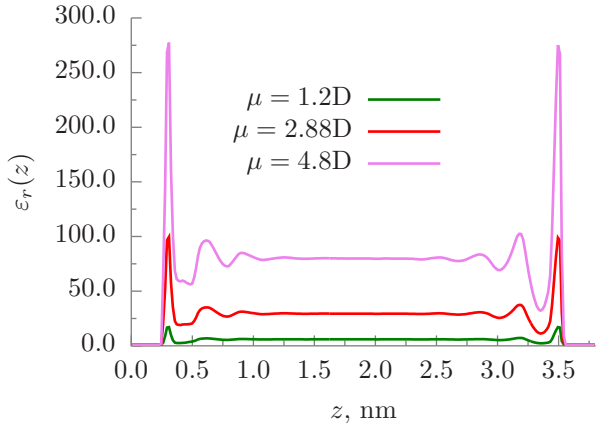

Figure 5.6: Dielectric permittivity profiles of system II from LD with different dipole moment values.

Though the LD model fails to capture the oscillations in $\phi(z)$, the surface potentials at the walls (i.e., $\phi(0)$ and $\phi(L)$) predicted by LD are comparable to MD. We observe that, for all μ values considered, the error in the surface potential at the negatively charged wall is higher compared to the error at the positively charged wall. This is mainly due to the failure of the LD framework to capture the positive peak in the electrostatic potential near the negatively charged wall. Despite these errors, the LD framework performs better than the uniform dielectric approach. From Fig. 5.5, we observe that $\phi(z)$ from the uniform dielectric permittivity approach does not exhibit any oscillations and it increases monotonically from the lower to the upper wall. Moreover, there is an order of magnitude error in the surface potentials predicted by the uniform permittivity approach. Therefore, the LD approach is an improvement over the uniform permittivity approach.

5.4.2 EQT results

We use the EQT framework to obtain ion and water density profiles for the four systems summarized in Table 5.2. The numerical details of the EQT simulations are given in Sec. 5.3.1. As explained in Sec. 5.3.1, for the ion-ion interactions, we use the same LJ potentials that are used in the reference MD simulations. For the water-water and ion-water pair interactions, we use the systematically developed CG potentials discussed in Sec. 5.2. For the wall-water interactions, we use the same C-O LJ potential used in the reference MD simulations. For the wall-ion interactions, we use LJ pair potentials similar to those in the reference MD. However, we modify the wall-ion LJ interaction parameters to account for the errors in the electrostatic potential near the walls due to the approximations in the LD model as described in Sec. 5.4.1. To optimize the wall-ion LJ potentials, we use a potential of mean force (PMF) matching based technique [97]. For the PMF-matching we use system IV as a reference system. The optimized wall-ion LJ parameters are: $\sigma_+^{\text{wf}} = 0.4596\,\text{nm}$, $\epsilon_+^{\text{wf}} = 0.2328\,\text{kJ/mol}$, $\sigma_-^{\text{wf}} = 0.3814\,\text{nm}$, and $\epsilon_-^{\text{wf}} = 0.1781\,\text{kJ/mol}$. For the water point dipole, we use $\mu = 2.88\,\text{D}$ because it predicts the surface electrostatic potentials comparable to MD (see Sec. 5.4.1). The summary of the interaction parameters used in EQT simulations is given in Table 5.3.

Figs. 5.7 and 5.8 show the comparison of the density profiles from EQT and MD for water and ions, respectively. For comparison purposes, we also include the density profiles from 3CM cDFT simulations. In the 3CM cDFT simulations, water molecules are modeled as neutral LJ type particles and ions are modeled as charged particles with LJ interactions. The LJ interaction parameters are the same as in MD and the electrostatic interactions are computed by the Poisson's equation with a uniform dielectric permittivity of 78.5. The hard sphere component of the free energy is modeled with FMT with the same hard sphere diameters as in EQT.

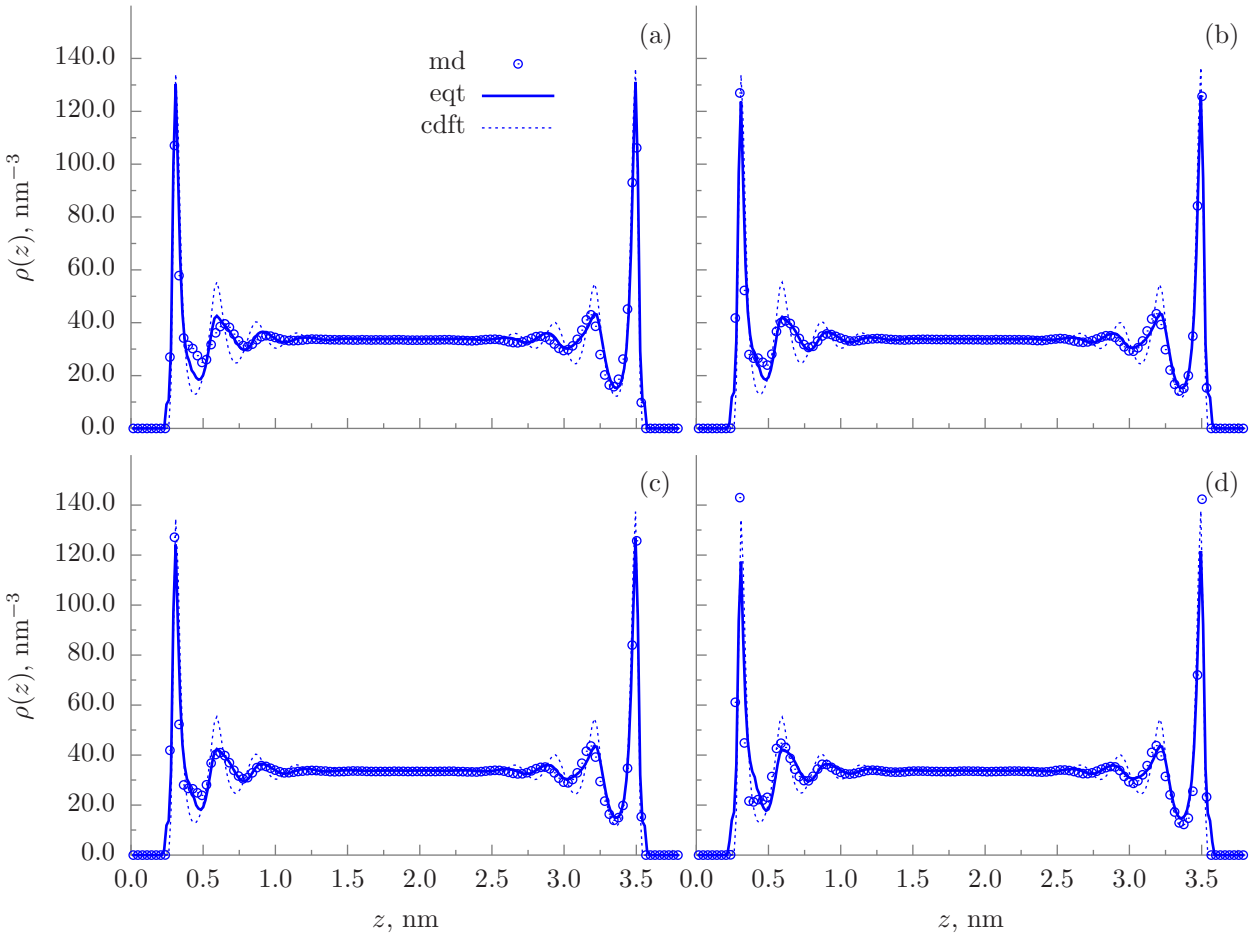

Figure 5.7: Comparison of water density profiles from EQT, 3CM cDFT, and MD for four different systems: (a) system I, (b) system II, (c) system III, and (d) system IV.

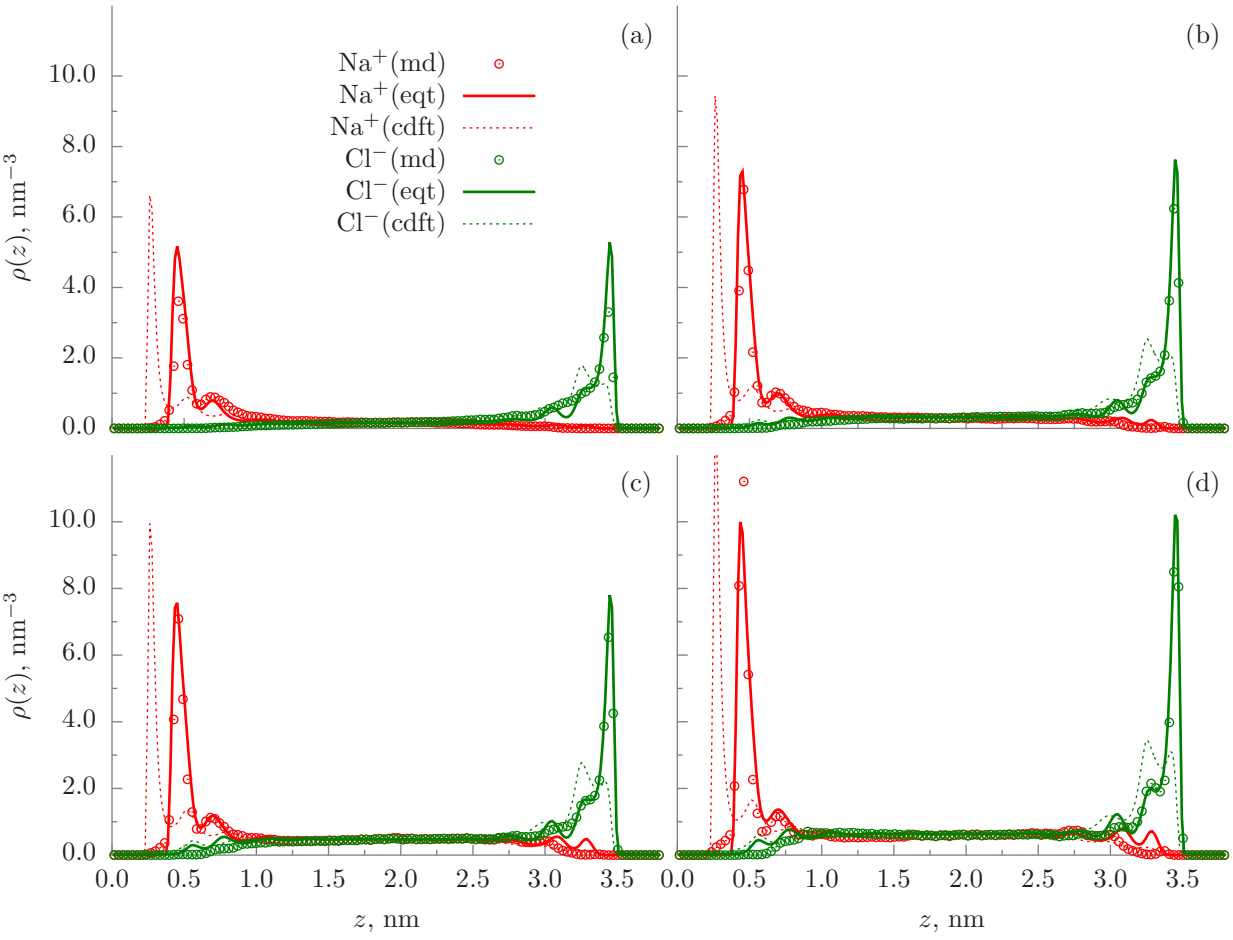

Figure 5.8: Comparison of Na^+ and Cl^- ion density profiles from EQT, 3CM cDFT, and MD for four different systems: (a) system I, (b) system II, (c) system III, and (d) system IV.

Fig. 5.7 shows that the water density profiles from EQT compare well with the reference MD simulations. The 3CM cDFT predicts higher oscillations in the water density profiles compared to MD. The errors in the 3CM cDFT water density profiles are due to the simple LJ based model of water, which ignores the water-water electrostatic interactions. Fig 5.8 shows that the ion density profiles from EQT compare well with the reference MD simulations. The distribution of Na^+ and Cl^- ions near the charged surfaces, such as the location of the first peak and layering, is different due to the differences in their sizes and hydration properties [115, 116, 39]. Such ion specific information is built into the EQT framework via different hard sphere diameters and ion-water CG potentials, which accounts for the ion hydration. The ion density profiles from 3CM cDFT are qualitatively and quantitatively different than the MD simulations. The errors in the 3CM cDFT mainly arise from the inability of the simple LJ based ion-water potentials and uniform dielectric permittivity assumption to capture ion hydration and water polarization effects.

There are, however, some quantitative discrepancies between the EQT and MD density profiles. These discrepancies are due to the simplifications made in this work. In addition to the mean-field approximations in the LD approach, as described in Sec. 5.4.1, we ignore fluid-fluid correlations while determining the vdW potentials from Eq. 5.14. Also, for the water-water and ion-water interactions, we use the CG potentials determined from the bulk systems. Since, the interfacial arrangement of the water molecules and ions is different from the bulk, the bulk-based CG potentials are not exact near the surface. There are approaches in EQT to address these limitations. The fluid-fluid correlation effects can be accounted via the correlation correction potential approach as described in [99, 102]. To account for the errors arising from the bulk-based CG potentials near the interface, wall-fluid interactions can be modified as suggested in [96, 97]. We note that, in this work, we already optimize the wall-ion LJ interactions to account for the errors near the interface. The accuracy of these wall-ion CG potentials can further be improved by using a more flexible B-splines functional form. Similarly, the errors in the water density profiles can be corrected by using a more complex functional form, such as LJ plus 2 Gaussians or B-splines, to model wall-water vdW potential [96, 97].

5.5 Summary

In this chapter, we presented an empirical potential-based quasi-continuum theory (EQT) for EDL, which incorporates the polarization and hydration effects of water explicitly. Water molecules are modeled as Langevin point dipoles and a point dipole based coarse-grained model for water is developed systematically. The space dependence of the dielectric permittivity of water is included in the Poisson equation to compute the electrostatic potential. In addition, to reproduce hydration of ions, ion-water coarse-grained potentials

are developed. We demonstrated the Langevin-Poisson-EQT framework for EDL by simulating NaCl aqueous electrolyte confined inside slit-like capacitor channels at various ion concentrations and surface charge densities. We showed that the ion and water density predictions from EQT agree well with the reference molecular dynamics simulations. Further improvements can be made to the Langevin-Poisson-EQT framework by incorporating dipole-dipole, ion-ion, and ion-dipole electrostatic correlations, which we discuss in Chapter 6.

Chapter 6

EQT to predict charge inversion in electric double layers

6.1 Charge inversion

The charge inversion is a phenomenon in which the co-ion charge density exceeds the counterion charge density in a certain region of the EDL. The presence of counterions next to a charged surface reduces the apparent surface charge of the EDL compared with the bare surface charge. The apparent surface charge is the charge that ions away from the surface see. The charge inversion occurs when the apparent surface charge has an opposite sign than that of the bare surface charge. The reversal of apparent surface charge is possible when the number of counterions next to the surface exceeds the surface charge. In an EDL region that experiences the reversal of apparent charge, coions are attracted and counterions are repelled, which causes the charge inversion.

In this chapter, we focus on extending the LP-EQT framework to accurately predict charge inversion phenomenon in EDLs. For a reference charge inversion system, we consider a KCl aqueous electrolyte confined inside a slit-like graphene channel. The electrolyte fluid is confined between two parallel, uniformly, and negatively charged graphene walls with -0.2265 C/m^2 surface charge density and 3.804 nm channel width. The confined electrolyte is assumed to be in thermodynamic equilibrium with a reference bulk electrolyte system with 1.0 M bulk ion concentrations in water at 1.0 g/cm^3 density and 298 K temperature. In the reference AA-MD simulations, water is modeled using SPC/E force field and ions are modeled using the force field of Joung and Cheatham [73]. The procedure of AA-MD simulations is same as described in Sec. 5.3.2. The number of fluid molecules used in the AA-MD simulations are: 1640 water molecules, 77 K^+ ions, and 37 Cl^- ions.

Fig. 6.1 shows the density profiles of K^+, Cl^-, and water COM obtained from the AA-MD simulations. Since the surface charge is negative, in this case, K^+ ions are counterions and Cl^- are coions. As expected water molecules arrange in distinct layers near the channel walls. We observe that majority of K^+ ions accumulate within 0.4 nm distance from the walls, Cl^- ion density is very low within 0.4 nm distance from the walls, and between 0.6 - 1.4 nm distance from the walls Cl^- (coion), density is higher than K^+

(counterion). Therefore, the charge inversion occurs at 0.6 nm distance away from the walls.

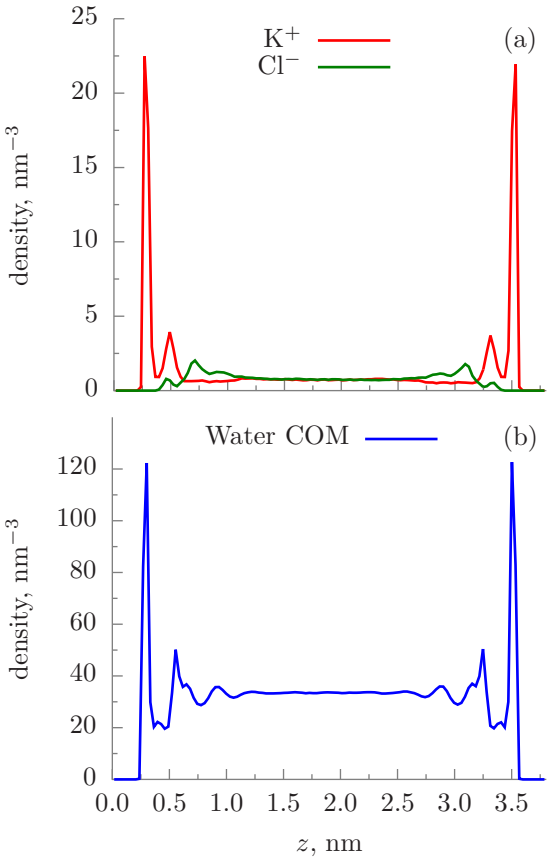

Figure 6.1: Ion (a) and water COM (b) density profiles from the reference AA-MD simulations of the charge inversion phenomenon in KCl aqueous electrolyte confined inside a slit-like graphene channel.

6.2 LP-EQT limitations

First, we test the ability of the LP-EQT framework, which is described in Section 5, to predict the charge inversion phenomenon in the confined KCl electrolyte system. In the LP-EQT simulation, for the water-water and Cl^--water interactions, we use the same CG potentials obtained in Section 5.2. For the K^+-water interaction, we obtain the CG potential following the same coarse-graining procedure as described in Section 5.2.2. Fig. 6.2 shows the K^+-water CG potential which reproduces the K^+-water RDF in the bulk. The ion-ion interactions are the same LJ potentials as in the reference MD simulations. Also, for wall-water, wall-K^+, and wall-Cl^- interactions, we use the same LJ interactions as in the reference MD simulations. For K^+, we set $d_{\mathrm{hs},+} = 0.18\,\mathrm{nm}$. The remaining parameters related to water and Cl^- are the same as in Section 5.3.1.

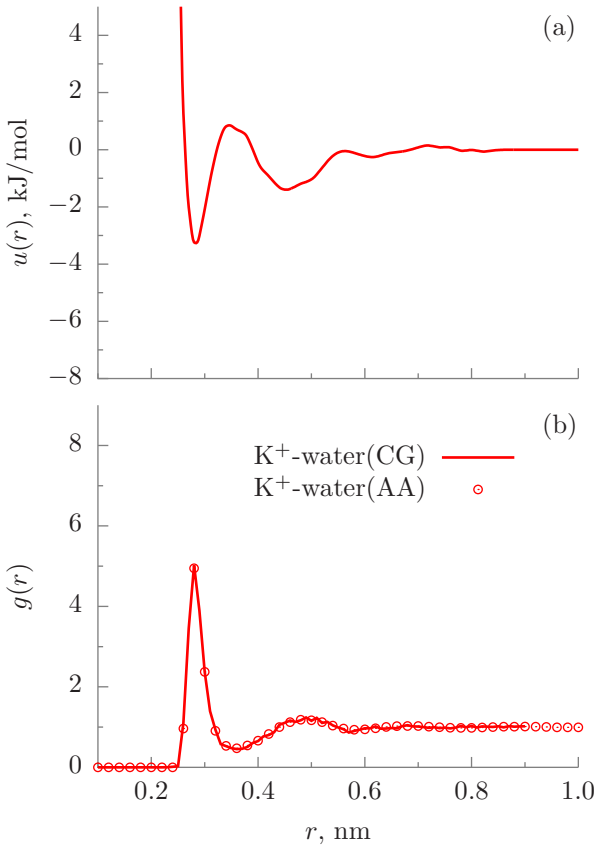

Figure 6.2: (a) K^+-water CG potential obtained by relative entropy minimization. (b) Comparison of K^+-water RDFs from AA MD and CG MD.

Fig. 6.3 shows the comparisons of the water and ion density profiles for the confined KCl electrolyte system from the LP-EQT and AA MD simulations. We observe that the water density profile from the LP-EQT compares well with reference MD simulations. However, LP-EQT framework fails to accurately predict ion density profiles and the charge inversion phenomenon near the walls. The errors in the LP-EQT results can be attributed to the simplifications and approximations made in the LP-EQT framework as described in Section 5.4.2. The Langevin-Poisson approach to compute the electrostatic interactions is a mean-field approach and hence, it ignores ion-ion, ion-dipole, and dipole-dipole correlations. Furthermore, as we discussed in Section 4.3, bulk-based CG potentials fail to predict interfacial layering of fluid molecules in a confined fluid system.

The focus of this chapter is to address the approximations in the LP-EQT framework and improve the accuracy of the LP-EQT such that it can accurately predict the charge inversion phenomenon. In Section 6.3, first, we develop accurate CG potentials for the confined KCl system by systematic coarse-graining approach. Then, in Section 6.4, we describe an approach to incorporate short-range ion-ion, ion-dipole, and dipole-

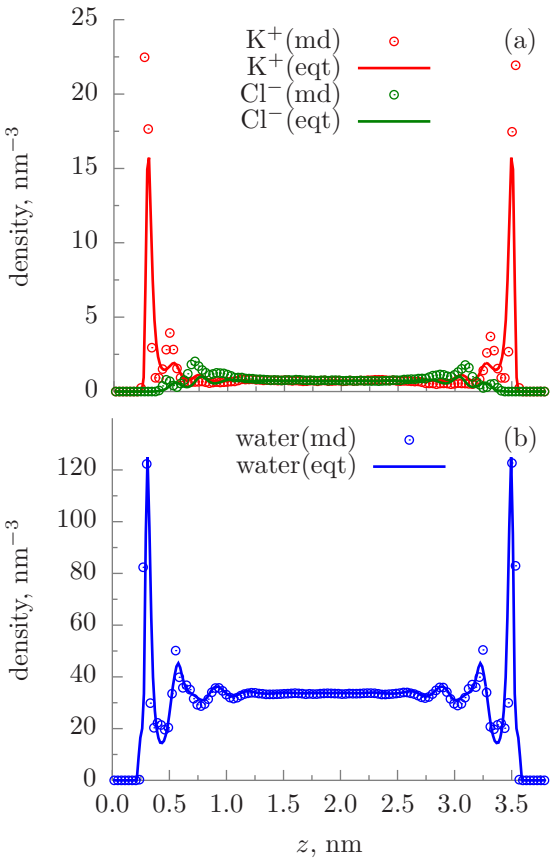

Figure 6.3: Comparisons of ion density profiles (a) and water COM density profile (b) from AA MD and LP-EQT for the charge inversion phenomenon in the confined KCl electrolyte system.

dipole electrostatic correlations in the LP-EQT framework. In Section 6.5, we present the results of EQT for the charge inversion system.

6.3 Systematic coarse-graining

For the confined KCl electrolyte system, we explore two coarse-grained representations for water molecule: (i) single coarse-grained bead at the center of mass (COM) with zero charge and no dipole moment; denoted as (oW) CG water model and (ii) point dipole model; denoted as (μW) CG water model. oW CG water is a single site isotropic model that is easy to incorporate accurately in a continuum-based approach like EQT. However, *oW* CG model cannot explicitly model water polarization effects and screening of electrostatic interactions in ionic systems. On the other hand, μW CG water can model the effects of water polarization and permittivity variation in EDL. However, due to orientation dependence and anisotropic nature of dipole-dipole and ion-dipole electrostatic interactions, μW CG water is challenging to model accurately in a

continuum-based approach.

We follow the similar systematic coarse-graining procedure described in Section 4.3 to obtain the water-water, wall-water, ion-water, and wall-ion CG potentials. The ion-ion vdW interactions are the same as the LJ interactions in the atomistic force-field. The charges on the ions are also kept the same as in the atomistic force field.

*o*W CG water

In *o*W water based CG representation of the KCl electrolyte system, we assume a uniform permittivity of 78.5 to incorporate screening effects of water. For the water-water interaction, we use the water-water CG potential obtained from bulk water in Appendix B. K^+-water and Cl^--water CG potentials are determined from the bulk KCl electrolyte system by relative entropy minimization. Wall-water and wall-ion interactions are optimized by relative entropy based coarse-graining of the confined KCl electrolyte system. Fig. 6.4 shows the water-water, ion-water, wall-water, and wall-ion CG potentials. From Fig. 6.5, we observe that the CG potentials can accurately predict the water and ion density profiles by CG MD simulations. This suggests that, though *oW* CG water representation assumes a uniform permittivity, the effects of water polarization and permittivity variations in the double layer region near the charged surface are accurately incorporated in the wall-water and wall-ion CG potentials.

μW CG water

In μW water based CG representation, we use the same water-water CG potential obtained in Section 5.2.1 with $\mu = 2.88\,\mathrm{D}$ which reproduces both the RDF and permittivity of bulk water. K^+-water and Cl^--water CG potentials are determined from the bulk KCl electrolyte system by relative entropy minimization. Wall-water and wall-ion interactions are optimized by relative entropy based coarse-graining of the confined KCl electrolyte system. Fig. 6.6 shows the water-water, ion-water, wall-water, and wall-ion CG potentials. From Fig. 6.7, we observe that the CG potentials can accurately predict the water and ion density profiles by CG MD simulations. We note that, unlike in *o*W water based CG representation of the confined KCl electrolyte system, in μW representation we do not assume a uniform permittivity.

6.4 Electrostatic correlations

As described in Section 2.1.2, fluid-fluid interactions give rise to the finite size, i.e., excluded volume effects, dispersion attraction, and particle-particle correlations in the fluid. A framework to incorporate fluid-fluid

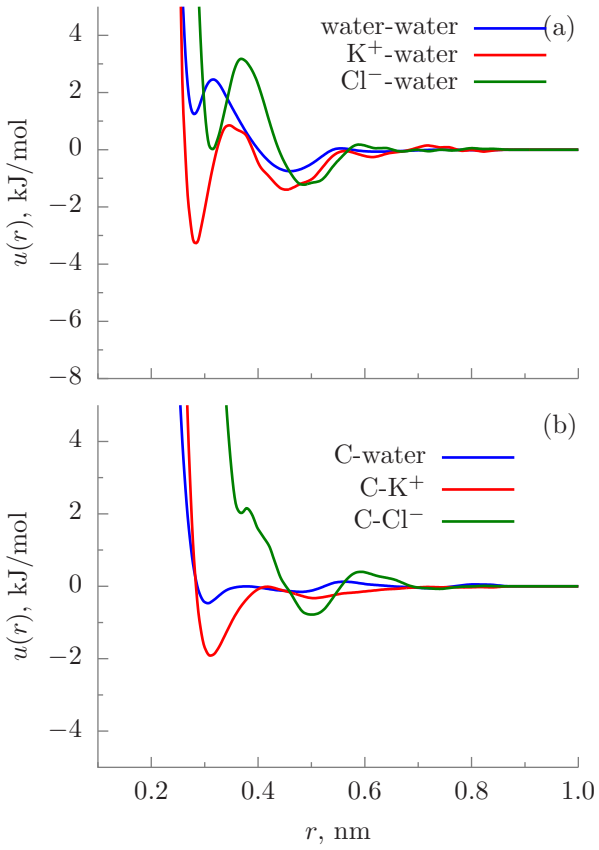

Figure 6.4: CG potentials in the *o*W water based CG representation of the KCl electrolyte system: (a) Water-water, K^+-water, and Cl^--water CG potentials and (b) C-water, C-K^+, and C-Cl^- CG potentials.

correlations is not known exactly. In LP-EQT (see Section 5.1.2), the fluid-fluid correlation part due to excluded volume and repulsive component of the vdW interactions is included by the hard sphere fluid approximation based on the White-Bear version of FMT mark II. However, the correlations due to the Coulombic interactions were ignored, and a mean-field approximation was used to compute the electrostatic potential.

Here, we include the electrostatic correlation contribution, $U^{\text{ff}}_{i,\text{elec-corr}}$, to the fluid-fluid potential as

$$U^{\text{ff}}_{i,\text{elec-corr}}(\boldsymbol{r}) = \sum_{j=1}^{3} \int_0^{R_{ij,\text{elec-corr}}} \rho_j(\boldsymbol{r}') u^{\text{ff}}_{ij,\text{elec-corr}}(r) d\boldsymbol{r}', \tag{6.1}$$

where, $u^{\text{ff}}_{ij,\text{elec-corr}}(r)$ is the electrostatic correlation component of the fluid-fluid interaction between the fluid molecules i and j and $R_{ij,\text{elec-corr}}$ defines the range for the electrostatic correlations. Therefore, the total

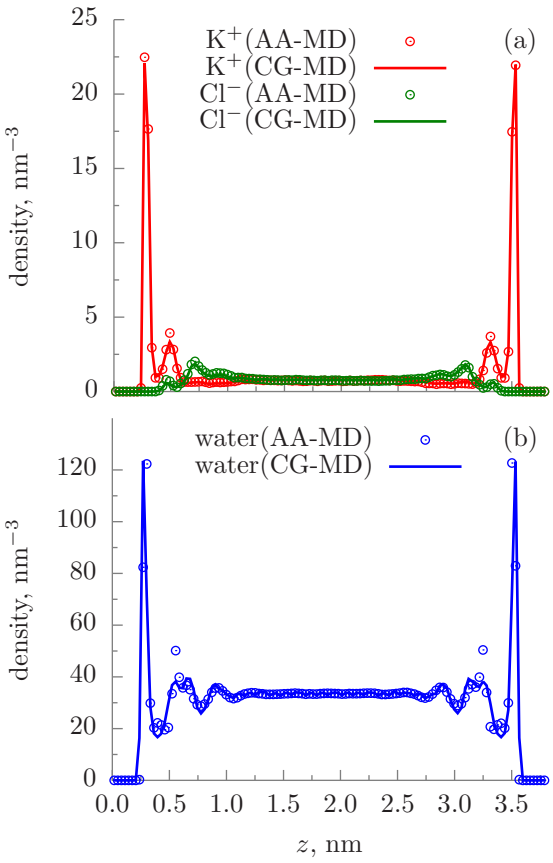

Figure 6.5: Comparisons of ion density profiles (a) and water COM density profile (b) from AA-MD and CG-MD with *o*W water based CG potentials of the confined KCl electrolyte system.

potential for a fluid molecule i is

$$U_i(\boldsymbol{r}) = U^{\text{wf}}_{i,\text{vdw}}(\boldsymbol{r}) + U^{\text{ff}}_{i,\text{vdw}}(\boldsymbol{r}) + U_{i,\text{elec}}(\boldsymbol{r}) + U^{\text{ff}}_{i,\text{elec-corr}}(\boldsymbol{r}). \tag{6.2}$$

The procedure to compute $U^{\text{wf}}_{i,\text{vdw}}(\boldsymbol{r})$, $U^{\text{ff}}_{i,\text{vdw}}(\boldsymbol{r})$, and $U_{i,\text{elec}}(\boldsymbol{r})$ is described in Section 5.1.

We estimate the electrostatic correlation component of the fluid-fluid interaction, $u^{\text{ff}}_{ij,\text{elec-corr}}(r)$, from a bulk residual direct correlation function, $\Delta c_{ij}(r)$, as

$$u^{\text{ff}}_{ij,\text{elec-corr}}(r) = -k_{\text{B}}T\Delta c_{ij}(r). \tag{6.3}$$

The residual direct correlation function is due to the short-range component of the Coulombic interactions

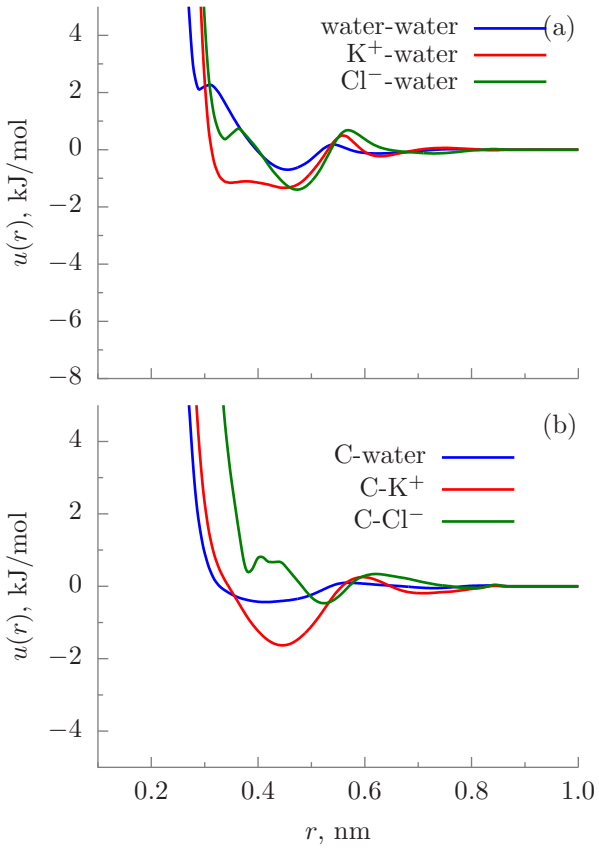

Figure 6.6: CG potentials in the μW water based CG representation of the KCl electrolyte system: (a) Water-water, K^+-water, and Cl^--water CG potentials and (b) C-water, C-K^+, and C-Cl^- CG potentials.

and is defined as [141, 53]

$$\Delta c_{ij}(r) = c_{ij}(r) - c_{ij,\mathrm{hs}}(r) + \frac{1}{k_\mathrm{B}T} u_{ij,\mathrm{vdw}}(r)\mathcal{H}\left(r - d_{ij,\mathrm{hs}}\right) + \frac{1}{k_\mathrm{B}T}\frac{q_i q_j}{4\pi\varepsilon_0\varepsilon_\mathrm{r} r}, \tag{6.4}$$

where $c_{ij}(r)$ is the direct correlation function and $c_{ij,\mathrm{hs}}(r)$ is the hard-sphere component of the direct correlation function between fluid particles i and j in the bulk electrolyte system. In Eq. 6.4, third term is the component of the direct correlation due to fluid-fluid vdW attractive interactions in a mean field approximation, $\mathcal{H}$ is a heaviside step function, $d_{ij,\mathrm{hs}} = \frac{d_{i,\mathrm{hs}}+d_{j,\mathrm{hs}}}{2}$ is the effective hard sphere diameter for the fluid pair $i-j$, and the fourth term is due to the mean-field Coulomb interaction. We obtain $c_{ij}(r)$ from the solution of the Ornstein-Zernike (OZ) equation with the hypernetted chain (HNC) closure relation [52]. For the HNC-based solution of the OZ equation in the bulk electolyte system, we use the water-water, ion-water, and ion-ion CG pair potentials obtained in Section 6.3. Similarly, $c_{ij,\mathrm{hs}}(r)$ is determined from the HNC solution of the OZ equation with the hard-sphere pair potentials. For $u_{ij,\mathrm{vdw}}(r)$, we use the CG potentials.

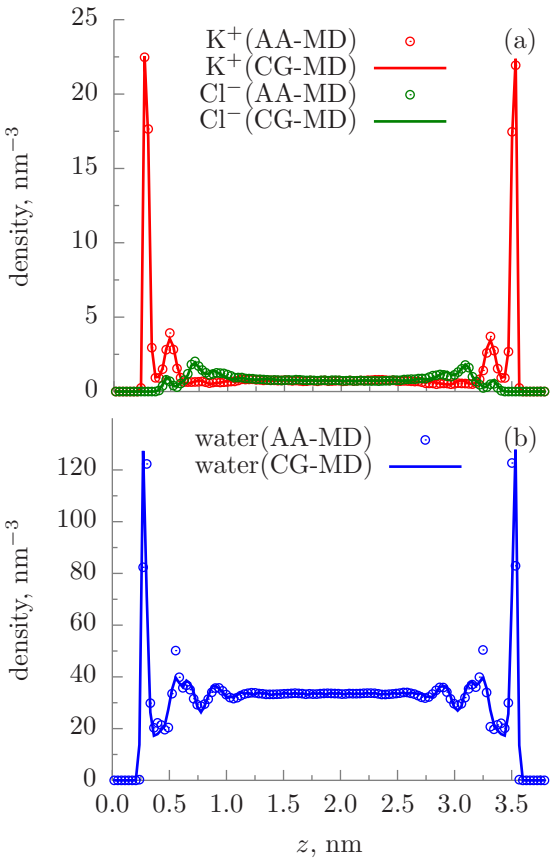

Figure 6.7: Comparisons of ion density profiles (a) and water COM density profile (b) from AA-MD and CG-MD with μW water based CG potentials of the confined KCl electrolyte system.

We note that, in Eq. 6.4, the attractive part of the vdW pair potential and long range electrostatics are treated in the mean-field sense, and the range, $R_{ij,\text{elec-corr}}$, of the residual correlations due to the short-range electrostatic interactions is similar to the hard-sphere diameter, $d_{ij,\text{hs}}$ [141, 53].

*o*W CG water

Fig. 6.8 shows the ion-ion residual direct correlation functions for the CG bulk 1 M KCl electrolyte system with *o*W CG water model and uniform permittivity of $\varepsilon_\text{r} = 78.5$. To compute $c_{ij,\text{hs}}(r)$, we use the hard-sphere diameters of 0.28, 0.18, and 0.32 nm for water CG bead, K^+, and Cl^-, respectively. We also verify the ion-water RDFs computed from the HNC-based solution of OZ equation using *o*W water CG potentials. Fig. 6.9 shows that the RDFs from HNC with the ion-water CG potentials compare well with the CG-MD RDFs. This suggests that HNC with the CG potentials can reliably predict the correlations in the bulk electrolyte system.

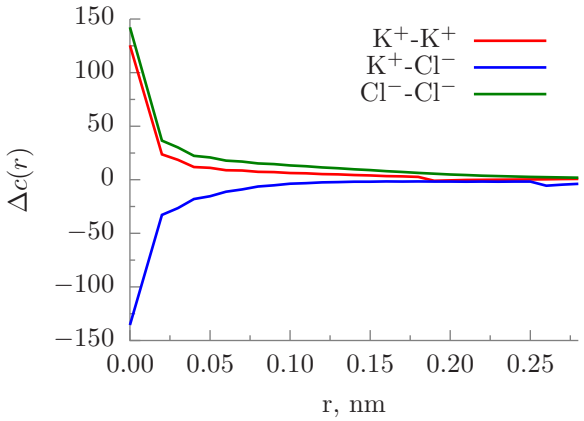

Figure 6.8: Residual direct correlations for the CG bulk 1M KCl electrolyte system using oW CG water model.

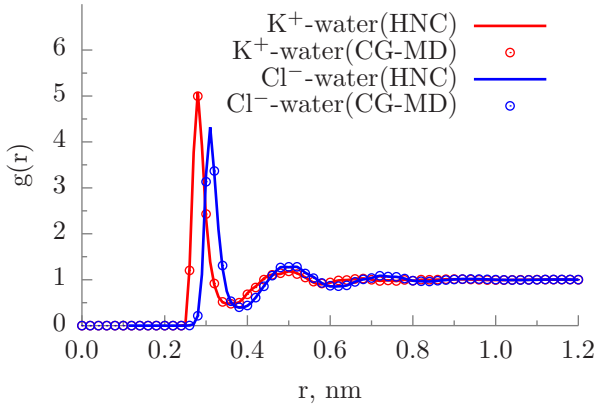

Figure 6.9: Comparisons of ion-water RDFs from CG-MD and HNC using oW CG water potentials.

μW CG water

Eqs. 6.1 and 6.3 assume the fluid-fluid electrostatic correlations are spherically symmetric. However, in the case of a point-dipole CG water model, μW, dipole-dipole and ion-dipole correlations are orientation dependent. Here, for numerical simplicity, we ignore dipole-dipole electrostatic correlations and incorporate the effects of ion-dipole correlations into an effective spherically symmetric ion-ion correlations defined as [8, 84],

$$c_{ij}^{\text{eff}}(r) = c_{ij}^{000}(r) + \rho_{\text{w}} \frac{c_{i-\text{w}}^{000}(r) c_{j-\text{w}}^{000}(r)}{1 - \rho_{\text{w}} c_{\text{w-w}}^{000}(r)} - \frac{1}{3}\rho_{\text{w}} \frac{c_{i-\text{w}}^{011}(r) c_{j-\text{w}}^{011}(r)}{1 - \rho_{\text{w}} \left(c_{\text{w-w}}^{110}(r) + 2c_{\text{w-w}}^{112}(r)\right)}, \tag{6.5}$$

where $c_{\alpha\beta}^{mnl}(r)$ are the projections of the direction correlation between fluid particles α and β in the rotational invariant based expansion [84]. We obtain $c_{\alpha\beta}^{mnl}(r)$ from the linearized hypernetted-chain (LHNC) [84, 54] approximation based solution of the OZ equation in the bulk electrolyte system. To solve OZ equation

with LHNC approximation, we follow the numerical scheme of Levesque et al. [84]. Then, the effective correlations, $c_{ij}^{\text{eff}}(r)$, can be substituted for $c_{ij}(r)$ in Eq. 6.4 to obtain ion-ion residual correlation for the μW CG water based electrolyte system.

Fig. 6.10 shows the ion-ion residual direct correlation functions for the CG bulk 1 M KCl electrolyte system with μW CG water model. To compute $c_{ij,\text{hs}}(r)$, we use the hard-sphere diameters of 0.28, 0.18, and 0.32 nm for water CG bead, K^+, and Cl^-, respectively. We also verify projections of the ion-water total correlations, $h_{i-\text{w}}^{mnl}(r)$, computed from the LHNC-based solution of OZ equation using μW water CG potentials. Fig. 6.11 shows that $h_{i-\text{w}}^{mnl}(r)$ from LHNC with the ion-dipole CG potentials compare well with the CG-MD results.

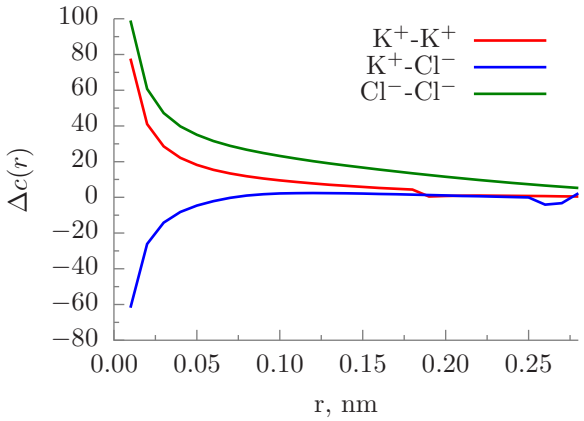

Figure 6.10: Ion-ion residual direct correlations for the CG bulk 1M KCl electrolyte system using μW CG water model.

6.5 Results

6.5.1 *o*W CG water

First, we use *o*W water based CG model of confined KCl electrolyte system in EQT to obtain ion and water density profiles. For the ion-ion interactions, we use the same LJ potentials that are used in the reference MD simulations. For the water-water, ion-water, wall-water, and wall-ion pair interactions, we use the systematically developed CG potentials discussed in Sec. 6.3. For all the pair potentials, we set $R_{ij,\text{cut}}^{\text{ff}} = 0.9$ nm. Here, we set $R_{ij,\text{min}}^{\text{ff}} = \sigma_{ij}^{\text{ff}}$ for the ion-ion LJ pair potentials, where σ_{ij}^{ff} is the usual LJ parameter. For the water-water and ion-water CG potentials, we set $R_{\text{ww,min}}^{\text{ff}} = 0.28\,\text{nm}$, $R_{\text{+w,min}}^{\text{ff}} = 0.262\,\text{nm}$, and $R_{\text{-w,min}}^{\text{ff}} = 0.314\,\text{nm}$. To compute the wall-fluid potential energies from Eq. 5.13, we use $\rho_{\text{wall}} = 38.18\,\text{atoms/nm}^3$ for the graphene walls. To determine the mean electrostatic potential, $\phi(z)$, we solve Eqs. 5.10 and 5.11 with

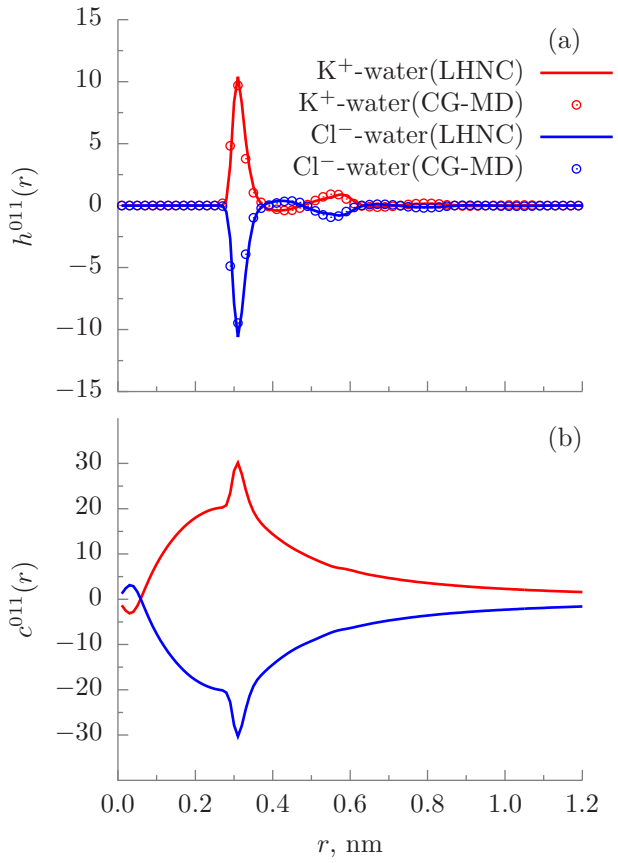

Figure 6.11: (a) Comparisons of ion-water total correlation $h^{011}(r)$ projections from CG-MD and LHNC for the CG bulk 1M KCl electrolyte using μW CG water model. (b) Ion-water direct correlation $c^{011}(r)$ projections.

$q_+ = +1.0\,\mathrm{e}$ and $q_- = -1.0\,\mathrm{e}$ and uniform permittivity of $\varepsilon_\mathrm{r} = 78.5$. The walls are equally charged such that $\sigma_{\text{wall-L}} = \sigma_{\text{wall-U}} = \sigma_{\text{wall}}$, where $\sigma_{\text{wall}} = -0.2265$ C/m^2. To determine the hard-sphere energy component from FMT (Eq. 5.15), we use $d_{\text{hs,w}} = 0.28\,\text{nm}$, $d_{\text{hs,+}} = 0.18\,\text{nm}$, and $d_{\text{hs,-}} = 0.32\,\text{nm}$. In addition, here, we also include the electrostatic correlations determined from Eq. 6.1 with the residual correlations shown in Fig. 6.8.

Fig. 6.12 shows the comparison of the density profiles from EQT and MD for water and ions. It can be seen that the water and ion density profiles from EQT compare well with the reference MD simulations. We show that the systematically obtained CG potentials and inclusion of electrostatic correlations improve the accuracy of EQT so that it can predict the charge inversion phenomenon well compared with the reference AA MD simulations.

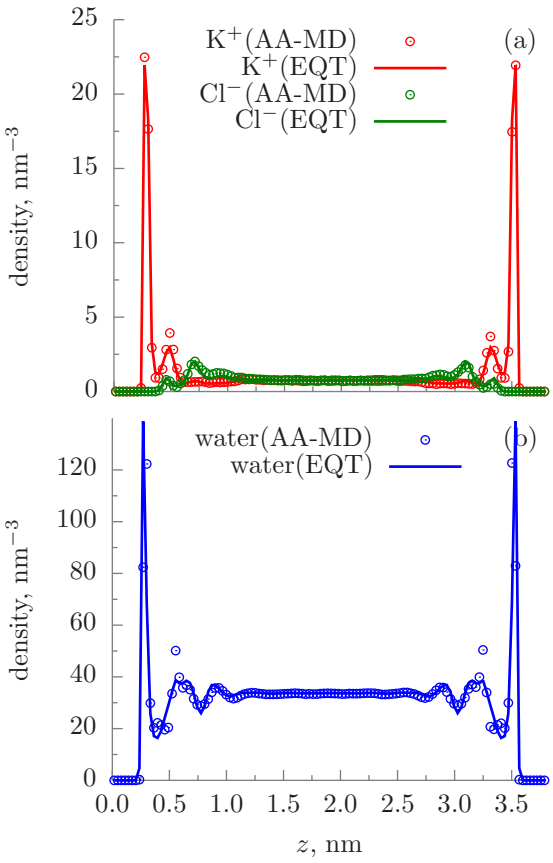

Figure 6.12: Comparisons of ion density profiles (a) and water COM density profile (b) from AA MD and EQT with oW water based CG potentials of the confined KCl electrolyte system.

6.5.2 μW CG water

As noted above, the main advantage of μW CG water model is that it can explicitly incorporate the spatially varying nature of the dielectric permittivity and the orientation polarization of water molecules near charged surfaces. Therefore, for μW CG water based EQT simulations of the confined KCl electrolyte system, we use the Langevin dipole based computation of the mean-field electrostatic potential as described in Section 5.1.1. In addition to the mean-field electrostatic potential, we include the ion-ion electrostatic correlations determined from Eq. 6.1 with the effective ion-ion residual correlations shown in Fig. 6.10. The remaining EQT simulation parameters are as follows.

For the ion-ion interactions, we use the same LJ potentials that are used in the reference MD simulations. For the water-water, ion-water, wall-water, and wall-ion pair interactions, we use the systematically developed CG potentials with μW CG water model as discussed in Sec. 6.3. For all the pair potentials, we set $R^{\text{ff}}_{ij,\text{cut}} = 0.9$ nm. Here, we set $R^{\text{ff}}_{ij,\text{min}} = \sigma^{\text{ff}}_{ij}$ for the ion-ion LJ pair potentials, where σ^{ff}_{ij} is

the usual LJ parameter. For the water-water and ion-water CG potentials, we set $R^{\text{ff}}_{\text{ww,min}} = 0.28\,\text{nm}$, $R^{\text{ff}}_{\text{+w,min}} = 0.32\,\text{nm}$, and $R^{\text{ff}}_{\text{-w,min}} = 0.338\,\text{nm}$. To compute the wall-fluid potential energies from Eq. 5.13, we use $\rho_{\text{wall}} = 38.18\,\text{atoms/nm}^3$ for the graphene walls. To determine the mean electrostatic potential, $\phi(z)$, we solve Eqs. 5.10 and 5.11 with $q_+ = +1.0\,\text{e}$, $q_- = -1.0\,\text{e}$, $\mu = 3.84\,\text{D}$ and spatially varying permittivity defined by Eq. 5.8. The walls are equally charged such that $\sigma_{\text{wall-L}} = \sigma_{\text{wall-U}} = \sigma_{\text{wall}}$, where $\sigma_{\text{wall}} = -0.2265$ C/m^2. To determine the hard-sphere energy component from FMT (Eq. 5.15), we use $d_{\text{hs,w}} = 0.28\,\text{nm}$, $d_{\text{hs,+}} = 0.18\,\text{nm}$, and $d_{\text{hs,-}} = 0.32\,\text{nm}$.

Fig. 6.13 shows the density profiles from EQT with μW CG water model. We observe that the EQT with μW CG water model and ion-ion effective electrostatic correlations fail to capture density profiles of ions accurately. The errors in the predictions of EQT can be attributed to the bulk-based approximation used to determine the ion-ion effective correlations from Eq. 6.5. We note that the ion-ion effective correlations depend on the ion-dipole correlations. It is known that near an interface the dipole orientation of water is widely different from the bulk water [78]. Therefore, the bulk-based ion-dipole correlations, which are used in Eq. 6.5, may not be accurate near the charged interface of EDL.

One approach to account for the orientation polarization effects of water dipoles on the ion densities near the interface is to obtain an effective wall-ion CG potential in EQT. We followed the similar approach for NaCl electrolyte confined inside capacitor channels in Section 5.4.2. We note that the wall-fluid CG potentials obtained in the CG-MD with oW CG water model account for the orientation polarization effects of SPC/E water on the ion densities. Therefore, here, to incorporate the interfacial orientation polarization effects of water on K^+ density, we use the same C-water and C-K^+ CG potentials obtained with oW CG model in CG-MD (see Fig. 6.4). For the wall-Cl^-, water-water, K^+-water, and Cl^--water, we use the μW water model based CG potentials. We also include the bulk-based ion-ion effective electrostatic residual correlations. Fig. 6.14 shows the comparison of the density profiles from EQT and MD for water and ions. It can be seen that, with appropriate wall-fluid CG potentials and ion-ion residual correlations from the bulk, the water and ion density profiles from EQT with μW CG water model compare well with the reference MD simulations.

6.6 Summary

In this chapter, we extended the LP-EQT framework to predict the charge inversion phenomenon in EDLs. We found that the ion-ion and ion-dipole electrostatic correlations are important for the charge inversion. We modeled the electrostatic correlations using the residual direct correlation functions of the bulk electrolyte.

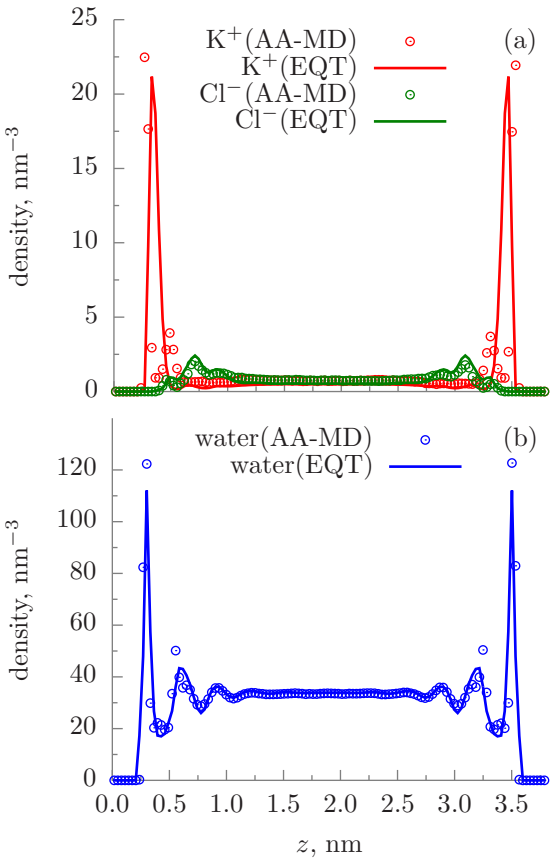

Figure 6.13: Comparisons of ion density profiles (a) and water COM density profile (b) from AA MD and EQT with μW water based CG potentials of the confined KCl electrolyte system.

The bulk residual direct correlation functions are determined from the HNC-based integral equation theory. We explored two coarse-grained representations for water molecule: oW CG water with no dipole and μW CG water with point dipole. We showed that, with the systematically obtained CG potentials and the inclusion of electrostatic correlations, EQT can predict the charge inversion phenomenon well compared to MD simulations.

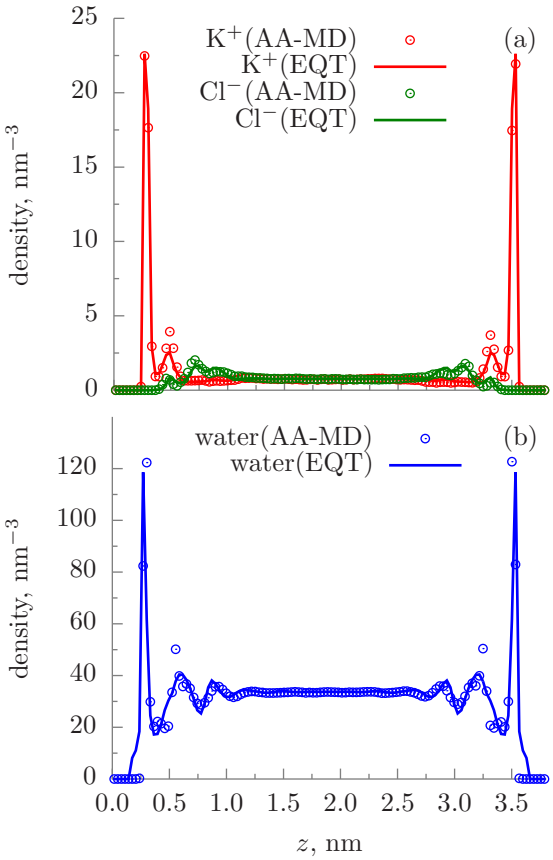

Figure 6.14: Comparisons of ion density profiles (a) and water COM density profile (b) from AA MD and EQT with μW water model and modified wall-water and wall-K$^+$ CG potentials in EQT.

Chapter 7

Integral equation coarse-graining approach

Most of the structure based coarse-graining approaches, such as iterative Boltzmann inversion (IBI) [119], inverse monte carlo (IMC) [90], and relative entropy [133] are numerical and iterative methods. In these iterative methods, a trial function is provided as a starting CG potential, which is then updated and optimized iteratively until a given error metric is minimized. Each iterative step requires canonical sampling of the coarse-grained system, which is done using either molecular dynamics (MD), stochastic dynamics (SD), or Monte Carlo (MC) techniques. To ensure the convergence of the iterative coarse-graining schemes, statistically reliable CG ensemble configurations are required, which can be obtained by selecting sufficiently large system size and long simulation length. The costs of the coarse-grained simulation and analysis of the CG ensemble configurations increase with the size of the system, i.e., number of particles, and the length of the simulation, i.e., number of time steps. Therefore, sampling of the coarse-grained systems and analysis of the CG ensemble configurations at each iteration step are computationally expensive and dominate the overall cost of the iterative coarse-graining approaches. Furthermore, special care must be taken, such as smoothing of the potential updates, to ensure the stability of the numerical iterative schemes [126].

In this chapter, we present a direct and computationally efficient theoretical procedure for coarse-graining. The theoretical procedure is based on the hypernetted chain closure (HNC) in the integral equation (IE) theory. HNC closure provides a direct approach to estimate an effective pair potential from a target distribution function without performing atomistic simulations. Therefore, HNC-based coarse-graining (HNC-CG) is a computationally efficient approach to obtain CG potentials. In Section 7.1, we provide theoretical and numerical details about HNC-based coarse-graining procedure. In Section 7.2, we demonstrate HNC-based coarse-graining procedure by determining CG potentials for the bulk water and water-methanol mixture systems.

7.1 Method

The goal for the coarse-grained model is to reproduce the target radial distribution function (RDF) of the reference system. The radial distribution function, $g(r)$, where $r = |\boldsymbol{r} - \boldsymbol{r}_0|$, is a conditional probability density, relative to the ideal gas limit, of finding a particle at a distance r away from a given reference particle at $\boldsymbol{r}_0$[51]. In the integral equation theory, for a uniform and isotropic system, the relation between an effective pair potential, $u(r)$, and RDF, $g(r)$, is defined as [52]

$$g(r) = \exp\left(-\beta u(r) + h(r) - c(r) + b(r)\right), \tag{7.1}$$

where, $\beta = \frac{1}{k_{\mathrm{B}}T}$, $h(r)$ is the total correlation function, $c(r)$ is the direct correlation function, and $b(r)$ is the bridge function. The total correlation function, $h(r)$, is the difference between the radial distribution function and its random value of unity,

$$h(r) = g(r) - 1. \tag{7.2}$$

The total correlation, $h(r)$, can be defined as a sum of the direct correlation part, $c(r)$, and the indirect correlations due to the propagation of the interactions via surrounding particles. This relation between $h(r)$ and $c(r)$ is given by the Ornstein-Zernike (OZ) equation as

$$h(r) = c(r) + \rho \int c\left(|\boldsymbol{r} - \boldsymbol{r}'|\right) h(r') d\boldsymbol{r}', \tag{7.3}$$

where ρ is the uniform density of the bulk system.

The exact expression for the bridge function, $b(r)$, in Eq. 7.1 is not known. There exists several approximations, known as 'closure approximations', to solve Eq. 7.1, such as the Percus-Yevick (PY) closure, mean spherical approximation (MSA) closure, and hyper-netted chain (HNC) approximation [52]. Here, we use HNC closure approximation, which ignores the bridge function as

$$g(r) = \exp\left(-\beta u(r) + h(r) - c(r)\right). \tag{7.4}$$

HNC closure approximation maps three-body and higher-order many-body contributions into an effective pair potential. Therefore, it provides a direct and analytical route to estimate an effective CG potential from a pair distribution. Given a target $g(r)$ and the thermodynamic state, i.e., ρ and T, of the reference system, the effective CG potential between coarse-grained particles can be obtained by inverting the HNC closure

Eq. 7.4 as

$$u(r) = k_{\mathrm{B}}T\left(h(r) - c(r) - \ln(g(r))\right). \tag{7.5}$$

The numerical procedure to obtain CG potentials from Eq. 7.5 is as follows. For a target RDF, $g(r)$, which can be obtained from an all-atom simulations or experimental data, $h(r)$ is determined from Eq. 7.2. Then, the OZ equation (Eq. 7.3) is solved to obtain $c(r)$. We follow the numerical procedure described in [152] to solve the OZ equation. Once $c(r)$ is determined, the effective CG potential between CG sites is determined from Eq. 7.5. We note that, for the short separation distances where $g(r) \to 0$, $u(r)$ values needs to be extrapolated.

7.2 Results

To illustrate functionality of the HNC-CG coarse-graining method, we coarse-grain two systems: an SPC/E bulk water system and a system consisting of a methanol-water mixture.

7.2.1 Bulk water

For coarse-graining the bulk water, we consider bulk water at a thermodynamic state of 300 K temperature and 1 bar pressure. In the coarse-grained model, we represent one water molecule by one CG bead positioned at its center of mass (COM), such that the CG beads solely interact via an isotropic two-body potential. The target RDF is determined from the reference all-atom ensemble configurations generated in the NVT ensemble [126]. Using the HNC-CG method, we obtain the water-water coarse-grained interaction. Fig. 7.1 shows the CG potential determined from HNC for bulk water. We, then, use the HNC-based water-water CG potential to perform the molecular simulations of the CG water system. Fig. 7.1 shows the water-water RDFs from the CG simulation along with the reference RDF from the AA simulation. We observe that the water-water RDF from the HNC-based CG potential compare well with reference RDF from AA simulations.

In Fig. 7.1, we also compare the HNC-based water-water CG potential to that from the relative entropy optimization (see Section B). It can be seen that the CG potential from HNC is very similar to the optimized CG potential from relative entropy minimization.The small differences between the CG potentials from the HNC and relative entropy minimization could be attributed to the bridge function approximation in the HNC closure.

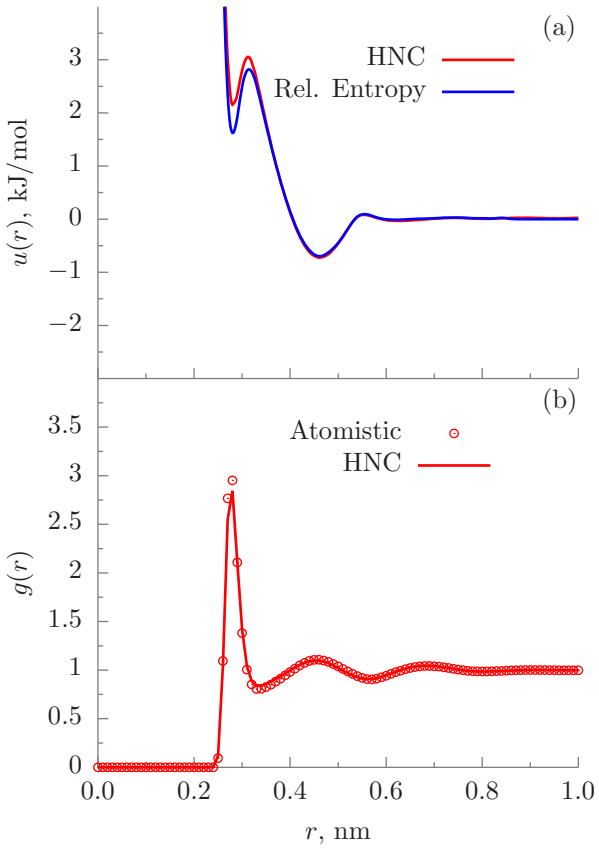

Figure 7.1: CG potential (a) and RDFs (b) for bulk water. CG potential from the HNC-CG procedure accurately predicts the water-water COM RDF.

7.2.2 Water-methanol mixture

Iterative coarse-graining methods, such IBI, can have convergence problems for multicomponent systems [126]. IBI ignores the cross-correlation terms and hence, its convergence can be slower and may require relaxation (i.e., multiplying factor $\chi \in (0...1)$) of the update function. On the other hand, IMC is more rigorous than IBI and accounts for the cross-correlations, but it is computationally costly and requires large configurational sampling to achieve good accuracy. See [126] for detailed comparisons of IBI and IMC methods.

HNC-based CG approach is rigorously derived from the statistical mechanics. As described in Section 7.1, HNC closure along with the OZ equation maps three-body and higher-order many-body contributions into an effective pair potential. Therefore, cross-correlation terms are explicitly considered in determining CG potentials from HNC.

Here, to demonstrate robustness of the HNC-based coarse-graining for multicomponent systems, we consider an equimolar water-methanol mixture. In the CG model for the water-methanol mixtures, water

and methanol molecules are represented by CG beads positioned at their COM and the interactions between CG beads are modeled via isotropic two-body potentials. The reference water-water, methanol-methanol, and methanol-water RDFs are generated from the all-atom simulations. See Section B.4 for the details about the reference atomistic simulations. To obtain the direct correlations between three different pairs, which are required to solve Eq. 7.5, we solve a multicomponent version of the OZ equation [152]. Fig. 7.2 shows the CG potentials for the water-water, methanol-methanol, and methananol-water pairs determined from HNC. We, then, use the HNC-based water-water CG potential to perform the molecular simulations of the CG water-methanol system. Fig. 7.1 shows the RDFs from the CG simulations compare well with the reference RDFs from AA simulations.

7.3 Summary

In this chapter, we developed HNC-based direct and computationally efficient coarse-graining approach. We demonstrated HNC-CG method by coarse-graining water and methanol-water mixture systems. We showed that the RDFs from the CGMD with HNC-based CG potentials compare well with the target RDF from AAMD. Also, we found that the CG potentials from HNC are very close to the iterative systematic coarse-graining approaches like relative entropy minimization.

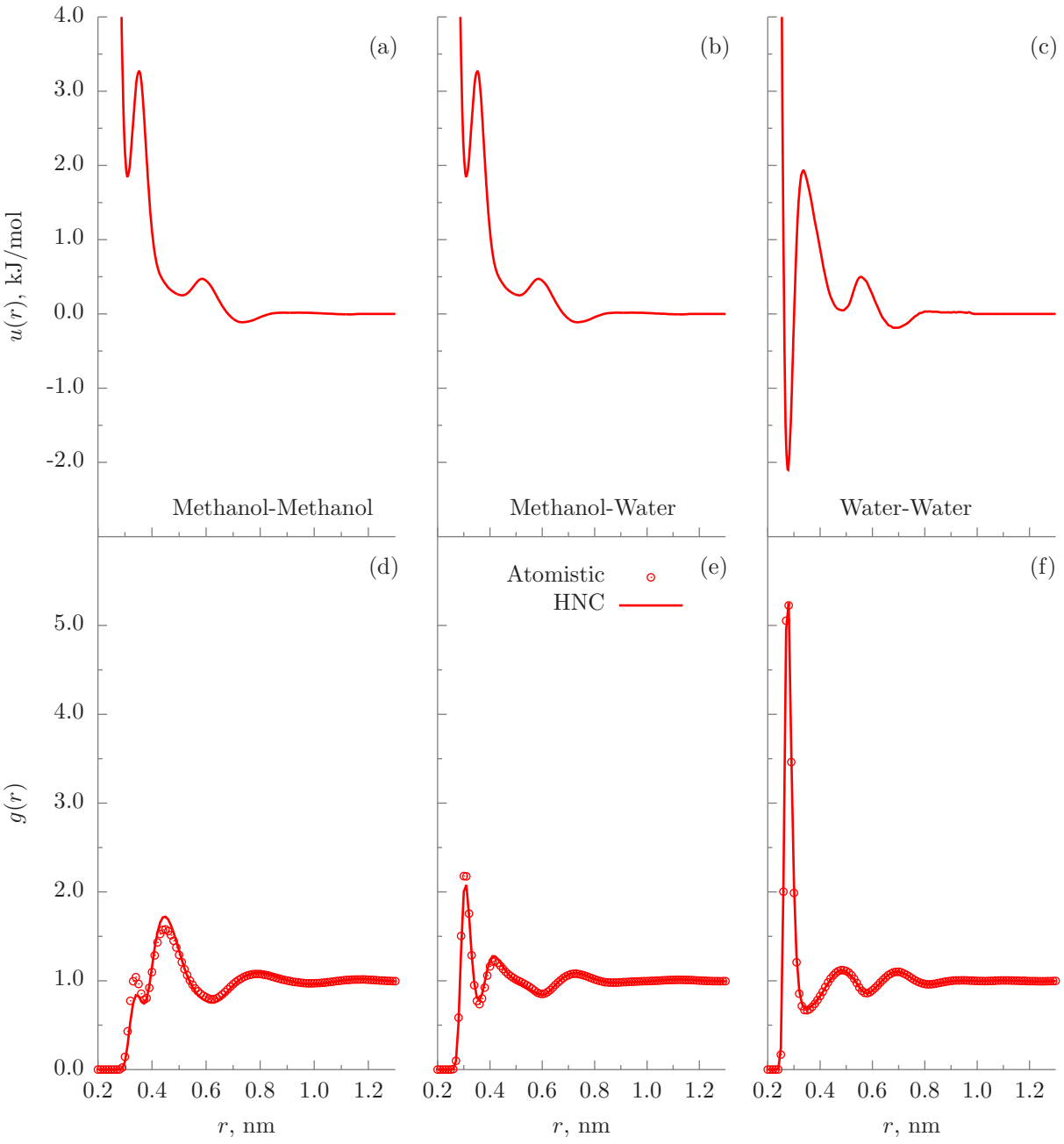

Figure 7.2: CG potentials and RDFs of methanol-water. CG potentials from the HNC-CG procedure predict water-water, methanol-water, and methanol-methanol COM RDFs accurately.

Chapter 8

Conclusions

The concluding remarks of this research work are as follows:

- We presented an empirical potential-based quasi-continuum theory (EQT) to predict the density and potential profiles of confined fluids. Determining the fluid-fluid potential of a confined fluid is the most challenging part of the continuum-based approach. We developed different approaches to determine the fluid-fluid potentials in EQT, namely a soft-core potential approach, correlation correction approach, and fundamental measure theory (FMT) approach. We showed that all three approaches can accurately predict the density profiles of a confined fluid. We observed that the soft-core potential has a similar form as the direct correlation function of the fluid. Therefore, the soft-core potential does not only address the numerical issues due to a steep-repulsion component of the fluid-fluid pair potential in the continuum approximation but also accurately captures the fluid-fluid correlations in the confined system. The correlation correction approach is based on the spline functional form and hence, it is the most flexible approach. On the other hand, the FMT-based approach is the most rigorous approach and has only the hard-sphere diameter as the free parameter to set.

- To extend EQT framework to molecular fluids like confined water, we developed a systematic coarse-graining approach to optimize structurally consistent coarse-grained potentials. We systematically coarse-grain degrees of freedom of confined water from the detailed all-atom level to the cheaper particle-based CG level, and to the continuum-based EQT level. It is found that the relative entropy based coarse-graining technique can be used to derive structurally consistent CG-MD potentials for the confined water. For determination of the EQT effective potentials, we developed a PMF-matching technique, and it is found to be a robust technique to derive effective potentials, which can be used in EQT to accurately predict the density profiles of the confined water. Both the wall-water and water-water CG potentials are found to be significantly dependent on the thermodynamic state. However, for all the thermodynamic states studied, it is found that the water-water CG potential exhibits so-called core-softened double-well type characteristics, whose energy-scales are significantly state dependent,

whereas length-scales change very little. Also, it is shown that the 2-point linear interpolation formula can be useful to derive the CG potentials at thermodynamic states other than the one optimized here.

- We developed an explicit water based theoretical framework for studying EDLs. This framework is based on the EQT and point dipole based coarse-grained water model. In EQT, water polarization and dielectric permittivity variations are modeled using the Langevin dipole approach. Finite size effects of water and ions are approximated by the White-Bear mark II (WBII) version of FMT. To accurately capture hydration interactions, we systematically developed water-water and ion-water coarse-grained potentials by relative entropy minimization. We demonstrated EQT by simulating the NaCl aqueous electrolyte confined inside slit-like capacitor channels for various ion concentrations and surface charge densities. EQT predictions of the water and ion density profiles agree well with the reference MD simulations.

- We extended the EQT framework to include short-range electrostatic correlations so that it can predict the charge inversion phenomenon. We showed that systematically obtained CG potentials and inclusion of electrostatic correlations improve the accuracy of EQT and it can predict the charge inversion phenomenon well compared to MD simulations.

- We presented a multiscale continuum-based method to predict the thermodynamic properties in addition to the structure of confined fluids. The multiscale method is a combination of two approaches, namely, EQT and cDFT. We developed a free energy functional for cDFT based on EQT potentials. We demonstrated the EQT-cDFT approach by simulating methane and argon confined in slit-like graphene channels of various widths. The EQT-cDFT predictions for the structure and thermodynamic properties, like the density, adsorption, local pressure tensor, surface tension, and solvation force, compare well with the MD simulations. Therefore, the EQT-cDFT approach is a promising approach to accurately predict the structure and thermodynamic properties of confined fluids.

- We presented hypernetted chain (HNC) theory based direct and computationally efficient theoretical procedure for coarse-graining. HNC closure provides a direct approach to estimate an effective pair potential from a target distribution function without performing atomistic simulations. We demonstrated HNC-based coarse-graining procedure by determining CG potentials for the bulk water and water-methanol mixture systems. CG potentials from HNC can be used to perform CG-MD simulations. We found that the pair distribution functions from the CG-MD simulations compare well with the reference atomistic simulations.

Appendix A

Fundamental measure theory

Rosenfeld's fundamental measure theory (FMT) provides a functional to determine the excess (over the ideal gas) free energy of hard-sphere mixtures, $F_{\rm hs}\left[\{\rho_i\}\right]$, as [121, 124]

$$\beta F_{\rm hs}\left[\{\rho_i\}\right] = \int d\boldsymbol{r}' \Phi\left(\{n_\alpha\left(\boldsymbol{r}'\right)\}\right), \tag{A.1}$$

where $\beta = \frac{1}{k_{\rm B}T}$, Φ is the reduced free energy density, and $\{n_\alpha\}$ are the set of weighted densities. The weighted densities for the ν-component mixture are defined as

$$n_\alpha\left(\boldsymbol{r}\right) = \sum_i^\nu \int d\boldsymbol{r}' \rho_i\left(\boldsymbol{r}'\right) \omega_\alpha^i\left(\boldsymbol{r}-\boldsymbol{r}'\right), \tag{A.2}$$

where ω_α^i are the weight functions given by

$$\begin{aligned}
\omega_3^i\left(\boldsymbol{r}\right) &= \Theta\left(R_{i,\rm hs}-r\right), \\
\omega_2^i\left(\boldsymbol{r}\right) &= \delta\left(R_{i,\rm hs}-r\right), \\
\boldsymbol{\omega}_2^i\left(\boldsymbol{r}\right) &= \frac{\boldsymbol{r}}{r}\delta\left(R_{i,\rm hs}-r\right), \\
\omega_1^i\left(\boldsymbol{r}\right) &= \frac{\omega_2^i\left(\boldsymbol{r}\right)}{4\pi R_{i,\rm hs}}, \\
\omega_0^i\left(\boldsymbol{r}\right) &= \frac{\omega_2^i\left(\boldsymbol{r}\right)}{4\pi R_{i,\rm hs}^2}, \\
\boldsymbol{\omega}_1^i\left(\boldsymbol{r}\right) &= \frac{\boldsymbol{\omega}_2^i\left(\boldsymbol{r}\right)}{4\pi R_{i,\rm hs}}.
\end{aligned} \tag{A.3}$$

In Eq. A.3, $R_{i,\rm hs} = \frac{d_{i,\rm hs}}{2}$ is the hard-sphere radius of the molecule i, $d_{i,\rm hs}$ is the hard-sphere diameter of the molecule i, $\Theta(r)$ is the Heaviside step function, $\delta(r)$ is the Dirac-delta distribution, and $r = |\boldsymbol{r}|$. The integrations over ω_α^i (Eq. A.2) give the *fundamental measures* of a fluid i, such as the volume ($\alpha = 3$), the surface area ($\alpha = 2$), the mean radius of curvature ($\alpha = 1$), and the Euler characteristics ($\alpha = 0$).

Various functions for the reduced free energy density, $\Phi\left(\{n_\alpha\left(\boldsymbol{r}'\right)\}\right)$, are derived from the different thermo-

dynamic conditions [124]. For example, the original Rosenfeld functional based on the scaled-particle theory equation, the White-Bear (WB) functional based on the Mansoori-Carnahan-Starling-Leland (MCSL) equation of state, and the White-Bear mark II (WBII) functional, which is similar to the WB functional but is constructed to reproduce the Carnahan-Starling-Boublík equation of state for a one-component bulk fluid. In this work, we use the WBII version of FMT. In WBII, the reduced free energy density is given by

$$\begin{aligned}\Phi &= -n_0 \ln\left(1-n_3\right) + \left(n_1 n_2 - \boldsymbol{n}_1 \cdot \boldsymbol{n}_2\right) \frac{1+\frac{1}{3}\phi_2\left(n_3\right)}{1-n_3} \\ &\quad + \left(n_2^3 - 3 n_2 \boldsymbol{n}_2 \cdot \boldsymbol{n}_2\right) \frac{1-\frac{1}{3}\phi_3\left(n_3\right)}{24\pi\left(1-n_3\right)^2},\end{aligned} \tag{A.4}$$

where

$$\phi_2\left(n_3\right) = \frac{1}{n_3}\left(2n_3 - n_3^2 + 2\left(1-n_3\right)\ln\left(1-n_3\right)\right) \tag{A.5}$$

and

$$\phi_3\left(n_3\right) = \frac{1}{n_3^2}\left(2n_3 - 3n_3^2 + 2n_3^3 + 2\left(1-n_3\right)^2\ln\left(1-n_3\right)\right). \tag{A.6}$$

From Eqs. A.1 and A.2, we determine $U_{i,\mathrm{hs}}^{\mathrm{ff}}$, required in Eq. 5.14, as

$$U_{i,\mathrm{hs}}^{\mathrm{ff}}(\boldsymbol{r}) = \frac{\delta F_{\mathrm{hs}}\left[\{\rho_i\}\right]}{\delta\rho_i\left(\boldsymbol{r}\right)} = k_{\mathrm{B}}T\sum_{\alpha}\int d\boldsymbol{r}'\frac{\partial\Phi\left(\{n_\alpha\}\right)}{\partial n_\alpha}\frac{\delta n_\alpha\left(\boldsymbol{r}'\right)}{\delta\rho_i\left(\boldsymbol{r}\right)}. \tag{A.7}$$

For a 1-D slit channel, the weighted densities expression, Eq. A.2, simplifies to [124]

$$n_\alpha\left(\boldsymbol{r}\right) = n_\alpha\left(z\right) = \sum_i \int dz'\rho_i\left(z'\right)\omega_\alpha^i\left(z-z'\right), \tag{A.8}$$

where the one dimensional weight functions are

$$\begin{aligned}\omega_3^i\left(z\right) &= \pi\left(R_i^2 - z^2\right)\Theta\left(R_i - |z|\right), \\ \omega_2^i\left(z\right) &= 2\pi R_i\Theta\left(R_i - |z|\right), \\ \boldsymbol{\omega}_2^i\left(z\right) &= 2\pi z\boldsymbol{e}_z\Theta\left(R_i - |z|\right), \\ \omega_1^i\left(z\right) &= \frac{\omega_2^i\left(z\right)}{4\pi R_i}, \\ \omega_0^i\left(z\right) &= \frac{\omega_2^i\left(z\right)}{4\pi R_i^2}, \\ \boldsymbol{\omega}_1^i\left(z\right) &= \frac{\boldsymbol{\omega}_2^i\left(z\right)}{4\pi R_i},\end{aligned} \tag{A.9}$$

where $\boldsymbol{e}_z$ is the unit vector in the z-direction. Similarly, the expression for $U^{\mathrm{ff}}_{i,\mathrm{hs}}$, Eq. A.7, simplifies to

$$U^{\mathrm{ff}}_{i,\mathrm{hs}}(z) = \frac{\delta F_{\mathrm{hs}}\left[\{\rho_i\}\right]}{\delta \rho_i\left(z\right)} = k_{\mathrm{B}}T \sum_{\alpha} \int dz' \frac{\partial \Phi\left(\{n_\alpha\}\right)}{\partial n_\alpha} \frac{\delta n_\alpha\left(z'\right)}{\delta \rho_i\left(z\right)}. \tag{A.10}$$

To evaluate the integrations in Eqs. A.8 and A.10, we use the numerical scheme given by Knepley et al. [2].

Appendix B

Relative entropy based coarse-graining

B.1 Relative entropy

Relative entropy, S_{rel}, is defined as [133]

$$S_{\text{rel}} = \sum_i p_{\text{AA}}(r_i) \ln \left(\frac{p_{\text{AA}}(r_i)}{p_{\text{CG}}\left(M(r_i)\right)} \right) + \langle S_{\text{map}} \rangle_{\text{AA}}, \tag{B.1}$$

where the sum is over all the configurations of the reference AA system, $r = \{r_i\}(i = 1, 2, ...)$, M is the mapping operation to generate a corresponding CG configuration, R_I, from a AA configuration, r_i, i.e., $R_I = M(r_i)$, p_{AA} and p_{CG} are the configurational probabilities based on the AA and CG potentials, respectively, and $\langle S_{\text{map}} \rangle_{\text{AA}}$ is the mapping entropy due to the average degeneracy of AA configurations mapping to the same CG configuration, given by

$$S_{\text{map}}(R_I) = \ln \sum_i \delta_{R_I, M(r_i)}, \tag{B.2}$$

where δ is the Kronecker delta function. From Eq. B.2, it can be shown that the mapping entropy, $\langle S_{\text{map}} \rangle_{\text{AA}}$, does not depend on the CG interactions, but instead it is a unique function of the mapping operation, M, and the AA configurational weights. The relative entropy is a metric borrowed from the field of information theory, which quantifies the extent of the configurational phase-space overlap between two molecular ensembles [156]. The log-likelihood based derivation of the relative entropy for molecular systems, as defined in Eq. B.1, is given in ref. [133]. Physically, S_{rel} can be interpreted as the log probability that one test configuration of the model CG ensemble is representative of the target AA ensemble, and when the likelihood is a maximum, S_{rel} is at a minimum. Hence, the numerical minimization of S_{rel} with respect to the parameters of the CG model can be used to optimize the CG model.

Comparisons between relative entropy and other coarse-graining methods are made in ref. [125] and [25]. Chaimovich and Shell [25] have shown that for certain CG models relative entropy minimization produces the same CG potentials as other methods, e.g., it is equivalent to the IBI when CG interactions are modeled

using finely tabulated pair additive potentials, and to the FM when a CG model is based on $N-$body interactions, where N is the number of degrees of freedom in the CG model. However, there are some advantages of using relative entropy based coarse-graining. Relative entropy method allows to use analytical function forms for CG potentials, which are desired in theoretical treatments, such as parametric study of CG potentials, whereas, methods, like IBI, use tabulated potentials. Recently Lyubartsev et. al [89] have shown how to use IMC with an analytical function form, too. BI, IBI, and IMC methods are based on pair correlations and hence, they are only useful to optimize 2-body CG potentials, whereas, relative entropy uses more generic metric which offers more flexibility in modeling CG interactions and not only 2-body, but also 3-body and N-body CG potentials can be optimized. In addition to the CG potential optimization, the relative entropy metric can also be used to optimize an AA to CG mapping operator.

In a canonical ensemble, substituting canonical configurational probabilities into Eq. B.1, the relative entropy simplifies to

$$S_{\mathrm{rel}} = \beta\langle U_{\mathrm{CG}} - U_{\mathrm{AA}}\rangle_{\mathrm{AA}} - \beta\left(A_{\mathrm{CG}} - A_{\mathrm{AA}}\right) + \langle S_{\mathrm{map}}\rangle_{\mathrm{AA}}, \tag{B.3}$$

where $\beta = 1/k_{\mathrm{B}}T$, k_{B} is the Boltzmann constant, T is the temperature, U_{CG} and U_{AA} are the total potential energies from the CG and AA potentials, respectively, A_{CG} and A_{AA} are the configurational part of the Helmholtz free energies from the CG and AA potentials, respectively, and all the averages are computed in the reference AA ensemble.

Consider a model CG system defined by the CG potentials between various CG sites such that the CG potentials depend on the parameters $\boldsymbol{\lambda} = \{\lambda_1, \lambda_2, ...\lambda_n\}$. As described above, in the relative entropy based coarse-graining, the CG potential parameters, $\boldsymbol{\lambda}$, are optimized by the relative entropy minimization.

In this work, we use the Newton-Raphson strategy for the relative entropy minimization described in ref. [25]. In this strategy, the CG potential parameters, $\boldsymbol{\lambda}$, are refined iteratively as

$$\boldsymbol{\lambda}^{k+1} = \boldsymbol{\lambda}^{k} - \chi\mathbf{H}^{-1}\cdot\nabla_{\lambda}S_{\mathrm{rel}}, \tag{B.4}$$

where k is the iteration index, $\chi \in (0...1)$ is the relaxation parameter that can be adjusted to ensure convergence, $\nabla_{\lambda}S_{\mathrm{rel}}$ is the vector of the first derivatives of S_{rel} with respect to $\boldsymbol{\lambda}$, which can be computed from Eq. B.3 as

$$\nabla_{\lambda}S_{\mathrm{rel}} = \beta\left\langle\frac{\partial U_{\mathrm{CG}}}{\partial\lambda}\right\rangle_{\mathrm{AA}} - \beta\left\langle\frac{\partial U_{\mathrm{CG}}}{\partial\lambda}\right\rangle_{\mathrm{CG}}, \tag{B.5}$$

and $\mathbf{H}$ is the Hessian matrix of S_{rel} given by

$$\begin{aligned}\mathbf{H}_{ij} &= \beta\left\langle\frac{\partial^2 U_{\text{CG}}}{\partial\lambda_i\partial\lambda_j}\right\rangle_{\text{AA}} - \beta\left\langle\frac{\partial^2 U_{\text{CG}}}{\partial\lambda_i\partial\lambda_j}\right\rangle_{\text{CG}} \\ &\quad +\beta^2\left\langle\frac{\partial U_{\text{CG}}}{\partial\lambda_i}\frac{\partial U_{\text{CG}}}{\partial\lambda_j}\right\rangle_{\text{CG}} \\ &\quad -\beta^2\left\langle\frac{\partial U_{\text{CG}}}{\partial\lambda_i}\right\rangle_{\text{CG}}\left\langle\frac{\partial U_{\text{CG}}}{\partial\lambda_j}\right\rangle_{\text{CG}}. \end{aligned} \tag{B.6}$$

To compute $\nabla_\lambda S_{\text{rel}}$ and $\mathbf{H}$ from Eq. B.5 and B.6, we need average CG energy derivatives in the AA and CG ensembles. For the averages in the AA ensemble, first a single AA system simulation can be performed and its AA configurations can be saved, then the average CG energy derivatives can be computed by processing the mapped CG configurations of the saved AA configurations using the CG potentials at each iteration. For the averages in the CG ensemble, since the CG ensemble changes with the CG parameters, $\boldsymbol{\lambda}$, a short CG simulation can be performed at each iteration to generate corresponding CG configurations. An alternative approach, which does not require a CG simulation at every iteration, to obtain the CG ensemble averages is to reweight the initial CG configurations obtained from $\boldsymbol{\lambda}^0$ [25]. In this work, we implemented the first approach based on performing a short CG simulation at every iteration.

In the case of a CG model, in which CG interactions are modeled by a two-body pair potential, u_{CG}, between CG sites, the ensemble averages of the CG energy derivatives can be computed as

$$\begin{aligned}\left\langle\left(\frac{\partial^a U_{\text{CG}}}{\partial\lambda^a}\right)^b\right\rangle_{\text{AA}} &= \left\langle\left(\sum_{i<j}\frac{\partial^a u_{\text{CG}}(r_{ij})}{\partial\lambda^a}\right)^b\right\rangle_{\text{AA}} \\ \left\langle\left(\frac{\partial^a U_{\text{CG}}}{\partial\lambda^a}\right)^b\right\rangle_{\text{CG}} &= \left\langle\left(\sum_{i<j}\frac{\partial^a u_{\text{CG}}(r_{ij})}{\partial\lambda^a}\right)^b\right\rangle_{\text{CG}}, \end{aligned} \tag{B.7}$$

where the sum is performed over all the CG site pairs (i, j), a stands for the 1st, 2nd,... derivatives and b stands for the different powers, i.e., $b = 1, 2, ...$

B.2 Implementation

We implemented the relative entropy-based coarse-graining method in an open-source coarse-graining software called Versatile Object-Oriented Toolkit for Coarse-graining Applications (VOTCA) [126, 98]. In the VOTCA package, we implemented the relative entropy-based coarse-graining method using the iterative workflow framework described in ref. [126]. Required inputs are the pair distributions of the CG sites in the reference AA ensemble, the initial guess for the CG potential parameters, the CG ensemble simulation set

up files, and the option file describing the modeling options for the CG interactions. Furthermore, the user can provide the Newton-Raphson iteration parameters, such as the relaxation parameter, χ, the convergence check criteria, etc.

To describe the CG potentials, we use the uniform cubic B-spline (CBSPL) form given by

$$u_{\mathrm{CBSPL}}(r) = \begin{bmatrix} 1 & t & t^2 & t^3 \end{bmatrix} \frac{1}{6} \begin{bmatrix} 1 & 4 & 1 & 0 \\ -3 & 0 & 3 & 0 \\ 3 & -6 & 3 & 0 \\ -1 & 3 & -3 & 1 \end{bmatrix} \begin{bmatrix} c_k \\ c_{k+1} \\ c_{k+2} \\ c_{k+3} \end{bmatrix}, \tag{B.8}$$

where $\{c_0, c_1, c_2, ..., c_m\}$ are the spline knot values tabulated for m evenly spaced intervals of size $\Delta r = r_{\mathrm{cut}}/(m-2)$ along the separation distance $r_i = i \times \Delta r$ with the cut-off r_{cut}, and t is given by

$$t = \frac{r - r_k}{\Delta r}, \tag{B.9}$$

where index k is determined such that $r_k \leq r < r_{k+1}$. We choose CBSPL form because it exhibits remarkable flexibility, and it can represent various complex functional characteristics of pair potentials for sufficiently large number of knots.

To ensure the stability of the relative entropy minimization, some precautionary measures are taken. For the Newton-Raphson update to converge towards a minimum, the Hessian, $\mathbf{H}$, must be positive definite at each step. With a good initial guess for the CG parameters and by adjusting the value of the relaxation parameter, χ, stability of the Newton-Raphson method can be ensured. One approach to initialize the CG parameters can be to fit them to PMF obtained by inverting the pair distributions of the CG sites obtained from the reference AA ensemble. For the CBSPL form, which is linear in it's parameters, the second derivative of S_{rel} is never negative, hence the minimization converges to a single global minimum. However, due to locality property of the CBSPL form, i.e., update to c_i affects only the value of the potential near r_i, and the poor sampling of the very small separation distances in the high repulsive core, the rows of $\mathbf{H}$ corresponding to the first few spline knots in the repulsive core may become zero causing $\mathbf{H}$ to be a singular matrix. To avoid this singularity issue, we specify a minimum separation distance, r_{min}, for each CG pair interaction and remove the spline knots corresponding to the $r \leq r_{\mathrm{min}}$ region from the Newton-Raphson update. Once the remaining knot values are updated, the knot values in the poorly sampled region, i.e., $r \leq r_{\mathrm{min}}$, can be extrapolated. The value of r_{min} can be estimated from the minimum distance at which the reference CG pair distribution is nonzero. Also, to ensure that the CG pair potentials and forces go

smoothly to zero near r_{cut}, couple of knot values before and after r_{cut} are fixed to zero.

For the convergence check, we define two types of errors: (i) the CG parameter error, ϵ_λ, given by

$$\epsilon_\lambda^k = \sum_{i=0}^{n-1} \left(\lambda_i^k - \lambda_i^{k-1}\right)^2, \tag{B.10}$$

where n is the total number of CG parameters to be optimized, k is the index of the iteration step and (ii) the CG potential error, ϵ_u, given by

$$\epsilon_u^k = \sum_{i=0}^{M-1} \sum_{j=0}^{N-1} \left(u_i^k(r_j) - u_i^{k-1}(r_j)\right)^2, \tag{B.11}$$

where M is the number of CG pair potentials to be optimized, and N is the the number of discrete points used to model CG potentials. Then, the total error, ϵ_{tot}, is defined as

$$\epsilon_{\text{tot}}^k = w_\lambda\, \epsilon_\lambda^k + w_u\, \epsilon_u^k, \tag{B.12}$$

where w_λ and w_u are the weights assigned to the CG parameter error and the CG potential error, respectively. Iterations are terminated when ϵ_{tot} is less than the specified tolerance value or the specified limit of maximum number of iterations is reached. Finally, due to stochastic nature of the CG simulations, optimal parameters are computed by evaluating their average over the last few iterations.

B.3 Coarse-graining of bulk water

In the past, water has already been studied extensively from the point of view of both all-atom and coarse-grained representations [106, 150, 67, 151, 101, 69, 49]. CG potentials for bulk water obtained by IBI, IMC, and FM methods using the VOTCA package can be found in ref. [126]. In this work, we coarse-grain SPC/E bulk water at a thermodynamic state of 300 K temperature and 1 bar pressure using the simplex and relative entropy methods. In the coarse-grained model, we represent one water molecule by one CG bead positioned at its center of mass (COM), such that the CG beads solely interact via an isotropic two-body potential. Note, that representing multiple water molecules within one CG bead is also possible [93, 105]. Previously, Shell [133] and Chaimovich and Shell [24] have already employed the relative entropy method to optimize CG potentials for SPC/E water at various thermodynamic states, providing an appropriate reference for comparison. Also, recently Lu et al. [88] derived a series of coarse-grained potentials for various water models, TIP3P, SPC/E, TIP4P-Ew, and TIP4P/2005, using the relative entropy method and systematically

compared the ability of these CG potentials to reproduce various structural, dynamic, and thermodynamic properties of water.

For the reference all-atom ensemble, we use the same bulk water all-atom configurations as in the NVT ensemble generated in ref. [126]. The all-atom system consisted of 2180 water molecules in a cubic box of size 4.031 nm. The coarse-grained system consisted of 2180 CG beads which are obtained by mapping the all-atom configuration using a COM mapping scheme.

Using the relative entropy method, we optimized the CBSPL functional form, Eq. B.8, for the water-water coarse-grained interaction. For the CBSPL form, we have used a cutoff distance of 0.9 nm, fixed the grid spacing to 0.02 nm, and set $r_{\min} = 0.24$ nm, i.e., only the knot values corresponding to the region, $r > r_{\min}$, are optimized, and the knot values in the poorly sampled region, $r \leq r_{\min}$, are extrapolated. Therefore, there are 48 CG parameters for the water-water CG potential. The initial guess for the CG potential parameters was obtained by a least-square fitting of the CBSPL functional form to the PMF obtained by inverting the water-water COM pair distribution function from the reference AA ensemble. At each iteration, a CG simulation of 200 ps is performed with the GROMACS simulation software. For the first iteration, the initial configuration for the CG simulation is obtained by mapping the last configuration of the reference AA ensemble trajectory. For all subsequent iterations, the final CG configuration from the previous step is used as an initial configuration for the CG simulation. Furthermore, at each iteration, CG configurations corresponding to the first 50 ps are discarded as equilibration stage and only the configurations of the last 150 ps stored at 1 ps intervals are used to compute the update for the CG potential parameters.

Fig. B.1a shows the optimized CG potentials for bulk water. It can be seen that, the water-water CG potential has a core-softened double-well-type shape, which is a very characterisitc of the water-water CG potential [24, 126]. Fig. B.1 shows the water-water RDFs from the CG simulation along with the reference RDF from the AA simulation. One observes that the relative entropy-based CG potential is able to predict the water-water RDF accurately. The accuracy of the RDF from the relative entropy-based CG potential is consistent with the analysis made in ref. [125] and [25]. In these references, it is demonstrated that, when CG potentials are modeled using a finely tabulated functional form such as CBSPL, the relative entropy minimization would result in the CG potentials similar to IBI and IMC, which reproduce the target AA ensemble pair distributions.

B.4 Coarse-graining of water-methanol mixtures

To further test robustness of the relative entropy method and its implementation within the VOTCA package, we consider a much more complex system, namely a water-methanol mixture. Methanol is the smallest alcohol and its structural properties feature a winding hydrogen-bonded chains with an average of approximately 2 hydrogen bonds per molecule [70]. Coarse-grained potentials for pure liquid methanol system have been determined by IBI, IMC, and FM methods in ref. [126]. In addition, a water-methanol mixture is a suitable system for studies of several structural aspects of solvation in aqueous mixtures [80].

In this study, we considered 3 different water-methanol mixtures with methanol mole fractions, X_m, of 0.062 (diluted), 0.5 (equimolar), and 0.938 (concentrated), similar to the ones used in ref [80]. Reference AA simulations were performed in the NVT ensemble using the GROMACS simulation software[62]. Water is modeled using the SPC/E model, whereas the OPLS [72] force field was used to model methanol, and the LJ interaction parameters, namely C_{12} and C_6, for the cross-interactions between water and methanol are determined using a geometric mean rule. The number of molecules and average densities of the simulated solutions are given in Table B.1. All three mixtures were simulated in a cubic box of length 5.05691 nm with periodic boundary conditions, at 300 K temperature maintained using the Nosé-Hoover thermostat [108]. Systems were equilibrated for 5 ns each, followed by production runs of 20 ns. Reference radial distributions have been computed using snapshots at every 1 ps and a bin size of 0.01 nm.

Table B.1: Simulated water-methanol mixtures.

	I	II	III
number of H_2O	3752	2000	248
number of MeOH	248	2000	3752
X_m	0.062	0.5	0.938
ρ g/cm^3	0.97	0.885	0.80

In the CG model for the water-methanol mixtures, water and methanol molecules are represented by CG beads positioned at their COM and the interactions between CG beads are modeled via isotropic two-body potentials. The number of water and methanol molecules in the CG simulations are the same as in the reference AA simulations (see Table B.1).

For the relative entropy-based coarse-graining, we have used the CBSPL form, Eq. B.8, to model all three CG interactions, i.e., water-water, water-methanol, and methanol-methanol interactions. For the water-water CG potential, a cut-off distance of 1.0 nm was used with the grid spacing of 0.01 nm and $r_{\min} = 0.24$ nm. For the water-methanol and methanol-methanol CG potentials, a cut-off distance of 1.32 nm was used with the grid spacing of 0.02 nm. $r_{\min}$ for the water-methanol and methanol-methanol CG potentials was set to 0.27 and 0.3 nm, respectively. Therefore, there are total of 241 (103 for water-water,

69 for water-methanol and methanol-methanol) CG parameters to be optimized. At each iteration, a CG simulation of 500 ps is performed with the GROMACS and the CG configurations corresponding to the first 100 ps are discarded as equilibration stage and the configurations of the last 400 ps stored at 1 ps intervals are used to compute the update for the CG potential parameters.

The CG potentials obtained from the relative entropy minimization for the three different water-methanol mixtures are shown in Fig. B.2 along with the corresponding RDFs obtained from the CG simulations. Observations about the accuracy of the CG potentials from the relative entropy method is similar to that of the bulk water case. As expected, due to the finely tabulated nature of the CBSPL functional form, the CG potentials from the relative entropy optimization are able to predict the water-water, water-methanol, and methanol-methanol RDFs as accurately as the reference AA simulations. We note that the CG potentials for the water-methanol mixture system are different for different mole-fractions. This is not surprising, because it is well-known that the CG potentials depend on the thermodynamic state of the reference system [69, 151]. However, it is possible to optimize CG potentials for multiple state-points simultaneously [104], but it is beyond the scope of this work.

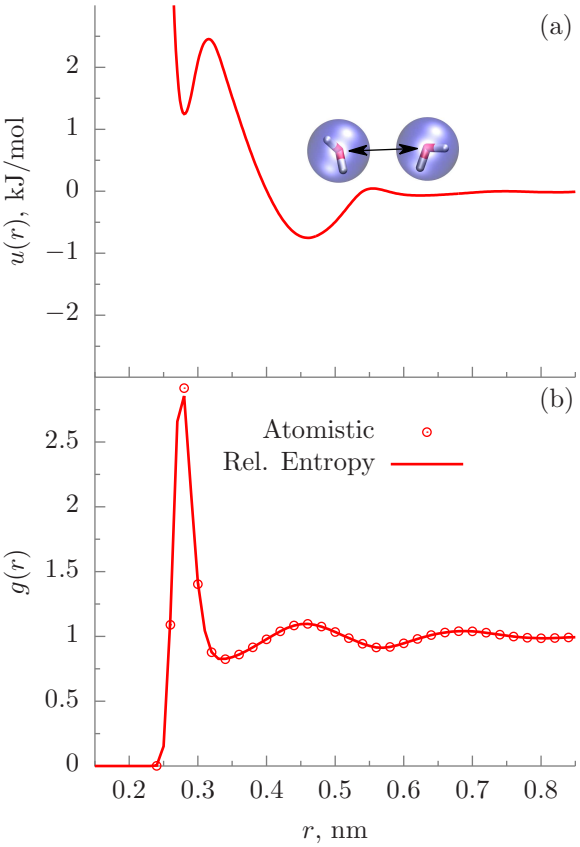

Figure B.1: CG potential (a) and RDFs (b) for bulk water. CG potential from the relative entropy minimization accurately predicts the water-water COM RDF.

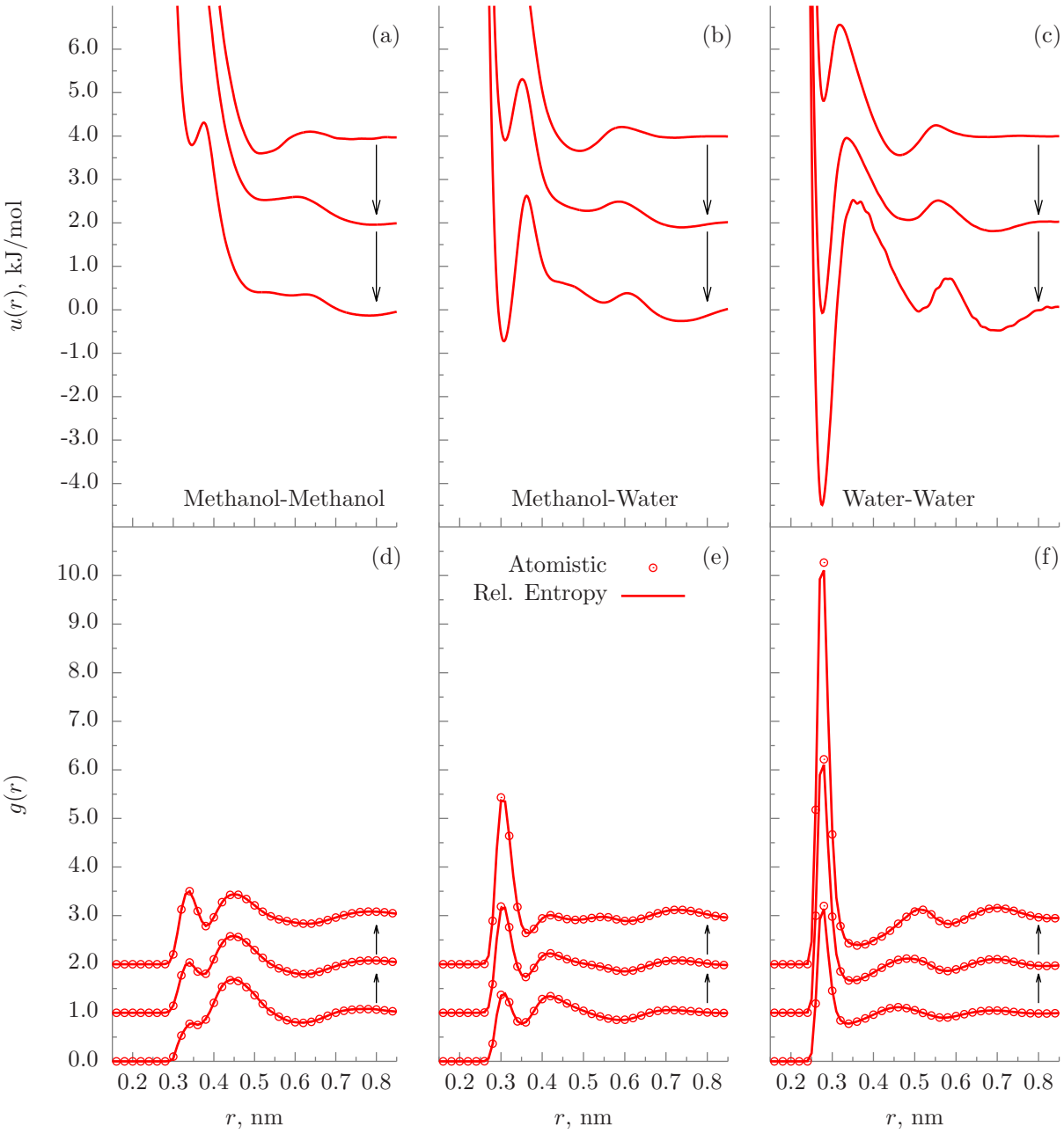

Figure B.2: CG potentials and RDFs of methanol-water: mixture at different methanol mole fractions, $X = 0.062, 0.5, 0.938$ are shown. Arrow indicates the direction of increasing X. CG potentials from the relative entropy minimization predict water-water, methanol-water, and methanol-methanol COM RDFs accurately for all mole fractions.

References

[1] Chapter 6 - Inhomogeneous Fluids. Oxford.

[2] An efficient algorithm for classical density functional theory in three dimensions: Ionic solutions. 132.

[3] The Electric Double Layer.

[4] https://github.com/symashayak/gromacs/tree/release-4-6-1-localpressure_slab.

[5] A review of reverse osmosis membrane materials for desalinationDevelopment to date and future potential. 370.

[6] A transferable coarse-grained potential to study the structure of confined, supercritical Lennard-Jones fluids. 132.

[7] Electric Double Layers. In J. Lyklema, editor, *Fundamentals of Interface and Colloid Science*, volume 2 of *Solid-Liquid Interfaces*, pages 3–1. Academic Press, 1995.

[8] S. A. Adelman. The effective direct correlation function: An approach to the theory of liquid solutions. *The Journal of Chemical Physics*, 64:724–731, 1976.

[9] M. P. Allen and D. J. Tildesley. *Computer Simulation of Liquids*. Oxford University Press, 1989.

[10] S. Attinger and P. Koumoutsakos. *Multiscale Modeling and Simulation*. Springer, New York,, 2004.

[11] Perla B. Balbuena, David Berry, and Keith E. Gubbins. Solvation pressures for simple fluids in micropores. *The Journal of Physical Chemistry*, 97:937–943, 1993.

[12] V. Ballenegger and J.-P. Hansen. Structure and dielectric properties of polar fluids with extended dipoles: results from numerical simulations. *Molecular Physics*, 102:599–609, 2004.

[13] V. Ballenegger and J.-P. Hansen. Dielectric permittivity profiles of confined polar fluids. *The Journal of Chemical Physics*, 122:114711, 2005.

[14] Murat Barisik and Ali Beskok. Equilibrium molecular dynamics studies on nanoscale-confined fluids. *Microfluidics and Nanofluidics*, 11:269–282, 2011.

[15] H. J. C. Berendsen, J. R. Grigera, and T. P. Straatsma. The missing term in effective pair potentials. *The Journal of Physical Chemistry*, 91:6269–6271, 1987.

[16] Amit Bhattacharya and Pallab Ghosh. NANOFILTRATION AND REVERSE OSMOSIS MEMBRANES: THEORY AND APPLICATION IN SEPARATION OF ELECTROLYTES. *Reviews in Chemical Engineering*, 20:111–173, 2004.

[17] Olle Björneholm, Martin H. Hansen, Andrew Hodgson, Li-Min Liu, David T. Limmer, Angelos Michaelides, Philipp Pedevilla, Jan Rossmeisl, Huaze Shen, Gabriele Tocci, Eric Tyrode, Marie-Madeleine Walz, Josephina Werner, and Hendrik Bluhm. Water at Interfaces. *Chemical Reviews*, 116:7698–7726, 2016.

[18] Lesser Blum and D. Henderson. Mixtures of hard ions and dipoles against a charged wall: The OrnsteinZernike equation, some exact results, and the mean spherical approximation. *The Journal of Chemical Physics*, 74:1902–1910, 1981.

[19] Lydric Bocquet and Elisabeth Charlaix. Nanofluidics, from bulk to interfaces. *Chemical Society Reviews*, 39:1073–1095, 2010.

[20] Douwe Jan Bonthuis, Stephan Gekle, and Roland R. Netz. Dielectric Profile of Interfacial Water and its Effect on Double-Layer Capacitance. *Physical Review Letters*, 107:166102, 2011.

[21] Douwe Jan Bonthuis and Roland R. Netz. Beyond the Continuum: How Molecular Solvent Structure Affects Electrostatics and Hydrodynamics at SolidElectrolyte Interfaces. *The Journal of Physical Chemistry B*, 117:11397–11413, 2013.

[22] Itamar Borukhov, David Andelman, and Henri Orland. Steric effects in electrolytes: A modified Poisson-Boltzmann equation. *Physical review letters*, 79:435, 1997.

[23] Gordon E. Brown and George A. Parks. Sorption of Trace Elements on Mineral Surfaces: Modern Perspectives from Spectroscopic Studies, and Comments on Sorption in the Marine Environment. *International Geology Review*, 43:963–1073, 2001.

[24] Aviel Chaimovich and M. Scott Shell. Anomalous waterlike behavior in spherically-symmetric water models optimized with the relative entropy. 11:1901–1915, 2009.

[25] Aviel Chaimovich and M. Scott Shell. Coarse-graining errors and numerical optimization using a relative entropy framework. *The Journal of Chemical Physics*, 134:094112, 2011.

[26] Martin F. Chaplin. Structuring and Behaviour of Water in Nanochannels and Confined Spaces. In Prof Lawrence J. Dunne and Dr George Manos, editors, *Adsorption and Phase Behaviour in Nanochannels and Nanotubes*, pages 241–255. Springer Netherlands, 2010.

[27] Martin F. Chaplin. Structuring and Behaviour of Water in Nanochannels and Confined Spaces. In Lawrence J. Dunne and George Manos, editors, *Adsorption and Phase Behaviour in Nanochannels and Nanotubes*, pages 241–255. Springer Netherlands, Dordrecht, 2010.

[28] B. E. Conway. *Electrochemical Supercapacitors Scientific Fundamentals and Technological Applications /*. Springer US,, Boston, MA :, 1999.

[29] Tom Darden, Darrin York, and Lee Pedersen. Particle mesh Ewald: An Nlog(N) method for Ewald sums in large systems. *The Journal of Chemical Physics*, 98:10089–10092, 1993.

[30] Sanjit K. Das, Mukul M. Sharma, and Robert S. Schechter. Solvation force in confined molecular fluids using molecular dynamics simulation. *Journal of Physical Chemistry*, 100:7122–7129, 1996.

[31] Petra S. Dittrich and Andreas Manz. Lab-on-a-chip: microfluidics in drug discovery. *Nature Reviews Drug Discovery*, 5:210–218, 2006.

[32] R. Eppenga and D. Frenkel. Monte Carlo study of the isotropic and nematic phases of infinitely thin hard platelets. *Molecular Physics*, 52:1303–1334, 1984.

[33] Hossein Eslami and Nargess Mehdipour. Local chemical potential and pressure tensor in inhomogeneous nanoconfined fluids. *The Journal of Chemical Physics*, 137:144702–144702–7, 2012.

[34] R. Evans. The nature of the liquid-vapour interface and other topics in the statistical mechanics of non-uniform, classical fluids. *Advances in Physics*, 28:143–200, 1979.

[35] R. Evans. Density Functional Theory For Inhomogeneous Fluids I: Simple Fluids in Equilibrium. *Lectures at 3rd Warsaw School of Statistical Physics, Kazimierz Dolny*, 27, 2009.

[36] R. Evans and T. J. Sluckin. A density functional theory for inhomogeneous charged fluids. *Molecular Physics*, 40:413–435, 1980.

[37] Karim Farah, Aoife Catherine Fogarty, Michael Christian Böhm, and Florian Müller-Plathe. Temperature dependence of coarse-grained potentials for liquid hexane. *Physical Chemistry Chemical Physics*, 13:2894–902, 2011.

[38] Amir Barati Farimani, Kyoungmin Min, and Narayana R. Aluru. DNA Base Detection Using a Single-Layer MoS $_2$. *ACS Nano*, 8:7914–7922, 2014.

[39] Guang Feng, Rui Qiao, Guoqing Hu, and Narayana R. Aluru. Structure of the Electrical Double Layers: Insights from Continuum and Atomistic Simulations. *Computational Bioengineering*, page 327, 2015.

[40] Daan Frenkel and Berend Smit. *Understanding Molecular Simulation: From Algorithms to Applications*. Academic Press, 2001.

[41] Amalie L. Frischknecht, Deaglan O. Halligan, and Michael L. Parks. Electrical double layers and differential capacitance in molten salts from density functional theory. *The Journal of Chemical Physics*, 141:054708, 2014.

[42] Phillip L. Geissler. Water Interfaces, Solvation, and Spectroscopy. *Annual Review of Physical Chemistry*, 64:317–337, 2013.

[43] N. Giovambattista, P.J. Rossky, and P.G. Debenedetti. Computational Studies of Pressure, Temperature, and Surface Effects on the Structure and Thermodynamics of Confined Water. *Annual Review of Physical Chemistry*, 63:179–200, 2012.

[44] Guy J. Gloor, George Jackson, F. J. Blas, E. Martn del Ro, and E. de Miguel. Prediction of the VaporLiquid Interfacial Tension of Nonassociating and Associating Fluids with the SAFT-VR Density Functional Theory. *The Journal of Physical Chemistry C*, 111:15513–15522, 2007.

[45] Guy J. Gloor, George Jackson, Felipe J. Blas, Elvira Martn del Ro, and Enrique de Miguel. An accurate density functional theory for the vapor-liquid interface of associating chain molecules based on the statistical associating fluid theory for potentials of variable range. *The Journal of Chemical Physics*, 121:12740–12759, 2004.

[46] Teena Goel, Chandra N. Patra, Swapan K. Ghosh, and Tulsi Mukherjee. Structure of cylindrical electric double layers: A systematic study by Monte Carlo simulations and density functional theory. *The Journal of Chemical Physics*, 129:154906, 2008.

[47] Ekaterina Gongadze and Ale Igli. Asymmetric size of ions and orientational ordering of water dipoles in electric double layer model - an analytical mean-field approach. *Electrochimica Acta*, 178:541–545, 2015.

[48] Ekaterina Gongadze, Alja Velikonja, arka Perutkova, Peter Kramar, Alenka Maek-Lebar, Veronika Kralj-Igli, and Ale Igli. Ions and water molecules in an electrolyte solution in contact with charged and dipolar surfaces. *Electrochimica Acta*, 126:42–60, 2014.

[49] Kevin R. Hadley and Clare McCabe. Coarse-Grained Molecular Models of Water: A Review. *Molecular simulation*, 38:671–681, 2012.

[50] Jongyoon Han, Jianping Fu, and Reto B. Schoch. Molecular sieving using nanofilters: Past, present and future. *Lab on a Chip*, 8:23–33, 2007.

[51] Jean-Pierre Hansen and Ian R. McDonald. Chapter 2 - Statistical Mechanics. In Jean-Pierre Hansen and Ian R. McDonald, editors, *Theory of Simple Liquids (Fourth Edition)*, pages 13–59. Academic Press, Oxford, 2013.

[52] Jean-Pierre Hansen and Ian R. McDonald. Chapter 4 - Distribution Function Theories. In Jean-Pierre Hansen and Ian R. McDonald, editors, *Theory of Simple Liquids (Fourth Edition)*, pages 105–147. Academic Press, Oxford, 2013.

[53] Jean-Pierre Hansen and Ian R. McDonald. Ionic Liquids. In *Theory of Simple Liquids*, pages 403–454. Elsevier, 2013.

[54] Jean-Pierre Hansen and Ian R. McDonald. Molecular Liquids. In *Theory of Simple Liquids*, pages 455–510. Elsevier, 2013.

[55] V. I. Harismiadis, J. Vorholz, and A. Z. Panagiotopoulos. Efficient pressure estimation in molecular simulations without evaluating the virial. *The Journal of Chemical Physics*, 105:8469–8470, 1996.

[56] Remco Hartkamp, A. Ghosh, T. Weinhart, and S. Luding. A study of the anisotropy of stress in a fluid confined in a nanochannel. *The Journal of Chemical Physics*, 137:044711–044711–19, 2012.

[57] Mohammad Heiranian, Amir Barati Farimani, and Narayana R. Aluru. Water desalination with a single-layer MoS2 nanopore. *Nature Communications*, 6:8616, 2015.

[58] Douglas Henderson. *Fundamentals of Inhomogeneous Fluids*. CRC Press, 1992.

[59] Douglas Henderson and Dezs Boda. Insights from theory and simulation on the electrical double layer. *Physical Chemistry Chemical Physics*, 11:3822–3830, 2009.

[60] Douglas Henderson, De-en Jiang, Zhehui Jin, and Jianzhong Wu. Application of Density Functional Theory To Study the Double Layer of an Electrolyte with an Explicit Dimer Model for the Solvent. *The Journal of Physical Chemistry B*, 116:11356–11361, 2012.

[61] J.R. Henderson and Frank van Swol. On the interface between a fluid and a planar wall. *Molecular Physics*, 51:991–1010, 1984.

[62] Berk Hess, Carsten Kutzner, David van der Spoel, and Erik Lindahl. GROMACS 4: Algorithms for highly efficient, load-balanced, and scalable molecular simulation. *Journal of Chemical Theory and Computation*, 4:435–447, 2008.

[63] M. Heuberger, M. Zch, and N. D. Spencer. Density Fluctuations Under Confinement: When Is a Fluid Not a Fluid? *Science*, 292:905–908, 2001.

[64] N. Hilal, H. Al-Zoubi, N. A. Darwish, A. W. Mohammad, and M. Abu Arabi. A comprehensive review of nanofiltration membranes:Treatment, pretreatment, modelling, and atomic force microscopy. *Desalination*, 170:281–308, 2004.

[65] Jessica Hughes, Eric J Krebs, and David Roundy. A classical density-functional theory for describing water interfaces. *The Journal of Chemical Physics*, 138:024509–024509, 2013.

[66] Jacob Israelachvili and Hkan Wennerstrm. Role of hydration and water structure in biological and colloidal interactions. *Nature*, 379:219–225, 1996.

[67] Sergei Izvekov and Gregory A. Voth. A Multiscale Coarse-Graining Method for Biomolecular Systems. *The Journal of Physical Chemistry B*, 109:2469–2473, 2005.

[68] Jian Jiang, Dapeng Cao, Douglas Henderson, and Jianzhong Wu. Revisiting density functionals for the primitive model of electric double layers. *The Journal of Chemical Physics*, 140:044714, 2014.

[69] Margaret E. Johnson, Teresa Head-Gordon, and Ard A. Louis. Representability problems for coarse-grained water potentials. *The Journal of Chemical Physics*, 126:144509–144509–10, 2007.

[70] William L Jorgensen. Optimized intermolecular potential functions for liquid alcohols. *Journal of Physical Chemistry*, 90:1276–1284, 1986.

[71] William L. Jorgensen and Jeffry D. Madura. Temperature and size dependence for Monte Carlo simulations of TIP4p water. *Molecular Physics*, 56:1381–1392, 1985.

[72] William L Jorgensen and Julian Tirado-Rives. Potential energy functions for atomic-level simulations of water and organic and biomolecular systems. *Proceedings of the National Academy of Sciences of the United States of America*, 102:6665–70, 2005.

[73] In Suk Joung and Thomas E. Cheatham. Determination of Alkali and Halide Monovalent Ion Parameters for Use in Explicitly Solvated Biomolecular Simulations. *The Journal of Physical Chemistry B*, 112:9020–9041, 2008.

[74] George Karniadakis, Ali Beskok, and N. R. Aluru. *Microflows and Nanoflows: Fundamentals and Simulation*. Springer New York, 2005.

[75] John G. Kirkwood and Frank P. Buff. The Statistical Mechanical Theory of Surface Tension. *The Journal of Chemical Physics*, 17:338–343, 1949.

[76] Roland Kjellander, Torbjrn kesson, Bo Jnsson, and Stjepan Marelja. Double layer interactions in mono and divalent electrolytes: A comparison of the anisotropic HNC theory and Monte Carlo simulations. *The Journal of Chemical Physics*, 97:1424–1431, 1992.

[77] Jacob Klein and Eugenia Kumacheva. Confinement-Induced Phase Transitions in Simple Liquids. *Science*, 269:816–819, 1995.

[78] Axel Kohlmeyer, Christoph Hartnig, and Eckhard Spohr. Orientational correlations near interfaces. Computer simulations of water and electrolyte solutions in confined environments. *Journal of Molecular Liquids*, 78:233–253, 1998.

[79] P. Kkicheff, S. Marcelja, T. J. Senden, and V. E. Shubin. Charge reversal seen in electrical double layer interaction of surfaces immersed in 2:1 calcium electrolyte. *The Journal of Chemical Physics*, 99:6098–6113, 1993.

[80] A Laaksonen and PG Kusalik. Three-dimensional structure in water-methanol mixtures. *The Journal of Physical Chemistry A*, 101:5910–5918, 1997.

[81] S. Lamperski and A. Zydor. Monte Carlo study of the electrode|solvent primitive model electrolyte interface. *Electrochimica Acta*, 52:2429–2436, 2007.

[82] Jonathan W. Lee, Ali Mani, and Jeremy A. Templeton. Atomistic and Molecular Effects in Electric Double Layers at High Surface Charges. *Langmuir*, 31:7496–7502, 2015.

[83] Jonathan W. Lee, Robert H. Nilson, Jeremy A. Templeton, Stewart K. Griffiths, Andy Kung, and Bryan M. Wong. Comparison of Molecular Dynamics with Classical Density Functional and Poisson-Boltzmann Theories of the Electric Double Layer in Nanochannels. *Journal of Chemical Theory and Computation*, 8:2012–2022, 2012.

[84] D. Levesque, J. J. Weis, and G. N. Patey. Charged hard spheres in dipolar hard sphere solvents. A model for electrolyte solutions. *The Journal of Chemical Physics*, 72:1887–1899, 1980.

[85] Yun Long, Jeremy C. Palmer, Benoit Coasne, Magorzata liwinska Bartkowiak, and Keith E. Gubbins. Pressure enhancement in carbon nanopores: a major confinement effect. *Physical Chemistry Chemical Physics*, 13:17163–17170, 2011.

[86] Yun Long, Jeremy C. Palmer, Benoit Coasne, Magorzata liwinska Bartkowiak, George Jackson, Erich A. Mller, and Keith E. Gubbins. On the molecular origin of high-pressure effects in nanoconfinement: The role of surface chemistry and roughness. *The Journal of Chemical Physics*, 139:144701, 2013.

[87] A. A. Louis. Beware of density dependent pair potentials. *Journal of Physics: Condensed Matter*, 14:9187–9206, 2002.

[88] Jibao Lu, Yuqing Qiu, Riccardo Baron, and Valeria Molinero. Coarse-Graining of TIP4p/2005, TIP4p-Ew, SPC/E, and TIP3p to Monatomic Anisotropic Water Models Using Relative Entropy Minimization. *Journal of Chemical Theory and Computation*, 10:4104–4120, 2014.

[89] Alexander Lyubartsev, Alexander Mirzoev, LiJun Chen, and Aatto Laaksonen. Systematic coarse-graining of molecular models by the newton inversion method. *Faraday Discussions*, 144:43–56, 2010.

[90] Alexander P. Lyubartsev and Aatto Laaksonen. Calculation of effective interaction potentials from radial distribution functions: A reverse Monte Carlo approach. *Physical Review E*, 52:3730–3737, 1995.

[91] Michael W. Mahoney and William L. Jorgensen. A five-site model for liquid water and the reproduction of the density anomaly by rigid, nonpolarizable potential functions. *The Journal of Chemical Physics*, 112:8910–8922, 2000.

[92] Ateeque Malani, K. G. Ayappa, and Sohail Murad. Influence of hydrophilic surface specificity on the structural properties of confined water. *Journal of Physical Chemistry B*, 113:13825–13839, 2009.

[93] Siewert J Marrink, H Jelger Risselada, Serge Yefimov, D Peter Tieleman, and Alex H de Vries. The martini force field: coarse grained model for biomolecular simulations. *The Journal of Physical Chemistry B*, 111:7812–7824, 2007.

[94] J. Marti, G. Nagy, M. C. Gordillo, and E. Gurdia. Molecular simulation of liquid water confined inside graphite channels: Thermodynamics and structural properties. *The Journal of Chemical Physics*, 124:094703, 2006.

[95] J. Martí, J. Sala, and E. Guàrdia. Molecular dynamics simulations of water confined in graphene nanochannels: From ambient to supercritical environments. *Journal of Molecular Liquids*, 153:72–78, 2010.

[96] S. Y. Mashayak and N. R. Aluru. Coarse-Grained Potential Model for Structural Prediction of Confined Water. *Journal of Chemical Theory and Computation*, 8:1828–1840, 2012.

[97] S. Y. Mashayak and N. R. Aluru. Thermodynamic state-dependent structure-based coarse-graining of confined water. *The Journal of Chemical Physics*, 137:214707, 2012.

[98] S. Y. Mashayak, Mara N. Jochum, Konstantin Koschke, N. R. Aluru, Victor Rhle, and Christoph Junghans. Relative Entropy and Optimization-Driven Coarse-Graining Methods in VOTCA. *PLoS ONE*, 10:e0131754, 2015.

[99] S. Y. Mashayak, M. H. Motevaselian, and N. R. Aluru. An EQT-cDFT approach to determine thermodynamic properties of confined fluids. *The Journal of Chemical Physics*, 142:244116, 2015.

[100] Enrique de Miguel and George Jackson. The nature of the calculation of the pressure in molecular simulations of continuous models from volume perturbations. *The Journal of Chemical Physics*, 125:164109, 2006.

[101] Valeria Molinero and Emily B. Moore. Water Modeled As an Intermediate Element between Carbon and Silicon. *The Journal of Physical Chemistry B*, 113:4008–4016, 2009.

[102] M. H. Motevaselian, S. Y. Mashayak, and N. R. Aluru. An EQT-based cDFT approach for a confined Lennard-Jones fluid mixture. *The Journal of Chemical Physics*, 143:124106, 2015.

[103] Florian Müller-Plathe. Coarse-graining in polymer simulation: from the atomistic to the mesoscopic scale and back. *ChemPhysChem*, 3:755–769, 2002.

[104] J. W. Mullinax and W. G. Noid. Extended ensemble approach for deriving transferable coarse-grained potentials. *The Journal of Chemical Physics*, 131:104110, 2009.

[105] Anu Nagarajan, Christoph Junghans, and Silvina Matysiak. Multiscale simulation of liquid water using a four-to-one mapping for coarse-graining. *Journal of Chemical Theory and Computation*, 9:5168, 2013.

[106] Ivo Nezbeda and Jan Slovak. A family of primitive models of water: three-, four and five-site models. *Molecular Physics*, 90:353–372, 1997.

[107] W. G. Noid. Perspective: Coarse-grained models for biomolecular systems. *The Journal of Chemical Physics*, 139:090901, 2013.

[108] Shuichi Nosé. A unified formulation of the constant temperature molecular dynamics methods. *The Journal of Chemical Physics*, 81:511–519, 1984.

[109] Anna Oleksy and Jean-Pierre Hansen. Microscopic density functional theory of wetting and drying of a solid substrate by an explicit solvent model of ionic solutions. *Molecular Physics*, 107:2609–2624, 2009.

[110] Christine Peter and Kurt Kremer. Multiscale simulation of soft matter systems from the atomistic to the coarse-grained level and back. *Soft Matter*, 5:4357–4366, 2009.

[111] Matej Praprotnik, Luigi Delle Site, and Kurt Kremer. Multiscale Simulation of Soft Matter: From Scale Bridging to Adaptive Resolution. *Annual Review of Physical Chemistry*, 59:545–571, 2008.

[112] Peter L. Privalov and Colyn Crane-Robinson. Role of water in the formation of macromolecular structures. *European Biophysics Journal*, 46:203–224, 2017.

[113] Sander Pronk, Szilárd Páll, Roland Schulz, Per Larsson, Pär Bjelkmar, Rossen Apostolov, Michael R. Shirts, Jeremy C. Smith, Peter M. Kasson, David van der Spoel, Berk Hess, and Erik Lindahl. GROMACS 4.5: a high-throughput and highly parallel open source molecular simulation toolkit. *Bioinformatics*, 29:845–854, 2013.

[114] R. Qiao and N. R. Aluru. Ion concentrations and velocity profiles in nanochannel electroosmotic flows. *The Journal of Chemical Physics*, 118:4692–4701, 2003.

[115] R. Qiao and N. R. Aluru. Charge Inversion and Flow Reversal in a Nanochannel Electro-osmotic Flow. *Physical Review Letters*, 92, 2004.

[116] R. Qiao and N.R. Aluru. Atomistic simulation of KCl transport in charged silicon nanochannels: Interfacial effects. *Colloids and Surfaces A: Physicochemical and Engineering Aspects*, 267:103–109, 2005.

[117] A. V. Raghunathan, J. H. Park, and N. R. Aluru. Interatomic potential-based semiclassical theory for Lennard-Jones fluids. *The Journal of Chemical Physics*, 127, 2007.

[118] Jayendran C. Rasaiah, Shekhar Garde, and Gerhard Hummer. Water in nonpolar confinement: from nanotubes to proteins and beyond. *Annual Review of Physical Chemistry*, 59:713–740, 2008.

[119] Dirk Reith, Mathias Pütz, and Florian Müller-Plathe. Deriving effective mesoscale potentials from atomistic simulations. *Journal of Computational Chemistry*, 24:1624–1636, 2003.

[120] Y. Rosenfeld, M. Schmidt, H. Löwen, and P. Tarazona. Fundamental-measure free-energy density functional for hard spheres: Dimensional crossover and freezing. *Physical Review E*, 55:4245–4263, 1997.

[121] Yaakov Rosenfeld. Free-energy model for the inhomogeneous hard-sphere fluid mixture and density-functional theory of freezing. *Physical Review Letters*, 63:980–983, 1989.

[122] Yaakov Rosenfeld. Free energy model for inhomogeneous fluid mixtures: Yukawacharged hard spheres, general interactions, and plasmas. *The Journal of Chemical Physics*, 98:8126–8148, 1993.

[123] R. Roth, R. Evans, A. Lang, and G. Kahl. Fundamental measure theory for hard-sphere mixtures revisited: the White Bear version. *Journal of Physics: Condensed Matter*, 14:12063, 2002.

[124] Roland Roth. Fundamental measure theory for hard-sphere mixtures: a review. *Journal of Physics: Condensed Matter*, 22:063102, 2010.

[125] Joseph F. Rudzinski and W. G. Noid. Coarse-graining entropy, forces, and structures. *The Journal of Chemical Physics*, 135:214101, 2011.

[126] Victor Rühle, Christoph Junghans, Alexander Lukyanov, Kurt Kremer, and Denis Andrienko. Versatile Object-Oriented Toolkit for Coarse-Graining Applications. *Journal of Chemical Theory and Computation*, 5:3211–3223, 2009.

[127] A.J. Rzepiela, Martti Louhivuori, C. Peter, and S.J. Marrink. Hybrid simulations: combining atomistic and coarse-grained force fields using virtual sites. *Physical Chemistry Chemical Physics*, 13:10437–10448, 2011.

[128] K. Michael Salerno, Amalie L. Frischknecht, and Mark J. Stevens. Charged Nanoparticle Attraction in Multivalent Salt Solution: A Classical-Fluids Density Functional Theory and Molecular Dynamics Study. *The Journal of Physical Chemistry B*, 120:5927–5937, 2016.

[129] T. Sanghi and N. R. Aluru. Coarse-grained potential models for structural prediction of carbon dioxide (CO2) in confined environments. *The Journal of Chemical Physics*, 136:024102–024102–13, 2012.

[130] E Schmidt. *Properties of Water and Steam in SI Units*. Springer-Verlag: Düsseldorf, 1969.

[131] P. Schofield and J. R. Henderson. Statistical Mechanics of Inhomogeneous Fluids. *Proceedings of the Royal Society of London. Series A, Mathematical and Physical Sciences*, 379:231–246, 1982.

[132] Mark A. Shannon, Paul W. Bohn, Menachem Elimelech, John G. Georgiadis, Benito J. Marias, and Anne M. Mayes. Science and technology for water purification in the coming decades. *Nature*, 452:301–310, 2008.

[133] M. Scott Shell. The relative entropy is fundamental to multiscale and inverse thermodynamic problems. *The Journal of Chemical Physics*, 129:144108, 2008.

[134] Patrice Simon and Yury Gogotsi. Materials for electrochemical capacitors. *Nature Materials*, 7:845–854, 2008.

[135] W.R. Smith and D. Henderson. Analytical representation of the Percus-Yevick hard-sphere radial distribution function. *Molecular Physics*, 19:411–415, 1970.

[136] Alberto Striolo. From Interfacial Water to Macroscopic Observables: A Review. *Adsorption Science & Technology*, 29:211–258, 2011.

[137] M. E. Suk, A. V. Raghunathan, and N. R. Aluru. Fast reverse osmosis using boron nitride and carbon nanotubes. *Applied Physics Letters*, 92:133120, 2008.

[138] Emad Tajkhorshid, Peter Nollert, Morten Jensen, Larry J. W. Miercke, Joseph O'Connell, Robert M. Stroud, and Klaus Schulten. Control of the selectivity of the aquaporin water channel family by global orientational tuning. *Science (New York, N.Y.)*, 296:525–530, 2002.

[139] Yiping Tang and Jianzhong Wu. A density-functional theory for bulk and inhomogeneous Lennard-Jones fluids from the energy route. *The Journal of Chemical Physics*, 119:7388–7397, 2003.

[140] Zixiang Tang, L. Mier-y Teran, H. T. Davis, L. E. Scriven, and H. S. White. Non-local free-energy density-functional theory applied to the electrical double layer. *Molecular Physics*, 71:369–392, 1990.

[141] Zixiang Tang, L. E. Scriven, and H. T. Davis. Interactions between primitive electrical double layers. *The Journal of Chemical Physics*, 97:9258–9266, 1992.

[142] P. Tarazona. Density Functional for Hard Sphere Crystals: A Fundamental Measure Approach. *Physical Review Letters*, 84:694–697, 2000.

[143] P. Tarazona and Y. Rosenfeld. From zero-dimension cavities to free-energy functionals for hard disks and hard spheres. *Physical Review E*, 55:R4873–R4876, 1997.

[144] Everett Thiele. Equation of State for Hard Spheres. *The Journal of Chemical Physics*, 39:474–479, 1963.

[145] Koki Urita, Yuichi Shiga, Toshihiko Fujimori, Taku Iiyama, Yoshiyuki Hattori, Hirofumi Kanoh, Tomonori Ohba, Hideki Tanaka, Masako Yudasaka, Sumio Iijima, Isamu Moriguchi, Fujio Okino, Morinobu Endo, and Katsumi Kaneko. Confinement in Carbon Nanospace-Induced Production of KI Nanocrystals of High-Pressure Phase. *Journal of the American Chemical Society*, 133:10344–10347, 2011.

[146] Frank van Swol and J. R. Henderson. Wetting and drying transitions at a fluid-wall interface: Density-functional theory versus computer simulation. *Physical Review A*, 40:2567–2578, 1989.

[147] Juan M. Vanegas, Alejandro Torres-Snchez, and Marino Arroyo. Importance of Force Decomposition for Local Stress Calculations in Biomembrane Molecular Simulations. *Journal of Chemical Theory and Computation*, 10:691–702, 2014.

[148] E. Velasco and P. Tarazona. Wetting and drying at a solidfluid interface. *The Journal of Chemical Physics*, 91:7916–7924, 1989.

[149] Gregory A. Voth. *Coarse-Graining of Condensed Phase and Biomolecular Systems*. CRC Press, 2008.

[150] Anders Wallqvist and Raymond D Mountaint. Molecular models of water: Derivation and description. In *Reviews in Computational Chemistry*, volume 13, chapter 4, pages 183–247. John Wiley & Sons, Inc., 2007.

[151] Han Wang, Christoph Junghans, and Kurt Kremer. Comparative atomistic and coarse-grained study of water: What do we l ose by coarse-graining? *The European Physical Journal E*, 28:221–229, 2009.

[152] Patrick B. Warren, Andrey Vlasov, Lucian Anton, and Andrew J. Masters. Screening properties of Gaussian electrolyte models, with application to dissipative particle dynamics. *The Journal of Chemical Physics*, 138:204907, 2013.

[153] Vadim Warshavsky and Marcelo Marucho. Polar-solvation classical density-functional theory for electrolyte aqueous solutions near a wall. *Physical Review E*, 93:042607, 2016.

[154] John D. Weeks, David Chandler, and Hans C. Andersen. Role of Repulsive Forces in Determining the Equilibrium Structure of Simple Liquids. *The Journal of Chemical Physics*, 54:5237–5247, 1971.

[155] M. S. Wertheim. Exact Solution of the Percus-Yevick Integral Equation for Hard Spheres. *Physical Review Letters*, 10:321–323, 1963.

[156] Di Wu and David A. Kofke. Phase-space overlap measures. I. Fail-safe bias detection in free energies calculated by molecular simulation. *The Journal of Chemical Physics*, 123:054103, 2005.

[157] J. Z. Wu. Density Functional Theory for Liquid Structure and Thermodynamics. In Xiaohua Lu and Ying Hu, editors, *Molecular Thermodynamics of Complex Systems*, Structure and Bonding, pages 1–73. Springer Berlin Heidelberg, 2009.

[158] Jianzhong Wu. Density functional theory for chemical engineering: From capillarity to soft materials. *AIChE Journal*, 52:1169–1193, 2006.

[159] Yanbin Wu and N. R. Aluru. Graphitic CarbonWater Nonbonded Interaction Parameters. *The Journal of Physical Chemistry B*, 117:8802–8813, 2013.

[160] Zhenyu Yan, Sergey V. Buldyrev, Nicolas Giovambattista, Pablo G. Debenedetti, and H. Eugene Stanley. Family of tunable spherically symmetric potentials that span the range from hard spheres to waterlike behavior. *Physical Review E*, 73:051204, 2006.

[161] Zhenyu Yan, Sergey V. Buldyrev, Pradeep Kumar, Nicolas Giovambattista, and H. Eugene Stanley. Correspondence between phase diagrams of the TIP5P water model and a spherically symmetric repulsive ramp potential with two characteristic length scales. *Physical Review E*, 77:042201, 2008.

[162] Yang-Xin Yu and Jianzhong Wu. Structures of hard-sphere fluids from a modified fundamental-measure theory. *The Journal of Chemical Physics*, 117:10156–10164, 2002.

[163] Francisco Zaera. Surface chemistry at the liquid/solid interface. *Surface Science*, 605:1141–1145, 2011.

[164] Francisco Zaera. Probing Liquid/Solid Interfaces at the Molecular Level. *Chemical Reviews*, 112:2920–2986, 2012.